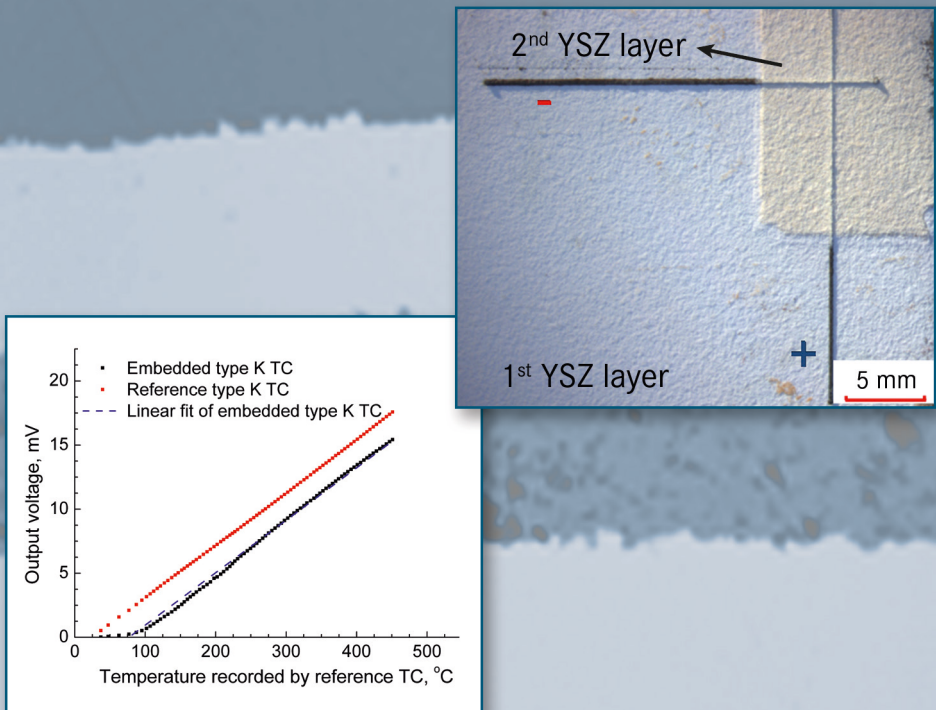


Development of Embedded Thermocouple Sensors for Thermal Barrier Coatings (TBCs) by a Laser Cladding Process

Yanli Zhang



Forschungszentrum Jülich GmbH
Institute of Energy and Climate Research
Materials Synthesis and Processing (IEK-1)

Development of Embedded Thermocouple Sensors for Thermal Barrier Coatings (TBCs) by a Laser Cladding Process

Yanli Zhang

Schriften des Forschungszentrums Jülich
Reihe Energie & Umwelt / Energy & Environment

Band / Volume 312

ISSN 1866-1793

ISBN 978-3-95806-129-3

Bibliographic information published by the Deutsche Nationalbibliothek.
The Deutsche Nationalbibliothek lists this publication in the Deutsche
Nationalbibliografie; detailed bibliographic data are available in the
Internet at <http://dnb.d-nb.de>.

Publisher and
Distributor: Forschungszentrum Jülich GmbH
Zentralbibliothek
52425 Jülich
Tel: +49 2461 61-5368
Fax: +49 2461 61-6103
Email: zb-publikation@fz-juelich.de
www.fz-juelich.de/zb

Cover Design: Grafische Medien, Forschungszentrum Jülich GmbH

Printer: Grafische Medien, Forschungszentrum Jülich GmbH

Copyright: Forschungszentrum Jülich 2016

Schriften des Forschungszentrums Jülich
Reihe Energie & Umwelt / Energy & Environment, Band / Volume 312

D 294 (Diss., Bochum, Univ., 2015)

ISSN 1866-1793
ISBN 978-3-95806-129-3

The complete volume is freely available on the Internet on the Jülicher Open Access Server (JuSER) at
www.fz-juelich.de/zb/openaccess.



This is an Open Access publication distributed under the terms of the [Creative Commons Attribution License 4.0](https://creativecommons.org/licenses/by/4.0/),
which permits unrestricted use, distribution, and reproduction in any medium, provided the original work is properly cited.

Abstract:

Thermal barrier coatings (TBCs) are now being widely used on gas turbine engines to lower the surface temperatures of metallic substrate from extreme hot gas stream in combustor and turbine components. The thermally grown oxide (TGO) growth rate plays an important role in the life time of TBC systems. The accurate real-time monitoring of bond-coat/ 8YSZ interface temperature in thermal barrier coatings (TBCs) in hostile environments opens large benefits to efficient and safe operation of gas turbines. A new method for fabricating high temperature thermocouple sensors which can be placed close to this interface using laser cladding technology has been developed.

K-type thermocouple powders consisting of alumei ($\text{Ni}_2\text{Al}_2\text{Mn}_1\text{Si}$) and chromel (Ni_{10}Cr) were studied as candidate feedstock materials. A thermocouple sensor using these materials was first produced by coaxial continuous wave (CW) or pulsed laser cladding process onto the standard yttria partially stabilized zirconia (7~8 wt.% YSZ) coated substrate and afterwards embedded with a second YSZ layer deposited by the atmospheric plasma spray (APS) process. The process parameters of the laser cladding were optimized with respect to the degradation of the substrate, dimensions, topography, thermosensitivity and embeddability, respectively. Infrared cameras were used to monitor the surface temperature of clads during this process.

The manufacture of the cladded thermocouple sensors provides minimal intrusive features to the substrate. The dimensions were in the range of two hundred microns in thickness and width for CW laser cladding and less than 100 microns for pulsed laser cladding. Additionally, continuous thermocouple sensors with reliable performance were produced. It is possible to embed sensors manufactured by CW laser cladding rather than by pulsed laser cladding due to the limited bonding strength between the clads and the substrate. Periodically droplets were formed along the clads under improper parameters, the mechanism to this is discussed in terms of particle size distribution after interaction with the laser beam, melts duration and Rayleigh's theory.

To sum up, laser cladding is a prospective technology for manufacturing microsensors on the surface of or even embedded into functional coatings that can survive in operation environments for in-situ monitoring. Production of sensors within thermal barrier coatings (TBCs) increases the application field of the laser cladding technique.

Kurzfassung:

Wärmedämmschichten (WDS) werden aktuell verbreitet in Gasturbinen genutzt, um die Oberflächentemperatur des metallischen Substrates in der Brennkammer und den Turbinenkomponenten gegenüber dem extrem heißen Gasstrom zu senken. Die genaue Echtzeitmessung von Oberflächentemperaturen oder der Innentemperatur einer Wärmedämmschicht in aggressiver Umgebung eröffnet beträchtliche Vorteile für den effizienten und sicheren Betrieb von Gasturbinen. Es wurde eine neue Methode zur Herstellung von Hochtemperatur-Thermoelementen für Gasturbinen mittels Laser-Auftragsschweißen entwickelt.

Alumel ($\text{Ni}_2\text{Al}_2\text{Mn}_1\text{Si}$) und Chromel (Ni_{10}Cr) wurden in Pulverform als Ausgangsmaterialien für Thermoelemente des K-Typs untersucht. Um einen Thermoelement-Sensor mit diesen Materialien herzustellen, wurde zunächst auf ein mit herkömmlichem Yttriumoxid-teilstabilisiertem Zirkoniumdioxid (7~8 wt.% YSZ) beschichtetes Substrat der Sensor durch koaxiales, kontinuierliches oder gepulstes Laser-Auftragsschweißen aufgebracht. Anschließend wurde die Einbettung durch atmosphärisches Plasmaspritzen (APS) einer weiteren YSZ-Schicht durchgeführt. Die Prozessparameter des Laser-Auftragsschweißens wurden optimiert in Bezug auf die Degradation des Substrats, die Dimensionen, Topographie, Wärmeempfindlichkeit und Einbettungsmöglichkeit. Es wurden Infrarotkameras eingesetzt, um die Oberflächentemperatur der Aufschweißung während des Prozesses zu verfolgen.

Die Herstellung des aufgeschweißten Hochtemperatursensors beeinflusst minimal die Funktion des Substrates. Die Abmessungen liegen für kontinuierliches Laser-Auftragsschweißen im Bereich von 200 μm und für gepulstes Laser-Auftragsschweißen unter 100 μm . Außerdem wurden kontinuierliche Thermosensoren mit zuverlässigen Ergebnissen hergestellt. Wegen der begrenzten Bindungsstärke zwischen den Aufschweißungen und dem Substrat ist es eher möglich, Sensoren durch koaxiales, kontinuierliches Laser-Auftragsschweißen herzustellen, als mit gepulstem Laser-Auftragsschweißen. Mit ungeeigneten Prozessparametern wurden periodische Tropfen entlang der Aufschweißungen gebildet. Der Mechanismus hierfür wird unter den Gesichtspunkten der Partikelgrößenverteilung nach dem Einwirken des Laserstrahls, der Schmelzdauer und der Rayleighs Theorie diskutiert.

Laser-Auftragsschweißen ist eine aussichtsreiche Technologie zur Herstellung von Mikrosensoren, die an der Oberfläche oder sogar eingebettet in funktionellen Beschichtungen unter Arbeitsbedingungen direkte Messungen ermöglichen. Die Produktion von Sensoren in Wärmedämmschichten erweitert den Anwendungsbereich für das Laser-Auftragsschweißen.

Table of Contents

Abbreviations	I
1. Introduction and Objectives	1
2. Background and Basic Overview	3
2.1 Introduction of Thermal Barrier Coatings (TBCs).....	3
2.2 Spray Techniques of TBCs	5
2.2.1 Electron Beam Physical Vapor Deposition (EB-PVD).....	5
2.2.2 Atmospheric Plasma Spray (APS).....	6
2.3 Introduction of ‘Smart’ Coatings	7
2.4 State of the Art Deposition Methods for Sensors.....	7
2.4.1 Mask-based Twin Wire Arc Deposition.....	7
2.4.2 Mask-based Sputtering	8
2.4.3 Direct-Write Thermal Spray (DWTS).....	8
2.5 Introduction of Laser Cladding Technology	9
2.5.1 Laser Beam Characteristics	9
2.5.2 Different Methods of Laser Cladding.....	11
2.5.3 Clad Dimensional Characteristics	14
2.5.4 Important Parameters in Laser Cladding	14
2.5.5 Non-invasive Thermal Imaging Techniques	18
2.5.6 Traditional Applications	20
2.5.7 New Applications	20
3. Experimental Methods	23
3.1 Concept of Embedded Thermocouple (TC) Sensors.....	23
3.2 Substrate Materials	24
3.3 Feedstock Selection.....	24
3.4 Thermal Spray Processes	25
3.4.1 Vacuum Plasma Spraying (VPS).....	25
3.4.2 Atmospheric Plasma Spray (APS).....	26
3.5 Laser Cladding Technology	27
3.6 Characterization Techniques	29
3.6.1 Particle Size Distribution.....	29

3.6.2 Micro-spot Monitor (MSM)	29
3.6.3 Infrared (IR) Camera	29
3.6.4 Cyberscan Topographer	30
3.6.5 Light Microscopy and Confocal Laser Microscopy	30
3.6.6 Ohmmeter and Four Probe Tester	30
3.6.7 Measurement of the Seebeck Coefficient	31
3.6.8 Shear Force Measurements	32
4. Experimental Results and Discussion	35
4.1 Feedstock Characterization	35
4.2 Laser Beam Characterization	36
4.2.1 Spatial Distribution of the Laser Beam	36
4.2.2 Spot Size Determination	37
4.3 Powder Feeding Rate	37
4.4 Deposition of K-type TCs with a continuous wave (CW) Laser	38
4.4.1 Deposition of Alumel Tracks	38
4.4.2 Deposition of Chromel Tracks	47
4.4.3 Preparation of K-type TC with Relatively Optimized Parameters	48
4.4.4 Thermosensitivity Characterization of the Cladded TC	53
4.4.5 Characterization of the Cladded TC Sensor	55
4.4.6 Embedding of Cladded Type-K TC	56
4.4.7 Deposition of TCs in Small Dimensions	61
4.5 Deposition of K-type TC with a Pulsed Laser	67
4.5.1 Optimization of Alumel Tracks	67
4.5.2 Optimization of Chromel Tracks	74
4.5.3 Preparation of K-type TCs	77
4.5.4 Embedding of the Cladded TCs	78
4.6 Shear Force Measurements	80
4.7 Summary of Optimized Tracks	81
5. Droplets Formation Mechanism	83
6. Summary and Outlook	91
7. Literature	93

Abbreviations

CW	Continuous wave
YSZ	Yttria partially stabilized zirconia
APS	Atmospheric plasma spraying/ sprayed
TBCs	Thermal barrier coatings
CSZ	Calcia stabilized zirconia
MSZ	Magnesia stabilized zirconia
EB-PVD	Electron beam physical vapor deposition/ deposited
DC	Direct current
DWTS	Direct-write thermal spray
W_H	Width of the heat affected zone
W_C	Track width
H_C	Clad height
H_D	Depth of the dilution
H_H	Depth of the heat affected zone
P	Laser power
D_b	Spot size
V	Scanning velocity
V_p	Shielding gas rate
V_c	Carrier gas rate
E	Energy input per unit length
G	Mass of injected powder per unit length
E_0	Laser pulse energy
t	Laser pulse width
f	Laser pulse frequency
P_0	Average power
C	Duty cycle
TC	Thermocouple
VPS	Vacuum plasma spraying
MSM	Micro-spot Monitor

IR	Infrared camera
R	Resistance
A	Cross-sectional area
L	Length of a track
ρ	Resistivity
S	Stand-off distance
t	Cladding time
c_p	Specific heat capacity
T_m	Melting point
RT	Room temperature
H_{fusion}	Latent heat of fusion
2D	Two dimensional
HAZ	Heat affected zone
EMF	Electromotive force
LC	Laser cladding
TBC	Top barrier coating
BC	Bond coat
CTE	Coefficient of thermal expansion
σ	Surface tension
τ	Break up time
λ	Wavelength of the disturbance
R_c	Radius of an cylinder
ρ_c	Density

1. Introduction and Objectives

Thermal barrier coatings (TBCs) are now being widely used in gas turbine engines to lower the surface temperatures of metallic substrate in an extreme hot gas stream in combustor and turbine components. On one hand, life capabilities of engines could be extended. On the other hand, an increase of the turbine inlet temperatures could also be allowed, thereby, the operation efficiency and performance of turbine engines could be improved [1-8].

Higher efficiency demands lead to increased combustion temperatures in gas turbine engines. Applying higher engine operating temperature requires accurate knowledge of the turbine blade temperature to avoid damage of engine components. Effective monitoring and diagnosis in such harsh operating conditions is of critical importance. If critical operating conditions could be continuously monitored in real-time, problems can be detected and solved during operation. ‘Smart’ coatings are generally proposed for the purpose of in-situ monitoring during operation of turbine blades in order to better control surrounding environment and design coatings with appropriate structures. ‘Smart’ coatings are the coatings integrated with embedded sensors, such as thermocouple sensors or strain gauge sensors and so on. This kind of coatings combines the function of a thermal barrier coating and a sensor, with which feedback about the functional status and operating history of the coatings as well as of the coated structure and surrounding environment could be provided.

In this study, a new method for fabricating high temperature type K thermocouple sensors using laser cladding technology has been developed. The desired TC sensors deposited by this process should contain certain properties: minimal effect on the substrate; small dimensions (minimal intrusion to the substrate); electrical conductivity as well as embedded feature for monitoring the internal temperature within a certain depth of the coatings.

There are a couple of challenges when applying this technique: first of all, a melting pool on the substrate surface needs to be formed for the traditional laser cladding, but sensors with little impact to the substrate are required to keep the original performance of TBCs; secondly, tracks tend to detach due to the low adhesion strength; thirdly, sensors in small dimensions or high roughness (discontinuous) tend to lose their electrical conductivity; furthermore, cladded sensors

have the risk to lose the electrical conductivity during embedding within a second YSZ layer because of continuous impingement of ceramic particles to the tracks; mismatched Seebeck coefficient of cladde type K TC sensors to that of commercial ones would mislead the temperature recording during operation, therefore, reliable temperature cannot be captured.

The aim of this work is to fabricate K-type TC sensors with properties of minimal impact to the substrate, small dimension as well as roughness and good electrical conductivity by laser cladding technology, moreover, to embed them by a second ceramic layer. The success of this work could increase application field of the laser cladding technique.

2. Background and Basic Overview

2.1 Introduction of Thermal Barrier Coatings (TBCs)

Superalloys used in commercial gas turbine engines normally melt in the range of 1230 °C~1315 °C and the operation temperature in a combustion gas environment typically above 1370 °C. In order to avoid failure caused by melting, thermal fatigue or creep, airfoils along with effective cooling geometries and hollow structures were designed and the engine efficiency was improved considerably. Higher efficiency demands led to innovative technologies that could further reduce the surface temperatures of superalloys. One method of protecting gas turbine engine components is through the application of thermal barrier coatings [1].

Thermal barrier coatings (TBCs) are now being widely used in gas turbine engines to lower the surface temperatures of metallic substrate from extreme hot gas stream in combustor and turbine components [2-5]. The application of TBCs (100 ~ 500 µm in thickness) along with internal cooling systems enables a large temperature drop (several 100 K) across the ceramic layer, hence, modern gas turbine engines could be operated well above the melting point of metallic materials (~1300 °C) [3, 6, 7]. Extended life capabilities of engines could be achieved by lowering the substrate temperatures. On the other hand, an increase of the turbine inlet temperatures could also be allowed, thereby, the operation efficiency and performance of turbine engines could be improved [3-5, 7-9]. TBCs are also being used in certain diesel engines, where higher operation temperatures translate into increased fuel economy and cleaner exhaust [2].

The TBC components must withstand very harsh environment accompanied by high temperature, large temperature gradient, complex stress condition and corrosion atmosphere. No single material is satisfied for these multifunctional requirements. As a result, TBC system with duplex-type consists of a metallic bond coat (75~150 µm thick) and an insulating ceramic topcoat (300~600 µm thick) was established. The bond coat protects the underneath substrate from high temperature oxidation and corrosion as well as improves the adhesion strength between the substrate and the topcoat. The ceramic topcoat that normally has a low thermal conductivity could prevent the heat flux into the metallic substrate [2, 3, 5, 7, 9].

The earliest ceramic coatings were frit enamels which were applied to aircraft engine components in the 1950s. In the 1960s, flame sprayed ceramic coatings with NiAl bond coats were developed in commercial aero engines. Among the various early ceramic materials evaluated for thermal barrier applications, alumina and zirconia were identified as promising candidate materials. The effectiveness of alumina coatings was limited by the relatively high thermal conductivity and destabilization upon temperatures above 1100 °C. Pure zirconia is also not suitable for the application as it undergoes a different phase transition from martensitic monoclinic to tetragonal at about 1000 °C accompanied by a large volume change (3 to 9 %). Therefore, different doping additions, such as MgO or CaO, were used with the intent of stabilizing the cubic phases [10]. V. S. Stubican [11] reported that the cubic phases were not stable below about 1140 °C for calcia stabilized zirconia (CSZ) and 1400 °C for magnesia stabilized zirconia (MSZ). Succeeding decades showed continuous improvements in the TBC materials and coating technology. It was however in the 1980s when the TBCs were significantly improved. During this decade, yttria stabilized zirconia (YSZ) was identified as an exceptional ceramic topcoat material due to its high melting point, low thermal conductivity, relatively high coefficient of thermal expansion when compared to other oxides and high thermal shock resistance [12, 13]. This modification has resulted in a fourfold improvement in durability [14]. The initial zirconia-yttria TBCs contained 12-20 % Y_2O_3 to fully stabilize the cubic phase [10] and Stecura proved that lowering the yttria level to 6-8 wt.%, TBC exhibited better performance at the end of the 1970s [12] and has been frequently used in aero and stationary gas turbines since the beginning of the 1980s [14-15]. Another reason for the frequent use of (6-8 wt.%) YSZ is the contributed to relatively good fracture toughness of this material [16]. A higher amount of stabilizer would lead to a fully stabilized cubic zirconia with a relatively low toughness. A lower amount of stabilizing additive leads to a higher toughness at room temperature, but detrimental phase transformations during heating could not be completely prevented [9]. Up to now, a candidate ceramic layer that is better than YSZ in all terms of relevant properties has not been discovered yet.

2.2 Spray Techniques of TBCs

In terms of preparation techniques, although there are various methods for depositing ceramic layers on metal substrates, electron beam physical vapor deposition (EB-PVD) and atmospheric plasma spraying (APS) are the most frequently used technologies for the deposition [2, 3, 5, 7, 9].

2.2.1 Electron Beam Physical Vapor Deposition (EB-PVD)

In the EB-PVD process, vapors are produced by heating the porous ingot of a ceramic material with a high energy electron beam in a vacuum chamber, and the evaporated atoms condense on the typically preheated substrates. Crystal nuclei form on favored sites, growing laterally and in thickness to form individual columns. A rather globular microstructure is initially formed which will then transition into a columnar structure due to the selection of a favorable growth direction during further deposition [17]. The microstructure of an EB-PVD deposited TBC is shown in **Figure 2.1**. The clearly visible columnar morphology can accommodate stress build-up under tensile loading and the spacing between the columns allows a free expansion [18]. The EB-PVD produced coatings offer the advantage of superior strain, erosion, and thermal shock tolerant behavior as well as retain an aerodynamically favorable smooth surface and usually exhibit long lifetime. Nevertheless, these advantages are gained at the expense of rather high-thermal conductivity and production cost [5, 19-22, 23].

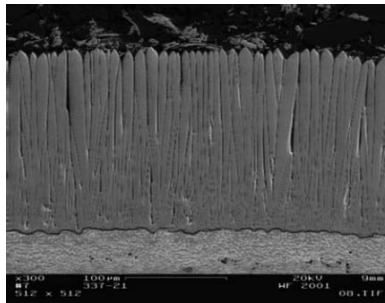


Figure 2.1 The microstructure of a 7YSZ thermal barrier coating deposited by EB-PVD on NiPtAl bond coat [17].

2.2.2 Atmospheric Plasma Spray (APS)

APS technique has been widely employed for TBC applications. The plasma gun typically consists of a tungsten cathode and anode surrounded by a cooling jacket and passages for the carrier gas. The plasma is generated by striking an arc between the cathode and anode with a high direct current (DC) in the presence of the electrically excitable primary gas in confined space. Argon or nitrogen is commonly applied as the primary gas. A high enthalpy secondary gas, typically H_2 or He, is injected into the established plasma plume to enhance the plasma performance. The torch components are water cooled to prevent the cathode and anode from degradation and melting by the high temperature plasma.

During spraying, the spray feedstock, typically in the form of powders but sometimes liquid, suspension or wire, is injected into high temperature plasma and accelerated to high velocities, impinging upon the substrate, and rapidly solidified to form a “splat” (a flattened particle). The coating develops by successive impingement and interlock among the splats, resulting in laminar microstructures and microcracks parallel to the metal/ceramic interface which provide low thermal conductivity with suitable porosity and superior adhesion. **Figure 2.2** presents the cross-section micrograph of typical APS TBCs.

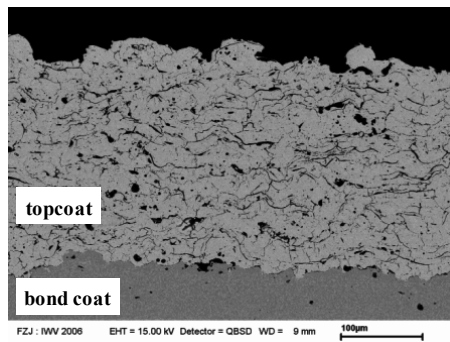


Figure 2.2 The microstructure of an APS produced 7YSZ thermal barrier coating with a NiCoCrAlY bond coat.

APS TBCs are attractive for commercial application due to its versatility and low production costs. However, APS TBCs generally have shorter thermal-cycling lives than EB-PVD TBCs, because the proliferation of microstructural defects parallel to the interface and the roughness of the interface. Hence, APS TBCs are typically not applied on the most demanding locations in aircraft engines but on combustors, fuel vaporizers, after burner flame holders, and stator vanes. APS TBCs have served extremely well in industrial gas turbine engines, including blade and vane applications, because of lower operation temperatures, reduced temperature gradients, and fewer thermal cycles [2].

2.3 Introduction of ‘Smart’ Coatings

Higher efficiency demands lead to increased combustion temperatures in gas turbine engines. However, achieving higher engine operating temperature requires accurate knowledge of the turbine blade temperature. Effective monitoring and diagnosis in such harsh operating conditions is of critical importance. If critical operating conditions could be continuously monitored in real-time, problems can be detected and solved during the operation. ‘Smart’ Coatings are generally proposed for the purpose of in-situ monitoring during operation of turbine blades in order to better control surrounding environment and design coatings with appropriate structures.

‘Smart’ coatings are coatings with integrated embedded sensors, such as thermocouple sensors or strain gauge sensors and so on. This kind of coatings possesses multiple functions as thermal barrier and sensors, with which feedback about the functional status and operating history of the coatings as well as of the coated structure and surrounding environment could be provided.

2.4 State of the Art Deposition Methods for Sensors

2.4.1 Mask-based Twin Wire Arc Deposition

The embedded sensors within the coatings by thermal spray technology were first addressed by Fasching et al. [24]. A mask-based twin wire arc deposition process was used to fabricate

thermocouples. In arc spraying, two conductive materials are injected into a direct current arc and melted; an atomizing gas breaks up the molten materials into droplets at the wire tips and propels it towards the prepared workpiece surface to form the coatings [25].

For preparing a thermocouple sensor within the coatings, a mask with constructed pattern was placed on an insulating substrate and the first thermoleg was sprayed on it, leaving a thin wire trace connected to a small pad. The second thermoleg was similarly sprayed by using another mask and the junction was formed with connected pads. Additional insulation layers could be sprayed onto the sensor to fully embed it. Feature sizes achievable with this approach are in the order of 200 μm . The yielded Seebeck coefficients of sprayed thermocouples were reasonably approaching bulk values when testing up to 200 $^{\circ}\text{C}$.

2.4.2 Mask-based Sputtering

Magnetron sputtering is a plasma vapor deposition process in which plasma is created and positively charged ions from the plasma are accelerated by an electrical field superimposed on the negatively charged electrode or "target". The positive ions strike the negative electrode with sufficient force to dislodge and eject atoms from the target [26]. The fabrication of the thin film sensors was performed in a class 1000 cleanroom to minimize possible contamination. The thermocouple Pt/ Pt13Rh thin film sensors were patterned with stenciled shadow masks during sputter deposition. The PdCr gauge was prepared first by sputtering and then patterned with the photolithography technique and chemical etching. These thin film sensors provided minimally intrusive features. However, the disadvantages of this technology are quite time-consuming because of either the application of masks or strict deposition conditions [27].

2.4.3 Direct-Write Thermal Spray (DWTS)

Over the past decade, thermal spray has been demonstrated the capability to fabricate a variety of sensors that are particularly well suited under harsh environments. Up to now, thermocouple and thermistor sensors, heaters, strain sensors, heat flux, and high density thermopile devices for

electricity production have been successfully fabricated [26, 28-35]. The typical dimension for sensors formed using commercial thermal spray process is several centimeters and far from applications. One approach to reduce the linewidth is to use a mask, which is placed over the substrate to block a portion of the plume. Linewidths less than 1 mm can be achieved. However, this approach restricts to non-conformal geometries. Apart from this, changes in the feature geometry require a new mask which also limits its application. Another approach is to place an aperture-collimator combined with a robotic motion control close to the torch to block the outer portion of the spray plume in flight, resulting in a smaller linewidth. Linewidths in the order of 100 μm could be produced with this system [36-37]. This provides a variety of vital advantages: reliability, robustness and survivability in extremely harsh thermal and chemical environments, cost effective implementation, and fabrication onto surfaces that are large, conformal and flexible [34].

Fabrication of finer linewidths is challenged by using thermal spray alone and cannot be reliably prepared using this additive process alone. Laser micromachining of thermal spray coatings for sensor applications was demonstrated [30] and feature sizes approaching to 15-20 μm could be readily achieved [37].

2.5 Introduction of Laser Cladding Technology

Laser cladding is a well-established industrial technology, which utilizes a focused or defocused laser beam as heating source to melt a thin layer of substrate and additive materials to create a pore-free and crack-free coating.

2.5.1 Laser Beam Characteristics

Laser beam characteristics play an important role in laser cladding process. The quality of a laser beam is indicated by many parameters. Some of them are beam parameter product (BPP), laser beam mode, energy distribution over the beam spot area, polarization and focusability.

The BPP provides an indication of the focused beam size and the focal depth which is represented by

$$BPP = \frac{r\theta}{2}$$

where r is the beam spot radius in the waist of the laser beam and θ is the far-field full divergence angle, as shown in **Figure 2.3**. From the above equation, it can be concluded that a low divergence angle produces a greater depth of focus and smaller focused spot.

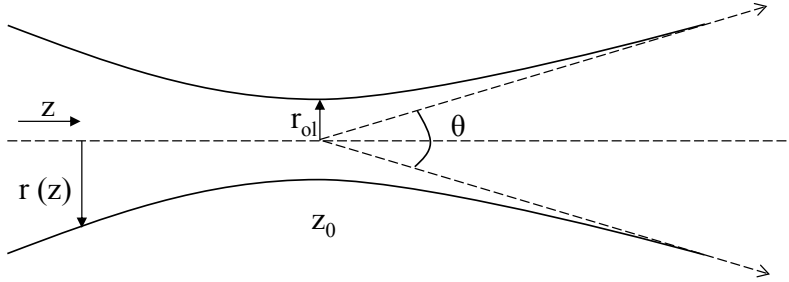


Figure 2.3 Laser beam geometry.

It is necessary to resonate the beam in a resonator so as to achieve a good beam quality. Due to the repeated reflections between mirrors, the distribution of the amplitude and phases of the electromagnetic field can be produced in the resonator [38]. These specific field shapes produced in the resonator are known as transverse electromagnetic modes (TEM) of a passive resonator. TEM_{pl} demonstrates transverse electromagnetic modes in polar coordinates. The subscript p indicates the number of nodes of zero intensity transverse to the beam axis in radial direction and the subscript l indicates the number of nodes of zero intensity transverse to the beam axis in tangential direction. The intensity distribution $I_{pl}(\gamma, \varphi)$ of a TEM_{pl} mode can be represented by

$$I_{pl}(\gamma, \varphi) = I_0 \left(\frac{2r^2 M^2}{r_l^2} \right)^l \left[L_l^p \left(\frac{2r^2 M^2}{r_l^2} \right) \right]^2 [\cos(l\varphi)]^2 \exp \left(-\frac{2r^2 M^2}{r_l^2} \right)$$

where I_0 is the intensity scale factor (W/m^2), r_l is the radius of the laser beam profile, M^2 is the beam quality factor and L_l^p is the generalized Laguerre polynomial of order p and index l [39].

The propagation can be illustrated by the quality factor M^2 , which is related as

$$M^2 = \frac{n\pi r_{ol} \theta}{2\lambda}$$

where λ is the laser wavelength in the used medium (m), n is the index of reflection. The propagation factor k is defined as

$$k = \frac{1}{M^2} - \frac{2\lambda}{n\pi r_{ol} \theta}$$

If $k=M^2=1$, the laser beam is Gaussian.

2.5.2 Different Methods of Laser Cladding

Basically, there are two different kinds of techniques for laser cladding: two-step process and single-step process. In the two-step process, the coating material in the form of powder is preplaced on the substrate and melted with a laser beam to form a coating. In the single-step cladding, an additive material is fed into the melting pool created by the laser beam as a powder, wire, paste, or melts to form the coating [40-42].

2.5.2.1 Laser Cladding with Pre-placed Powder

Prior to the laser treatment, the powder particles are pre-placed with a certain thickness on the surface of the substrate. Since pre-placed particles do not have enough bonding to the substrate, it is necessary to prevent the particles from blowing away due to the gas flow during melting in the second step. A chemical binder is usually mixed with particles to ensure its adhesion with the substrate during laser treatment. In the second step of the process, a melting pool is created on the top surface of pre-placed powders due to the laser radiation. A melt advances from the surface towards to the interface due to the heat conduction. If the energy is sufficient, the heat will penetrate into the substrate and a fusion bond will be created between the substrate and the

coating. Good adhesion and low dilution are obtained when supplying just enough energy. Excessive energy leads to excessive dilution while insufficient energy causes incomplete melting of particles or poor bonding strength [41, 43]. Results show that this technique works well for single track production but is not suitable for multiple ones [44].

Some drawbacks of this process: it is time consuming due to additional slurry preparation and difficult to deposit uniform layers on the surface of complex shaped components, therefore, it is hardly used in industrial application. Bad quality clads with porous and high roughness are always formed due to the evaporation or decomposition of residual binder. In addition, this process usually has a small processing window. Therefore, two step processes always present lower productivity and higher costs when comparing to the single step ones. Generally, injecting the feedstock directly into the melting pool is preferred [41-42, 45-46].

2.5.2.2 One-Step Laser Cladding

Laser Cladding by Wire Feeding

In this process, wires are fed into the melting pool through a ceramic drum usually to produce a layer of clad. Wire feeding is useful in cladding rotationally symmetric components that can be rotated such that the surface can be clad in one continuous track [44]. Due to the feeding mechanisms, it is essential to use a wire that have been strengthened and stored without plastic deformation to guarantee stable feeding [43, 47-48]. This approach seems advantageous because it is a single step process and material use efficiency is higher. The wire feeding nozzle must be positioned close to the melt pool to ensure accurate feeding of the material to the proposed area. Besides, the wire must be carefully controlled so it will not disturb the melting pool. A problem with using wire is that the laser beam is partially shielded from the melt pool by the solid wire and the laser energy is poorly absorbed by the wire, thus, the results tend to have limited reproducibility. In summary, the wire feeding process has some major drawbacks. On one hand, both the wire feeding rate and dilution are difficult to be controlled. On the other hand, low surface energy and bonding strength, porosity and cracks are easily emerged [41, 44].

Laser Cladding by Paste

In laser cladding by paste, a stream of additive material in a form of paste is injected on the substrate which is normally a little bit ahead of the laser beam [49]. The paste consists of the powder particles mixed with a suitable binder. However, the binder must be dried within a short time while the powder still keeps compact, otherwise, the particles would be blown away by the shrouding gas. Therefore, a special paste feeding system needs to be carefully designed for this process. Extreme sensitivity of this process to disturbances, high porosity and difficulties in paste feeding mechanism limit its application [43].

Laser Cladding by Powder Injection

In laser cladding by powder injection, the clad material is injected as powder instead of wire into the melting pool to produce a layer with a laser beam. A powder feeding system must be used. A typical powder feeding system involves a powder feeder, powder delivery tubes and a powder feed nozzle. Special powder feeders have been designed for laser cladding [50-51], but powder feeders for plasma spray are more often applied. The powder feeder can be categorized into gravity feed and carrier gas propelled. The carrier gas feeder is most commonly used. Powder delivery tubes convey the powder to the nozzle by a carrier gas and the powder feeding nozzle is classified as either lateral or coaxial. In lateral powder feeding, particles are injected into interaction region from one side without preheating. Different cladding directions lead to completely different local cladding conditions while the powder stream is injected off-axis from the laser beam. When the powder stream is fed to the molten pool created by the laser beam from the front, the powder utilization efficiency is the maximum compared to the other feeding locations [45, 52]. Therefore, in terms of this process, such a feeding system has certain limitations. First, it is difficult to align the location of the powder delivery with respect to the laser beam center. This positioning is very critical, and a small deviation will greatly decrease the powder utilization efficiency, and lead to a poor quality of cladding tracks. Moreover, this technique does not work well for complex geometric patterns which require multidirectional motions [53]. Several designs of coaxial nozzles were reported [54-56]. In a coaxial feeding nozzle, the focused laser beam passes through a central cone which is kept unobstructed by a

flow of argon, and the powder is transported by a flow of inert gas through an outer cone. A concentric powder stream is injected from all radial directions during the coaxial laser cladding process. Equivalent tracks are fabricated independent of cladding directions perpendicular to the laser beam. Therefore, coaxial laser cladding is more widely used for industrial purposes. This advantage of coaxial laser cladding is employed in the formation of metallic parts from 3D designs.

2.5.3 Clad Dimensional Characteristics

Figure 2.4 shows a typical cross section of a clad bead perpendicular to the cladding directions and defines the geometrical quantities used for laser track characterization: W_H is the width of the HAZ, W_C is the width of the clad track, H_C is the clad height, H_D is the depth of the dilution, H_H is the depth of the HAZ.

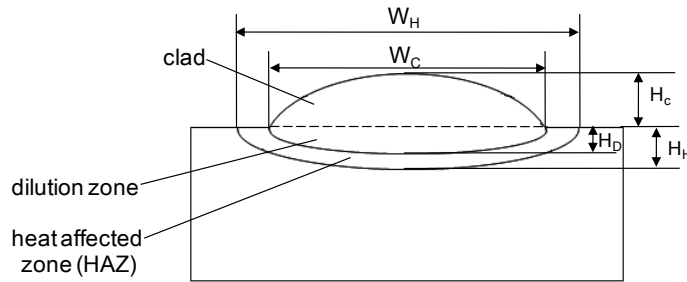


Figure 2.4 A typical cross section of a clad bead perpendicular to the cladding directions.

2.5.4 Important Parameters in Laser Cladding

The laser cladding operational window is usually defined as laser power P , scanning speed V and powder feeding rate F . Several additional process parameters such as laser beam spot size D_b , laser beam energy distribution, amount and sort of shielding and carrier gas, size, speed and feeding direction of powder particles, etc., play also a role. A complete description of the laser

cladding technique with injecting powder into a laser melt pool is rather complex because of numerous interactions (laser beam/powder, laser beam/substrate, powder stream/melt pool, powder stream/ solid substrate, etc.) with different physical phenomena (mass and heat transfer, fluid flow, phase transformations, etc.) involved [45].

Since there are many parameters involved in LC which are strongly coupled with each other, the energy input per unit area ($E = P/ VD_b$) and the mass of injected powder per unit area ($G=F/ VD_b$) are considered to be two important combined process parameters for the quality of the clad [57].

Dilution

The dilution quantifies the relative amount of the substrate that has been molten during the cladding process and mixed with an additive material. Although, for successful cladding some dilution between the coating and substrate is always required to ensure a good metallurgical bond, the fact that the high dilutions may degrade coating properties requires that it stays reasonable low. According to the specified parameters in **Figure 2.4**, the dilution is

$$dilution = \frac{H_D}{H_C + H_D}$$

Laser Pulse Shaping

The laser beam can be applied as continuous wave (CW) or as pulsed wave. In the form of pulse wave, several parameters associated with the shape of pulses are defined: laser pulse energy E_0 , laser pulse width (laser pulse duration) t , laser pulse frequency f , average power P_0 and duty cycle C . These parameters which are shown in **Figure 2.5** can be expressed by

$$C = ft \quad (2.1)$$

$$P_0 = E_0 f \quad (2.2)$$

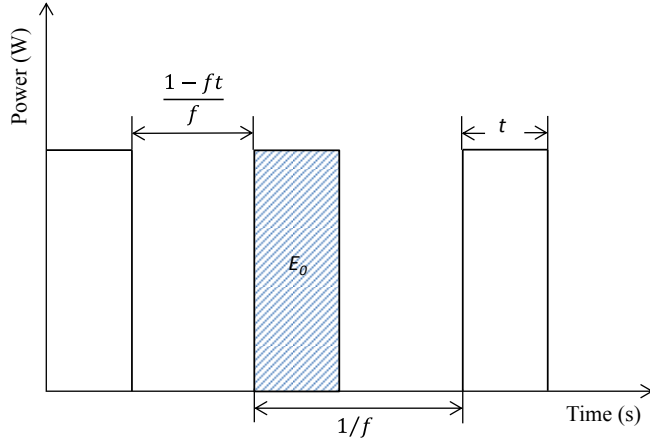


Figure 2.5 Laser pulse shaping.

Due to the numerous parameters involved in the process, two combined parameters, effective energy density E_{eff} (J/ mm²) and effective powder deposition density PDD_{eff} (g/ mm²), are introduced [3, 58-59] to simplify this process and expressed by

$$E_{eff} = \frac{P_0}{A_{eff}} \quad (2.1)$$

$$PDD_{eff} = \frac{Fft}{A_{eff}} = \frac{FC}{A_{eff}} \quad (2.2)$$

where A_{eff} is the effective area per second which is irradiated by the laser beam and powder stream (mm²/ s). E_0 is the pulse laser energy (J), F is the powder feeding rate (g/ s), f is the laser pulse frequency (Hz) and t is the laser pulse duration (s). The substrate velocity but also the pulse characteristics of the laser determine the effective area per second. Providing the percentage overlap of the laser spot on the substrate is high (i. e. ≥ 80 %), the irradiated area per second can be expressed as

$$A_{eff} = \begin{cases} \frac{\pi D_b^2}{4} + VD_b - 2f \left[\frac{1-ft}{f} V \frac{D_b}{2} - \frac{1-ft}{2f} yV - \frac{D_b^2}{4} \left(\frac{\pi}{2} - \sin^{-1} \frac{2y}{D_b} \right) \right] & \text{for } D_b > \frac{1-ft}{f} V \\ \frac{\pi D_b^2}{4} f + D_b Vft & \text{for } D_b \leq \frac{1-ft}{f} V \end{cases} \quad (2.3)$$

where

$$y = \sqrt{\frac{\pi D_b^2}{4} - \left(\frac{1-ft}{2f}V\right)^2}$$

D_b is the spot size of the laser beam on the substrate surface (mm), V is the scanning velocity of the laser head (mm/ s) and A_c is the half uncovered area of a rectangle created by two successive laser pulses (**Figure 2.6**).

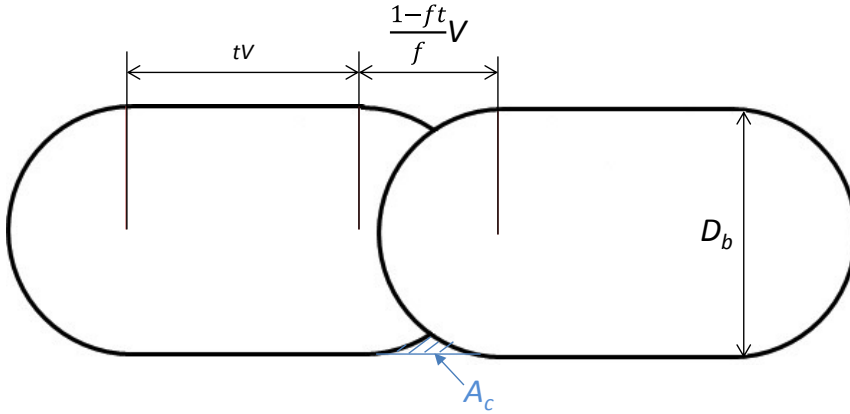


Figure 2.6 A schematic of the affective area of cladding created by successive laser pulses.

The inherent assumption in Eq. (2.2) is that, when the laser is off no powder is deposited on the substrate, due to the absence of energy provided by the laser. This assumption is introduced through the inclusion of the duty cycle (i.e. ft) in Eq. (2.2). This assumption is not completely valid since residual heat from the previous pulse may allow some powder melting and deposition. A critical ratio between energy and powder deposition density is required to achieve high quality clads [58]. If cladding conditions produce a low ratio, porosity and/ or poor bonding occurs.

$$r = \frac{E_{eff}}{PDD_{eff}} = \frac{P_0}{FC} = \frac{P}{F} \quad (2.4)$$

where r is the ratio between energy and powder deposition density (J/ g).

2.5.5 Non-invasive Thermal Imaging Techniques

A two dimensional (2D) temperature mapping is useful to optimize the cladding parameters. Especially if the surface structure is non-uniform, cooling of the tracks could be hindered to some extent leading to non-uniform temperature distributions. The non-uniform temperature distribution indicates that the injection conditions were not properly adjusted. On the other hand, the smooth and regular shape of temperature distribution corresponds to the well-optimized cladding [60].

To date, some research has been done to detect and monitor the temperature by applying non-contact thermal imaging techniques during the laser processing. Thermocouple and imaging techniques were used to monitor the thermal signature during the laser rapid forming process, and study the solidification behavior, residual stress, and microstructural evolution which were determined by the thermal history [61]. Temperature measurement by a pyrometer was carried out and the control of the laser power was realized [62]. The temperature of the formed layer by an IR pyrometer was measured and the powder efficiency through an inverse calculation of the boundary temperature obtained from observed surface temperature was estimated [63]. The temperature of the molten pool in the process of the laser rapid forming with a two-color infrared thermometer and the influences of the laser processing parameters on the temperature of molten pool was investigated [64].

Black-Body Radiation

Each body with a temperature above the absolute zero (0 Kelvin) emits an electromagnetic radiation from its surface, which arises from the motion of atoms which make up the body. In 1879, Stefan proposed a law that related the total energy radiated from a body to its temperature which can be expressed by means of the following equation:

$$R=\sigma\epsilon T^4$$

where R is the total thermal radiation per unit surface area of the body, σ is the Stefan's constant, ε is the emissivity which depends on the nature of the emitting surface and T is the absolute temperature.

A black body is a radiator, which absorbs all incoming radiation and shows neither reflection nor transmissivity.

$$\alpha = \varepsilon = 1$$

where α is called absorptivity.

The total radiation emitted by a black-body according to Stefan's law is:

$$R = \sigma T^4$$

The entire emitted radiation of a black body within the overall wavelength range increases proportional to the fourth power of its absolute temperature.

Real Body Radiation

The intensity of infrared radiation depends on the temperature as well as on the radiation features of the surface material of the measuring object. The emissivity is used as a material constant factor to describe the ability of the body to emit infrared energy. The emissivity depends on the material, its surface, temperature and wavelength. Many objects consisting of nonmetallic material show a high and relatively constant emissivity independent from their surface consistency, at least in longwave ranges. If the emissivity chosen is too high, the infrared thermometer displays a temperature value much lower than the real temperature of the measuring object. A low emissivity carries the risk of inaccurate measuring results due to interference of infrared radiation emitted by background objects.

2.5.6 Traditional Applications

Current trends of laser cladding are to produce multifunctional protective coatings for the modification of surface properties, such as, wear and corrosion resistance, abrasion and thermal resistance, or the repair of critical components with a laser beam [65-68]. The majority of work is the metallic coating production by laser cladding process for aerospace, medical and automotive industrial applications. Nickel-based superalloys [69-74], titanium-based alloys [75-78] and cobalt-based alloys [79-81] are some of the popular alloys that are deposited on different substrates to improve the substrate capability as wear and high temperature resistance. With high speed cladding and the characteristic of rapid solidification processes, extremely homogeneous structures could be obtained on the surface of work pieces [82-83]. Recently, production of glassy metallic layers which provide superior resistance against wear and corrosion by laser cladding was reported [84]. Bioceramics coating on titanium alloys applied in orthopedic implants was also conducted by laser cladding [85].

A new and increasingly important application of laser cladding is rapid fabrication of complex components and tools in additive manufacturing. With this technology, high value tools and components can be produced with low manufacturing cost, good surface quality and a short manufacturing time [86]. Additive manufacturing technologies allow an accurate model of a previously designed in a computer without the need for conventional manufacturing techniques, and the production time is significant reduced by 40 percent with laser cladding process [87-88].

2.5.7 New Applications

Contrary to the traditional laser cladding process, type K thermocouple (TC) sensors fabricated with this technique without altering the surface structures of the substrate is described in this work. Several advantages are possessed by the produced TC sensors, such as neither vacuum processing nor application of masks as well as short-time processing. Feature sizes achievable with this approach are in the range of several ten microns. The resistivity values of the clad TCs are estimated and compared to that of the commercial standard K-type TC. The thermal and

electrical performance of manufactured TC sensors is also evaluated and characterized at high temperatures.

3. Experimental Methods

3.1 Concept of Embedded Thermocouple (TC) Sensors

The aim is to fabricate functional electrical structures within layered TBC systems: electric conductive structures need isolation otherwise a short circuit will occur; sensor structures have to be isolated against the metallic substrate by at least a thin ceramic layer. Therefore, a thin layer of a TBC ceramic material is used as the substrate. Another ceramic layer (again TBC utilized) to protect sensor structures from harsh environment is applied (not strictly necessary); if insulation against each other by ceramic in between is possible, several sensors in different locations and/or height within the same ceramic coating layer of the same component could be implemented. Thereby, sensors monitoring surface temperature distribution or the heat flux through a coating can be realized. Typically such embedded thermocouple sensors will be located close to the ceramic top coat/ bond coat interface, the interface temperature which determines the thermally grown oxides (TGO) growth rate can be approximately measured. Hence, the life time of TBC system would be further evaluated. **Figure 3.1** displays the framework of one embedded thermocouple sensor.

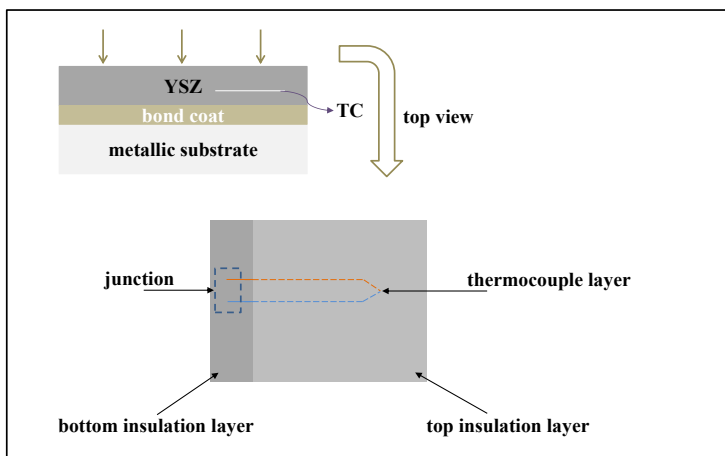


Figure 3.1 Concept of one embedded thermocouple sensor.

3.2 Substrate Materials

Since Ni-based superalloys possess excellent high temperature corrosion resistance and mechanical properties, they were widely used on gas turbine engines. Inconel 738 LC was studied as the initial metallic substrate. Much cheaper stainless steel was employed as the candidate substrate material for those experiments aimed for process optimization and where no subsequent heat treatment has been planned.

3.3 Feedstock Selection

For the thermal spray and the laser cladding processes, powderous feedstocks have been used. Amdry 386 (Oerlikon Metco, Wohlen, Switzerland), composed of Ni-21Co-17Cr-12Al-1Y, was selected as the bond coat material which was manufactured by vacuum plasma spraying.

Both insulation layers made of $\text{ZrO}_2\text{-}8\text{Y}_2\text{O}_3$ (Oerlikon Metco 204NS, Wohlen, Switzerland) were produced by APS process with standard spraying parameters.

Nitrogen gas atomized type-K thermocouple powders provided by Sandvik Osprey company (Sandvik Osprey, United Kingdom) were chosen as the candidate thermocouple sensor materials due to its high output voltage and a wide working range of temperatures. Alumel (Ni-2Al-2Mn-1Si) and chromel (Ni-10Cr) create a circuit with negative and positive polarities for the K type thermocouple.

3.4 Thermal Spray Processes

3.4.1 Vacuum Plasma Spraying (VPS)

Vacuum plasma spraying with a F4 plasma torch (Oerlikon Metco, Wohlen, Switzerland) was applied to deposit a 150 μm NiCoCrAlY bond coat, which is directly coated on the metallic substrate. **Figure 3.2** shows the VPS device (Oerlikon Metco, Wohlen, Switzerland).



Figure 3.2 VPS facility.

3.4.2 Atmospheric Plasma Spray (APS)

Both insulation layers with 17 % ~ 18 % porosity were produced from a commercially available YSZ powder (Oerlikon Metco 204NS) and these layers were deposited by APS process in a Multicoat facility (Oerlikon Metco, Wohlen, Switzerland) with a three-cathode TriplexPro™ 210 gun, as shown in **Figure 3.3**. The bottom YSZ layer was deposited with a thickness of about 200 μm and the top YSZ layer with variable thicknesses. Before coating, the metallic substrate was previously sand-blasted with alumina particles with an average size of 0.71 μm and ultrasonically cleaned in an ethanol bath. The stainless steel plate coated with 200 μm thickness thermally sprayed yttria partially stabilized zirconia (8YSZ, $\text{ZrO}_2\text{-}8\text{Y}_2\text{O}_3$) coatings was used as the substrate for the subsequent laser cladding, the dimension of which was about 50 mm (length) \times 50 mm (width) \times 3 mm (thickness). The substrate was cleaned in an ethanol bath and dried with compressed air before deposition of the sensor structures.

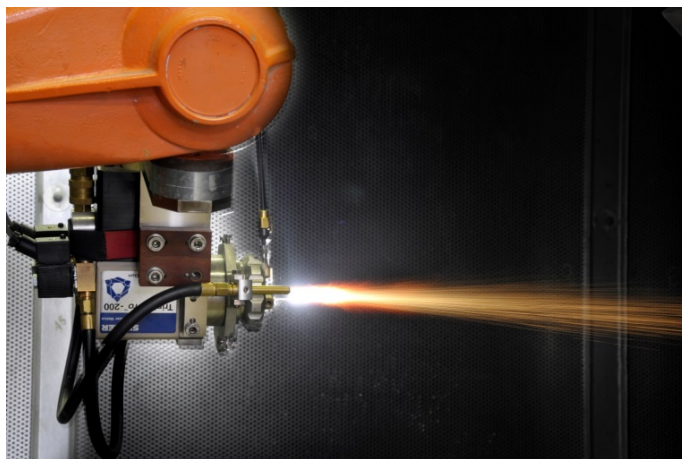


Figure 3.3 A Oerlikon Metco TriplexPro 210 APS plasma gun in operation

3.5 Laser Cladding Technology

The deposition of type K thermocouple sensors was performed by coaxial laser cladding technique. The experiments were conducted with a 400 W Nd: YAG laser system TruLaser Cell 3008 (Trumpf, Germany) combined with a fiber laser TruFiber 400 (Trumpf, Germany) as the power source. A three-axis CNC (computerized-numerical-control) table was employed to move the laser beam and the powder feeding system over the substrate with a controlled scanning speed. A coaxial powder nozzle Coax 8 (ILT, Aachen, Germany) and a powder hopper (TWIN-10-2, Oerlikon Metco, Wohlen, Switzerland) as a powder feeder were used. Argon was used on one hand as carrier gas to deliver both thermocouple powders respectively from the powder hopper and on the other hand as shielding gas to protect the process from oxidation while the laser beam scans the surface of the substrate. **Figure 3.4** shows the laser cladding device and the coaxial jet nozzle with injected powder.

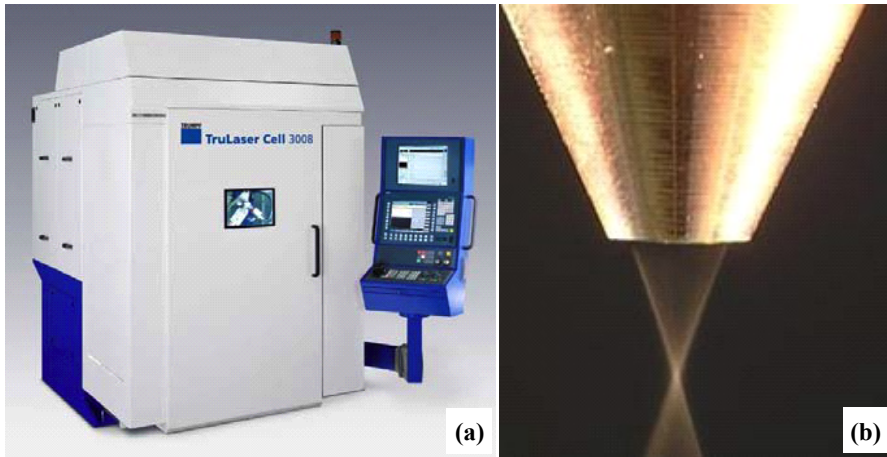


Figure 3.4 Experimental setup: (a) laser system TruLaser Cell 3008 and (b) coaxial jet-nozzle with injected powder.

The spot size was varied by adjusting the position of internal lens of the laser beam. The variation of the stand-off distance S , shown in **Figure 3.5** changes with the different focus position of the laser beam while the divergence angle of the laser beam keeps constant. The

focus position was 9.0 mm when the laser beam was focused 7.0 mm below the laser nozzle (S=0). With the increase/ decrease of stand-off distance, the focus position was increased/ decreased correspondingly.

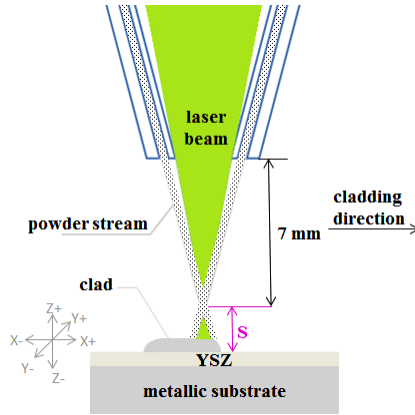


Figure 3.5 Schematic of laser cladding process.

The powder feeding rate is varied by controlling the disk rotation speed of the rotating disk. A disk with a notch of 5 mm \times 0.6 mm for the powder hopper (**Figure 3.6**) was applied. A funnel-shaped powder feed geometry was obtained as seen in **Figure 3.4b**. The powder focus position was 7 mm underneath the coaxial jet nozzle and the minimum powder focus size was about 0.2 mm.

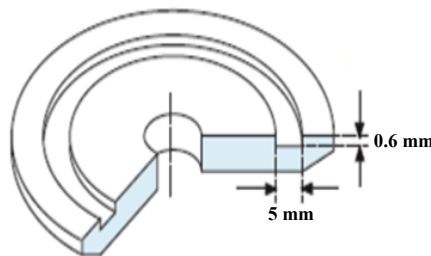


Figure 3.6 Disk for the powder hopper.

3.6 Characterization Techniques

3.6.1 Particle Size Distribution

The particle size distribution of both feedstock powders was characterized by Particle Analyzer Horiba LA-950V2 (Horiba Europe GmbH, Germany). The LA-950 measures light scattering patterns of the particle sizes with the interaction of the laser light. The scattering-degree increases with decreasing particle size and vice versa. The number of particles is represented by the intensity of the scattered light. It is able to measure the particle size over a range of 0.01 μm -3000 μm .

3.6.2 Micro-spot Monitor (MSM)

The spatial power density distribution of the laser beam which is one of the important factors to affect the track geometry was measured by a Micro-spot Monitor (MSM, Primes, Germany). The MSM is a camera-based, beam diagnostic system capable of measuring wavelengths from 248 nm to 1100 nm. The device is used for the analysis of focused laser beams. It measures the spatial power density distribution within the focus range of the processing optics. The measurement is done using a diffraction limited objective projecting the image of the power density distribution onto a CCD-sensor.

This device was set right beneath the laser head nozzle with a certain distance. By varying the position of the lens within its focus range, the spatial power density distribution could be characterized. The spot size and center as well as the focus position of the laser beam could be further derived.

3.6.3 Infrared (IR) Camera

An infrared camera Optris PI200 (Optris GmbH, Germany) equipped by an ZnSe sensor with 7.5 to 13 μm band pass arranged on 160×120 pixel array with up to 128 Hz, was applied to monitor the surface temperature for a travelling speed up to 400 mm/ min. The measuring range is up to

1500 °C with an accuracy of ± 2 °C. This IR camera was positioned 50 mm from the deposition area with an integration time of 20 ms and a single pixel size of 0.13 mm.

An infrared camera (FLIR SC655, Germany) equipped by a FOL25SF10 lens with 640×120 pixels was applied to monitor the surface temperature at higher travelling speeds up to 1500 mm/min. The measurable temperature range is up to 2000 °C. The integration time and single pixel size are 5 ms and 0.18 mm, respectively.

3.6.4 Cyberscan Topographer

Surface topography, dimensions, cross-sectional area and roughness measurement of cladded tracks were carried out with a Cyber Scan CT200 (Technologies GmbH, Ingolstadt, Germany) non-contact laser scanning inspection system equipped with a confocal laser sensor LT-9010M (Keyence Deutschland GmbH, Neu-Isenburg, Germany) and a laser Triangulations sensor DRS 8000 (Cyber Optics Ltd., North Yorkshire, UK).

3.6.5 Light Microscopy and Confocal Laser Microscopy

For the investigation of macroscopic and cross sectional structures of tracks after laser cladding, a stereo-microscope SZX12 (Olympus, Japan) and a laser microscope VK-9710K (Keyence, Japan) were used, respectively. By illuminating the sample at an angle from the side under the stereo microscope, shadows of cladded tracks could be observed which implied whether homogeneous and well-bonded tracks could be obtained or not. A HAZ can be analyzed with the laser microscope on cross-sections of deposited clads.

3.6.6 Ohmmeter and Four Probe Tester

The electrical conductivity properties of cladded tracks were first roughly estimated with an Ohmmeter (Meterman, Germany), if conductive, a self-assembled direct-current Four Probe

Tester was utilized to further examine the resistance (**Figure 3.7**). The resistivity of clad tracks could be calculated with the following equation:

$$\rho = \frac{R \cdot A}{L}$$

where R is resistance (Ω), A is the cross-sectional area (m^2) and L is the length (m). The cross-sectional area is estimated under the Cyberscan topographer and the length is the distance between voltage sense connections.

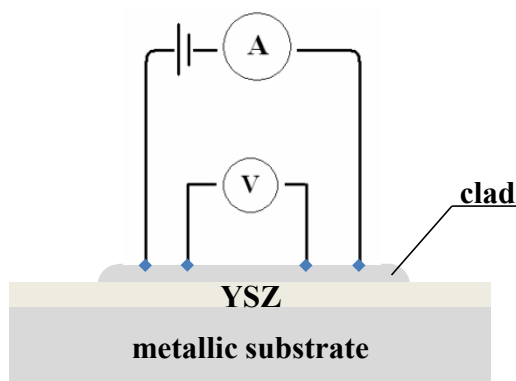


Figure 3.7 Schematic of four point resistance measurement of one clad.

3.6.7 Measurement of the Seebeck Coefficient

The change in material electromotive force (EMF) with respect to temperature is called Seebeck coefficient or thermoelectric sensitivity. Slight variations will cause large deviations in reading. The thermal sensitivity (Seebeck coefficient) of clad thermocouples before and after embedding into the second YSZ layer was measured in a furnace at temperatures up to 500 °C. A data acquisition system ALMEMO (AHLBORN, Germany) accompanied by a transducer was applied and attached to the tips of clad thermocouples by applying commercial type K thermocouple wires. The measuring point temperatures at the junctions should be kept the same

to have the reliable temperature reading. **Figure 3.8** illustrates the setup for the Seebeck coefficient measurement.

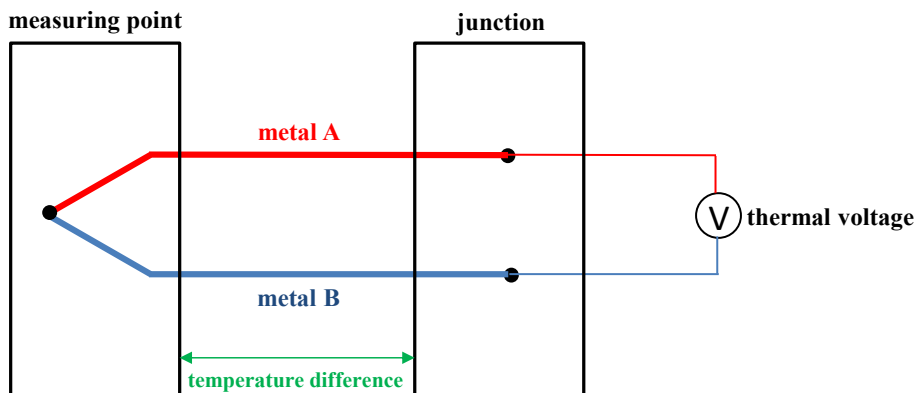


Figure 3.8 Seebeck coefficient measurement setup.

3.6.8 Shear Force Measurements

The bonding strength between cladded tracks and the substrate plays also an important role for the following embedding with a second ceramic layer. Therefore, the adhesion strength between cladded tracks and substrate was evaluated with a shear force device (ATP Messtechnik GmbH, Germany) in **Figure 3.9** at ZEA-1, Forschungszentrum Jülich. The tip of the shearing knife should be positioned just contact with the substrate surface without any load. A certain load is applied until the tracks are able to be removed.

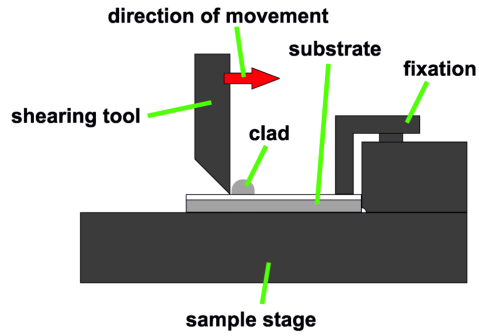


Figure 3.9 Shear force measurement device.

4. Experimental Results and Discussion

4.1 Feedstock Characterization

The particle size distribution for both bond-coat and YSZ insulation layer was measured by static laser scattering. The average diameter for the bond coat is $24\ \mu\text{m}$ ($d_{10}=15\ \mu\text{m}$, $d_{90}=36\ \mu\text{m}$) and for the YSZ layer is $54\ \mu\text{m}$ ($d_{10}=28\ \mu\text{m}$, $d_{90}=85\ \mu\text{m}$), respectively.

The particle size of the type-K TC powder is very significant for the laser cladding process because the fluidity of the powder influences the quality of the clad. Therefore, the particle size distribution for the two powders was also analyzed by static laser scattering which is shown in **Figure 4.1**. The diameter for the alumei powder is in the range of $2.6\text{--}20\ \mu\text{m}$ with a mean particle size of $7.4\ \mu\text{m}$ and for chromel powder it is in the range of $3.5\text{--}35\ \mu\text{m}$ with a mean particle size of $12.1\ \mu\text{m}$, respectively. Considering the flowability of the powders, first experiments showed that chromel powder worked very well, but alumei powder had quite poor fluidity. This problem was solved after drying in a furnace at $150\ ^\circ\text{C}$ for 24 h.

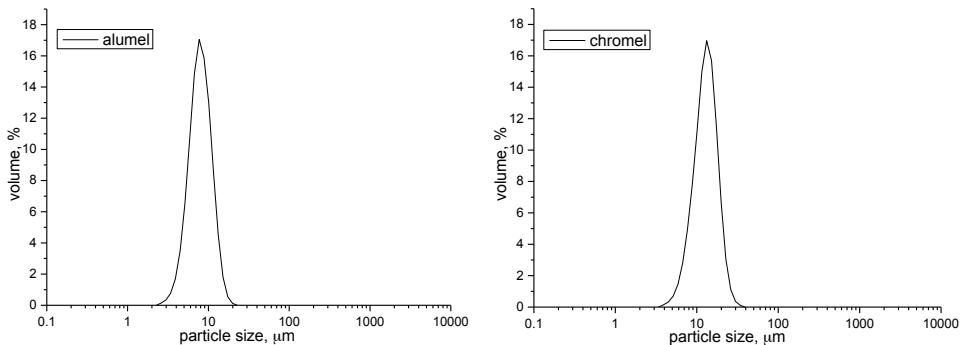


Figure 4.1 Particle size distribution of alumei powder (left) and chromel powder (right).

4.2 Laser Beam Characterization

4.2.1 Spatial Distribution of the Laser Beam

The spatial power distribution of the laser beam was measured by a MSM. The results show that the laser beam intensity follows a Gaussian distribution with a Gaussian mode TEM_{00} when applying the focus position from -4 mm to 16 mm. **Figure 4.2** shows one example of the spatial distribution of the laser beam at 9.0 mm focus position. Detailed laser beam parameters are displayed in **Table 4.1**.

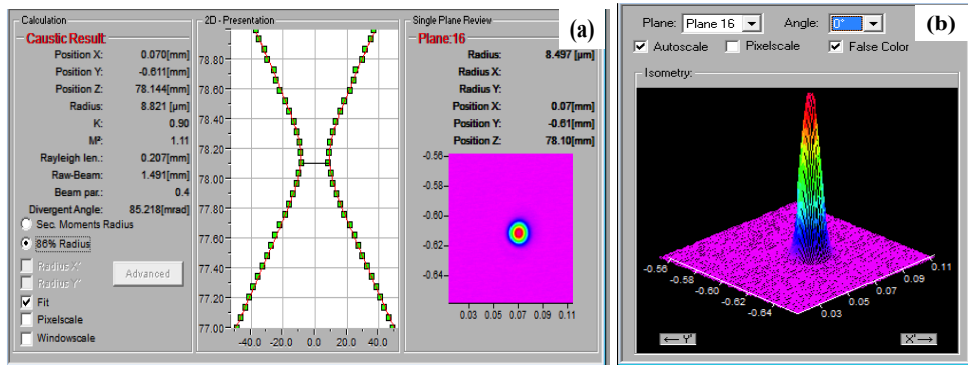


Figure 4.2 Laser beam analysis: (a) focalization plane determination and divergence of the laser beam, (b) spatial distribution of irradiance.

Table 4.1 Laser beam parameters.

laser beam mode	TEM_{00}	propagation factor k	0.90
spot size _{min}	17 μm	divergence angle θ	4.96°
quality factor M^2	1.11		

4.2.2 Spot Size Determination

Since the track width is strongly dependent on the spot size on the substrate [62], the relationship of the spot size and the focus position measured by the MSM is given in **Figure 4.3**. It can be seen that the minimum laser beam diameter is about 17 μm at 9.0 mm focus position and the spot size is linearly increasing accordingly when decreasing or increasing the focus position.

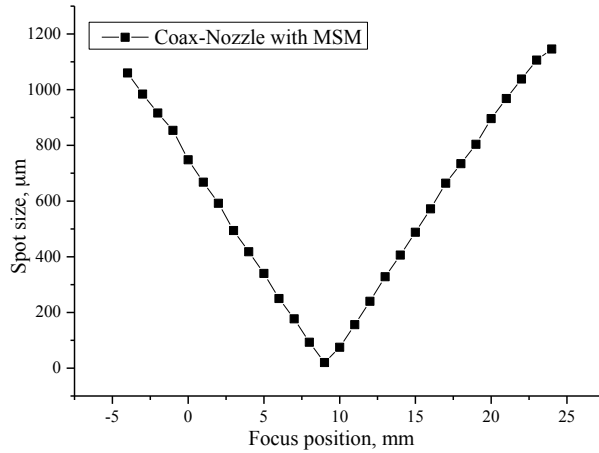


Figure 4.3 The relationship between the spot size and focus position.

4.3 Powder Feeding Rate

The powder feeding rate for both powders under the different disk rotation speed was separately measured by collecting powders at the nozzle exit for 5 minutes feeding into a clean bottle without activating the laser. The results are displayed in **Figure 4.4**.

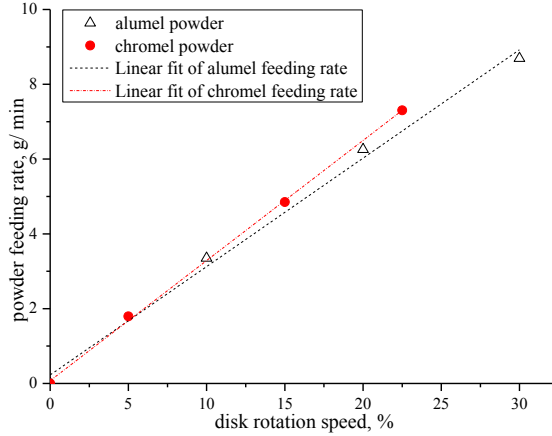


Figure 4.4 The relationship of powder feeding rate and the disk rotation speed of the powder feeder.

4.4 Deposition of K-type TCs with a continuous wave (CW) Laser

4.4.1 Deposition of Alumel Tracks

By limitations of the powder hopper, the minimum continuous and stable feeding rate is 5.0 % ($F=1.68$ g/ min) for the alumel powder. The necessary power to melt such an amount of powders was roughly estimated to be 29 W according to the following equation:

$$P \times t = F \times t [c_p \times (T_m - RT) + H_{fusion}]$$

where P is the necessary power, t is the cladding time, F is the powder feeding rate, c_p is the specific heat capacity of alumel, T_m is the melting point of alumel, RT is the room temperature and H_{fusion} is the latent heat of fusion for alumel powder. Since not all of the power would be absorbed by the powders, part of which is lost by the reflection by the metallic particles in-flight or by transmission, so the starting input power was 50 W. Laser cladding experiments were first carried out by varying the laser power from 50 W to 110 W while keeping the spot size, the scanning speed, the powder feeding rate, the carrier gas rate and the protective gas rate constant which were 984 μ m (focus position=-3 mm), 400 mm/ min, 1.68 g/ min, 10 l/ min and 10 l/ min,

respectively. The surface morphologies of the clads are displayed in **Figure 4.5**. From the top view, it can be seen that big beads much larger than the original particles were observed with powers at 50 W to 100 W what is supposed to be the low specific energy (energy per unit area) input. The laser heating of the substrate and the interaction between the molten powder and the substrate are restricted [89]. The size of the beads had the tendency to become smaller when increasing the laser power and the clad became quite smooth and continuous when increasing the power to 110 W.

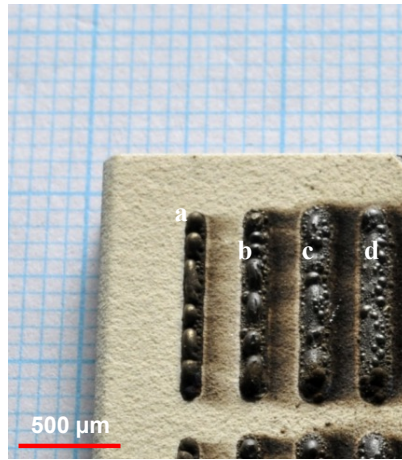


Figure 4.5 Surface morphologies of clads at different parameters from the top view. $V=400$ mm/ min, $D_b=0.984$ mm, $F=1.68$ g/ min, $V_p=V_c=10$ l/ min. (a) $P=50$ W, (b) $P=80$ W, (c) $P=100$ W, (d) $P=110$ W.

Figure 4.6 illustrates the behavior of the laser clad width as a function of the laser power. The track width displayed a strong dependence on the laser power and increased with increasing the laser power as a result of increased energy input per unit length. More particles were melted at the border of the laser spot. The track widths were in the range of 1.0 mm to 1.7 mm, a premature failure of TBCs would be caused because of intensive thermal expansion mismatch between metallic thermocouples and ceramic YSZ layer.

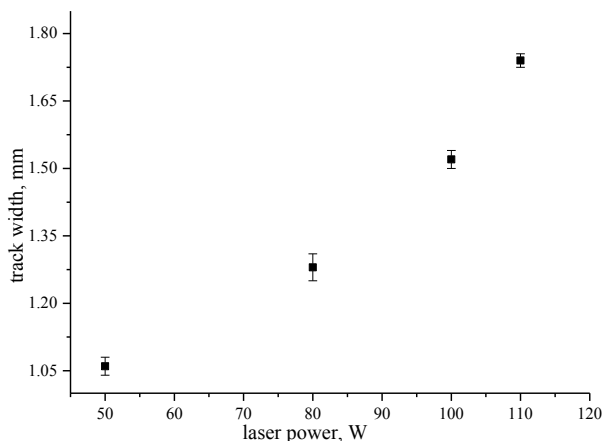


Figure 4.6 Laser clad width as a function of the laser power. $V=400$ mm/ min, $D_b=0.984$ mm, $F=1.68$ g/ min, $V_p=V_c=10$ l/ min.

4.4.1.1 Resistivity Analysis and Cross Sections of Cladded Aludel Tracks

Since one of the important characteristics for thermocouples is its electrical conductivity, the resistivity of cladded aludel tracks was roughly estimated. Results showed that only the thermocouple produced with 50 W power was conductive even though the surface morphology was wavy. The resistivity of the track in **Figure 4.5a** was estimated to be about $1.752 \mu\Omega \cdot m$. This is much larger than reported value $0.294 \mu\Omega \cdot m$ [90] which indicated that the track was inhomogeneous probably due to the defects and impurities at the grain boundaries of the bulk material.

In order to identify the mechanisms which lead to conductive or non-conductive, cross sections of the above deposited tracks along the cladding directions were prepared and investigated by a laser microscope. The micrographs are given in **Figure 4.7**. With the increase of the laser power, the influence to the substrate increased correspondingly. The tracks started to penetrate into the insulating YSZ coatings and were even buried in the YSZ coatings. The higher the laser power was, the deeper the tracks penetrated and more cracks emerged within the YSZ layers. It can be clearly seen that the upper part of YSZ coatings became dense (**Figure 4.7b-c**) which implied that remelting and resolidification of YSZ layers took place due to excessive energy input per

unit length. This amount of energy was not only absorbed by the injected particles but also by the substrate. The reason that the first track was conductive is the slight contact of the big beads. The beads in **Figure 4.7b-c** were intermittently and the track in **Figure 4.7c** started to be buried by the YSZ coating leading to these two tracks non-conductive. The last track in **Figure 4.7d** was totally buried and discontinuous that made this track non-conductive. The dense YSZ layer was transparent [91], so the deposited track in **Figure 4.7d** could still be recognized.

Figure 4.8 displays the depth of the HAZ plotted against the laser power. It can be seen that the dimension of the HAZ was highly related to the input laser power. When given a low laser power of 50 W, there was no obvious effect on the substrate. However, the HAZ was increased dramatically when increasing the laser power and spread the entire ceramic layer when increasing the laser power up to 110 W.

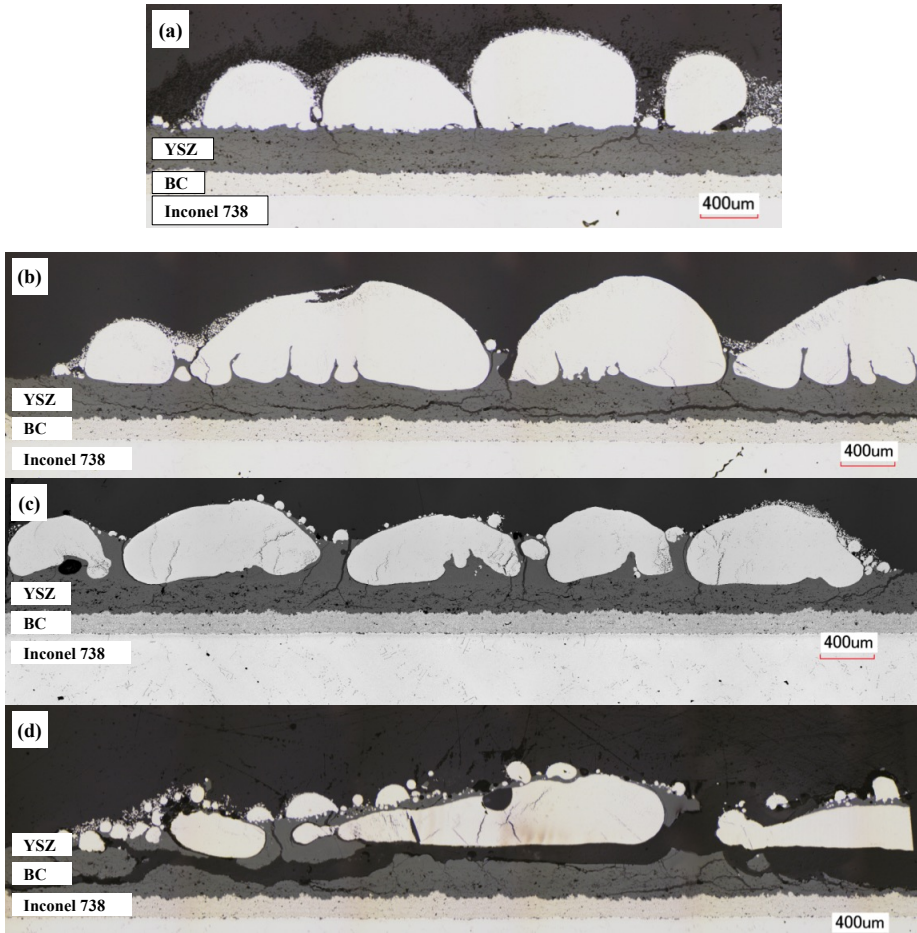


Figure 4.7 Cross sections of tracks produced with different process parameters under a laser microscope. $V=400$ mm/ min, $D_b=0.984$ mm, $F=1.7$ g/ min, $V_p=V_c=10$ l/ min. (a) $P=50$ W, (b) $P=80$ W, (c) $P=100$ W, (d) $P=110$ W.

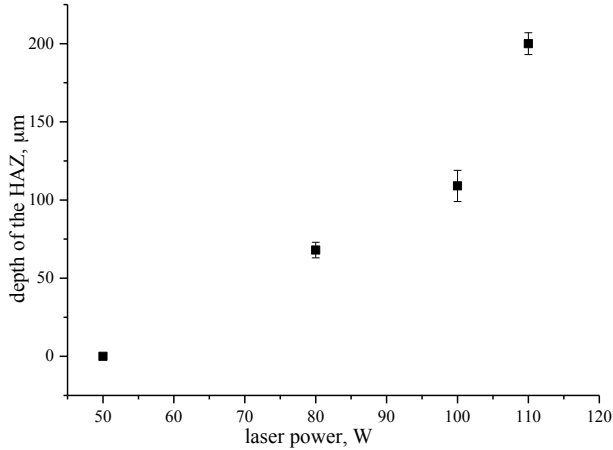


Figure 4.8 Influence of the laser power on the depth of the HAZ. $V=400$ mm/ min, $D_b=0.984$ mm, $F=1.68$ g/ min, $V_p=V_c=10$ l/ min.

4.4.1.2 Optical Diagnostics

An IR camera was applied during the laser cladding of the aluminel powder. In order to get the correct temperature reading (the temperature should not change within the integration time of one pixel), the maximum scanning speed should not exceed 400 mm/ min defined as one single pixel size divided by the integration time. In addition, to make sure that temperature could be accurately recorded, the area of homogeneous temperature should include at least three pixels, that is to say, the spot size of the laser beam should be larger than 0.39 mm in diameter. Based on the curve displayed in **Figure 4.3**, the focus position should be set from -4 mm to 4 mm or from 14 mm to 16 mm. Due to the limitation of this IR camera, the upper temperature is 1500 °C. If the brightness temperature (the brightness temperature of a non-blackbody target is defined as the temperature that would be measured from a blackbody having the same monochromatic luminance) exceeded 1500 °C under a given power, the power would be stopped to be increased.

2D temperature fields under the different laser power are shown in **Figure 4.9**, each image was chosen by taking a random snapshot. It can be seen that a better homogeneous temperature profile could be achieved with increasing the laser power.

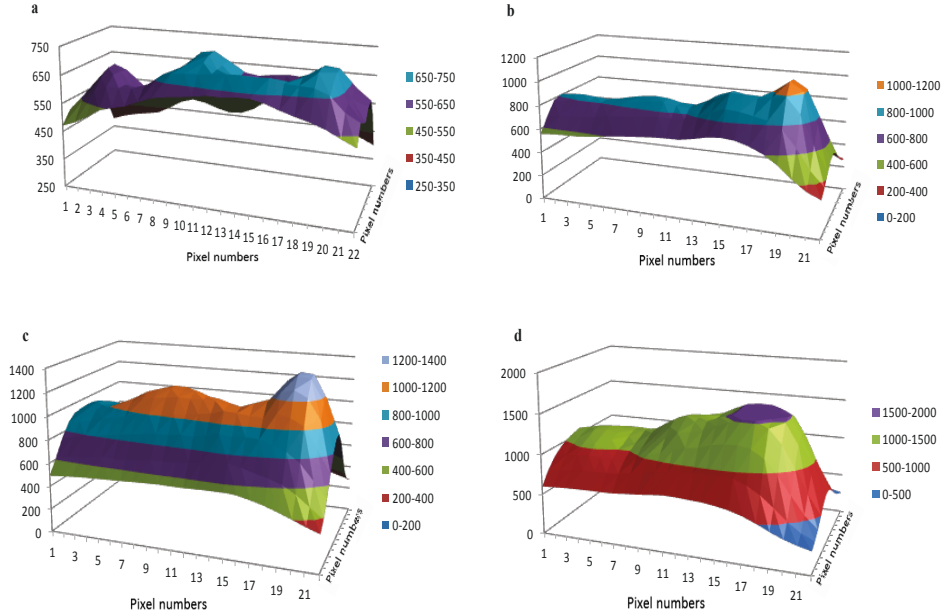


Figure 4.9 Two-dimensional temperature fields in coaxial laser cladding of aluminel on substrate; $V=400$ mm/min, $D_b=0.984$ mm, $F=1.68$ g/min, $V_p=V_c=10$ l/min, (a) $P=50$ W; (b) $P=80$ W; (c) $P=100$ W; (d) $P=110$ W.

In conclusion, critical defects like severe HAZ and cracks emerged after the first laser cladding experiments which destroyed the original microstructures of the TBCs, thus, the life time performance of TBCs would be degraded. Discontinuous clads were generated which need to be avoided to ensure the electrical conductivity of the cladded tracks. Furthermore, tracks in small dimensions are more suitable for the following embedding to create an in-situ temperature monitoring system in TBCs. Therefore, homogeneous tracks with little impact to the substrate and in small dimensions are desired to be deposited. It confirms that the application of IR camera is one of the useful tools to optimize the cladding process parameters. However, higher travelling speed than 400 mm/min cannot be applied due to the limitation of this IR camera, the following work was done without using it.

4.4.1.3 Optimization of Aludel Tracks

According to reported papers [46, 92], there are three different ways to reduce a deep substrate melting during the laser cladding process, by reducing the laser beam power, increasing the traveling speed or by displacing the irradiated surface from the focal plane of the laser beam. The main point for these three methods is to reduce the energy input per unit area at the substrate surface. Due to the limitation of this facility, the minimum power that can be achieved is 12 W. Increasing the scanning velocity increases the risk related to a loss of the electrical conductivity of clad tracks of morphological discontinuities. The third method was supposed to be the most effective way but undesired larger structures can be expected due to the defocused laser. Usually the reflectivity of a ceramic in a laser beam is lower and the absorptivity is higher than that of metallic materials, which might be one of the reasons for the large dimensions of the HAZ.

During the interaction between laser beam and powder, a part of the laser energy is absorbed, another part is reflected or scattered by the powder particles. If the size of a particle is sufficiently close to the laser wavelength, there exists apparently diffraction. Most of the energy reflected or scattered from the particles leaves to the ambient, while a small amount irradiates the work-piece or other particles. Some of the energy absorbed by the particles could also be lost by convection or irradiation from these particles to the surroundings [93-96]. When the laser beam passes through the clouds of powder particles, some laser energy is absorbed and reflected, reducing its intensity and changing its distribution. Thus, increasing the powder feeding rate is an alternative way to reduce the laser intensity at the substrate level and might be helpful to decrease the dimension of the HAZ. The larger the amount of particles above the substrate surface, the higher the possibility to reduce the dimension of the HAZ.

In order to make sure whether it is possible to decrease the dimension of HAZ or avoid the melting of the substrate by increasing the powder feeding rate, experiments were first conducted with a relatively low energy input per unit area of 2.1 J/mm^2 . A defocused laser beam of 16.0 mm focus position was applied and the laser beam was focused 7.0 mm above the substrate. **Table 4.2** gives the corresponding process parameters during laser cladding aludel powder. The laser power, travelling speed, laser beam spot size, protective and carrier gas rate were kept constant while the powder feeding rate was varied. When setting the feeding rate to 25.0 %, no

track was formed on the substrate surface after deposition, which meant the remaining laser energy after attenuation was insufficient to melt a certain amount of particles. The track with 20.0 % feeding rate was washed away by the cooling water during cutting with the cutting machine which indicated that the bonding strength between cladded alumel track and YSZ coating was very poor. Therefore, the powder feeding rate was further reduced to 14.0 % ($F=4.30$ g/ min). The track was sticking to the substrate and had a better bonding strength than the former tracks indicated by surviving the subsequent processing, like cleaning in the ultrasonic bath and eroding by cooling water during cutting.

Table 4.2 Laser cladding parameters for alumel powder.

	P (W)	V (mm/ min)	D_b (μ m)	E (J/mm^2)	F (%)
a	20	1000	572	2.1	14.0
b	20	1000	572		25.0
c	20	1000	572		20.0

* Protective gas and carrier gas rate: 10 l/ min.

A cross section of the first track along the cladding direction was prepared to make sure whether the dimension of the HAZ was reduced or not, as shown in **Figure 4.10**. It can be clearly seen that there was nearly no effect on the ceramic substrate after this process, in other words, increasing the powder feeding rate is beneficial to reduce the dimension of the HAZ.

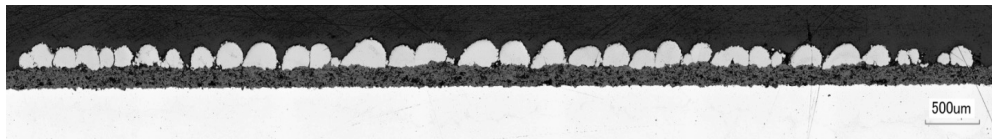


Figure 4.10 Cross section of the track with 14.0 % powder feeding rate for alumel powder. $P=20$ W, $V=1000$ mm/ min, $D_b=572$ μ m, $V_p=V_c=10$ l/ min.

4.4.2 Deposition of Chromel Tracks

Similar experiments were also performed with chromel powder. Corresponding parameters are given in **Table 4.3**. Only a low amount of chromel particles was bonded to the substrate when using with the same optimized parameters as above for the aludel clad. This might be caused by the higher reflectivity and larger average particles required more energy for melting the same amount of chromel powder than that of aludel powder. Therefore, the laser power was increased to 30 W. Parts of the tracks were detached when the feeding rate was higher than 14.0 % and the powder feeding rate was finally optimized to 13.5 %. **Figure 4.11** shows the cross section along the cladding direction of optimized chromel track. This track was unfortunately over-polished from the center, nevertheless, it is obvious that there was also no apparent effect to the substrate after laser cladding.

Table 4.3 Laser cladding parameters for the chromel powder.

	P (W)	V (mm/min)	D _b (μm)	F (%)	V _p (l/ min)	V _c (l/ min)
a	20	1000	572	14.0	10	10
b	30	1000	572	15.0	10	10
c	30	1000	572	13.0	10	10
d	30	1000	572	14.0	10	10
e	30	1000	572	13.5	10	10

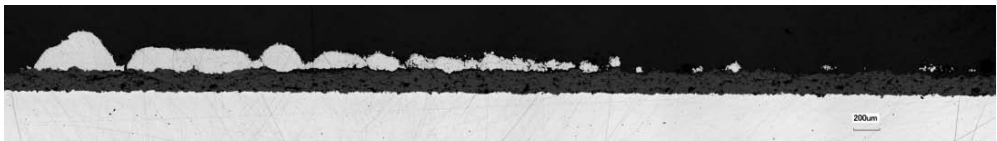


Figure 4.11 Cross section of cladded track for chromel powder under parameters of P=30 W, V=1000 mm/ min, D_b=572 μm, F=13.5 %, V_p=V_c=10 l/ min.

4.4.3 Preparation of K-type TC with Relatively Optimized Parameters

Sensors with smaller dimensions with low impact to the structural preference of the coatings are more desired. Since the bead width is determined by the spot size on the substrate [56], the beam diameter was decreased by decreasing the focus position of the laser beam. The spot size of a diameter of 156 μm was applied by setting the focus position to 11.0 mm and the laser beam was focused 2 mm above the substrate. In addition, the laser track width was also strongly dependent on the initial laser power [46]. Therefore, the input laser power was also reduced to 15 W. In this case, the energy per unit area is nearly three times larger than before. Hence, the powder feeding rate should be higher in order to reduce the HAZ. **Table 4.4** shows the used parameters for both powders. The other parameters were kept constants apart from the feeding rate. When the chromel powder feeding rate was higher than 21.5 %, detached tracks could be recognized by shadows observed in **Figure 4.12a-b**. Similarly, the alumel powder feeding rate was optimized to 30.0 % to prevent bonding problems (**Figure 4.12c-d**). However, the height with about 184 μm of track (6) in **Table 4.4** was much larger than that of the optimized track in **Table 4.3** of 96 μm . Taking into account this issue, parameters of the optimized track in **Table 4.3** were reconsidered as the optimized clad.

Table 4.4 Laser cladding parameters for both powders.

powder	track	P (W)	V (mm/min)	D _b (μm)	F (%)	E (J/ mm ²)
chromel	(1)	15	1000	156	25.0	5.8
	(2)	15	1000	156	23.0	
	(3)	15	1000	156	20.0	
	(4)	15	1000	156	21.5	
	(5)	15	1000	156	22.5	
alumel	(6)	15	1000	156	30.0	
	(7)	15	1000	156	40.0	
	(8)	15	1000	156	35.0	

* Protective gas and carrier gas rate: 10 l/ min.

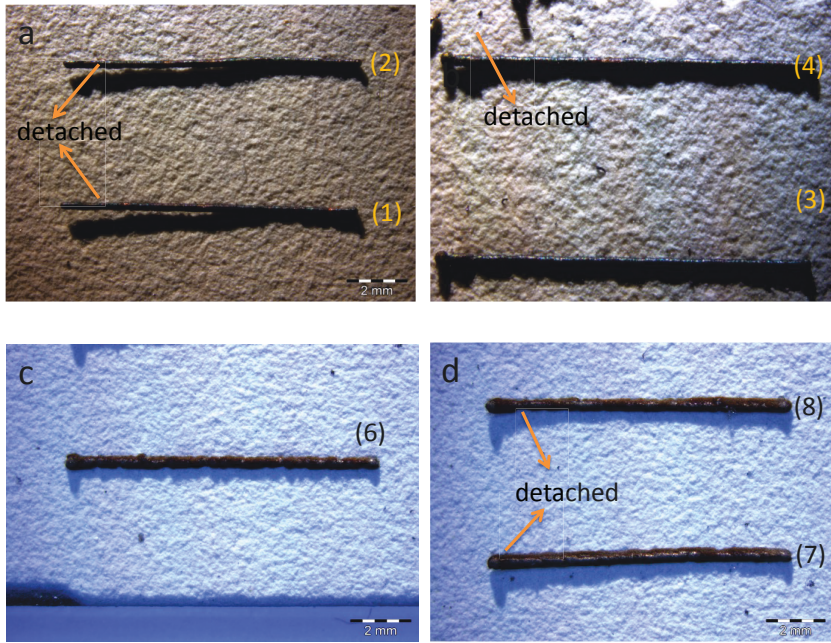


Figure 4.12 Stereo micrograph of cladded tracks. (a-b) chromel powder; (c-d) aludel powder. $P=15$ W, $V=1000$ mm/ min, $D_b=156$ μ m, $V_p=V_c=10$ l/ min. (1) $F=25.0$ %, (2) $F=23.0$ %, (3) $F=20.0$ %, (4) $F=21.5$ %, (5) $F=22.5$ %, (6) $F=30.0$ %, (7) $F=40.0$ %, (8) $F=35.0$ %.

Figure 4.13 displays the influence of the powder feeding rate on the track height for both powders. It can be seen that the track height increased from about 210 μ m to 240 μ m with the powder feeding rate from 30.0 % to 40.0 % for aludel powder. This might due to that more aludel particles were melted when increasing the mass of the powder per unit length input. But for chromel powder, the track height decreased from 230 μ m to 190 μ m with the powder feeding rate from 20.0 % to 25.0 %. The might related to the fact that more laser energy were lost by the flying particles when increasing the powder feeding rate. Less energy was remained after attenuation, therefore the height of the tracks decreased.

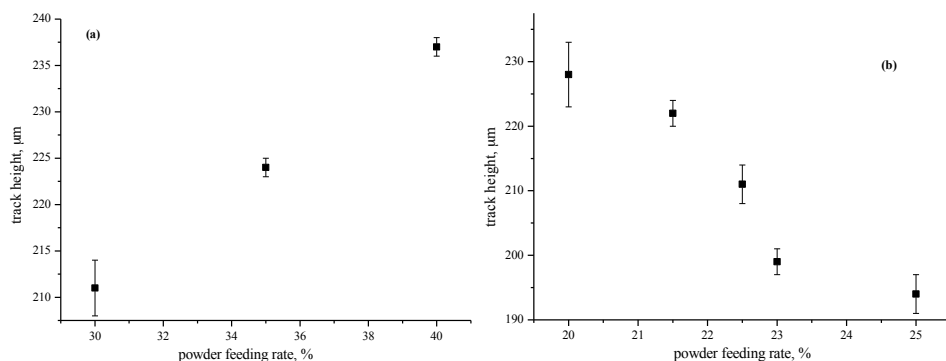


Figure 4.13 Influence of the powder feeding rate on the height of the tracks. $P=15$ W, $V=1000$ mm/ min, $D_b=156$ μm , $V_p=V_c=10$ l/ min. (a) alumel and (b) chromel.

The above two optimized thermolegs (alumel: $P=20$ W, $V=1000$ mm/ min, $D_b=572$ μm , $F=14.0$ %, $V_p=V_c=10$ l/ min; chromel: $P=15$ W, $V=1000$ mm/ min, $D_b=156$ μm , $F=22.5$ %, $V_p=V_c=10$ l/ min) were analyzed by the Cyberscan topographer in **Figure 4.14**. The surface morphology of alumel was not even what might be related to the poor wetting of the powder particles. Unlike the cladbed alumel track, a chromel track with very homogeneous morphology was gained. Good wetting behavior was supposed to be the reason due to the chromium. During the process, chromium has the tendency to segregate at the interface and form Cr-O clusters, which are beneficial for the improvement of the wetting behavior [97]. Besides, it can be seen from the cross-sectional microstructure in **Figure 4.15** that no additional influence on the substrate was visible.

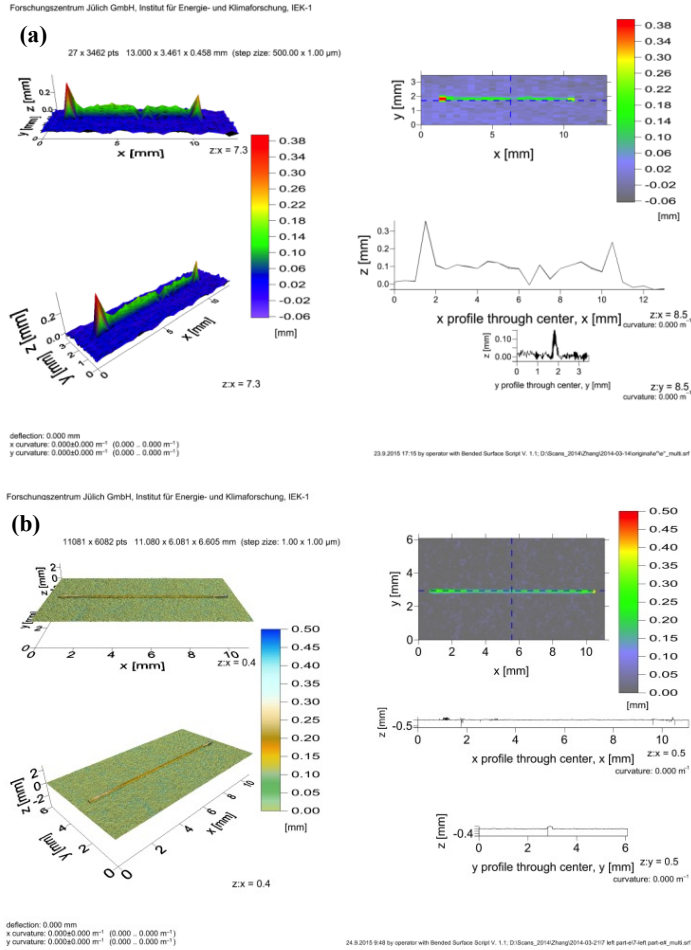


Figure 4.14 Micrographs of clad tracks with optimized parameters under a laser microscope. (a) alumel, $P=20$ W, $V=1000$ mm/ min, $D_b=572$ μ m, $F=14.0$ %, $V_p=V_c=10$ l/ min; (b) chromel, $P=15$ W, $V=1000$ mm/ min, $D_b=156$ μ m, $F=22.5$ %, $V_p=V_c=10$ l/ min.

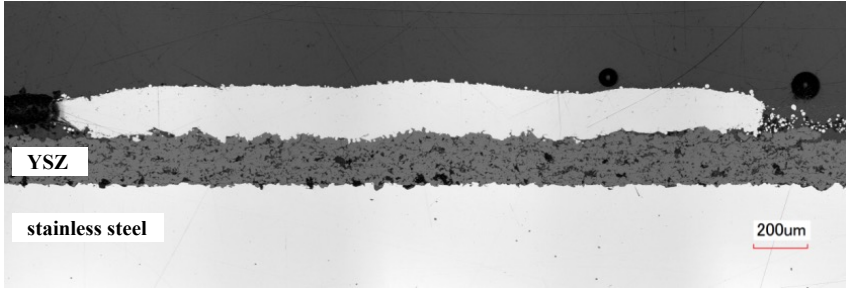


Figure 4.15 Cross section of the cladmed chromel track with optimized parameters under a laser microscope. $P=15$ W, $V=1000$ mm/ min, $D_b=156$ μ m, $F=22.5$ %, $V_p=V_c=10$ l/ min.

Figure 4.16 shows a cladmed K-type thermocouple with optimized parameters. The dimensions of two thermolegs were measured and results are shown in **Table 4.5**. For the chromel thermoleg, the dimension was about 211 ± 3 μ m in height and 191 ± 5 μ m in width. The dimension of the alumel thermoleg was about 96 ± 1 μ m in height and 338 ± 20 μ m in width.

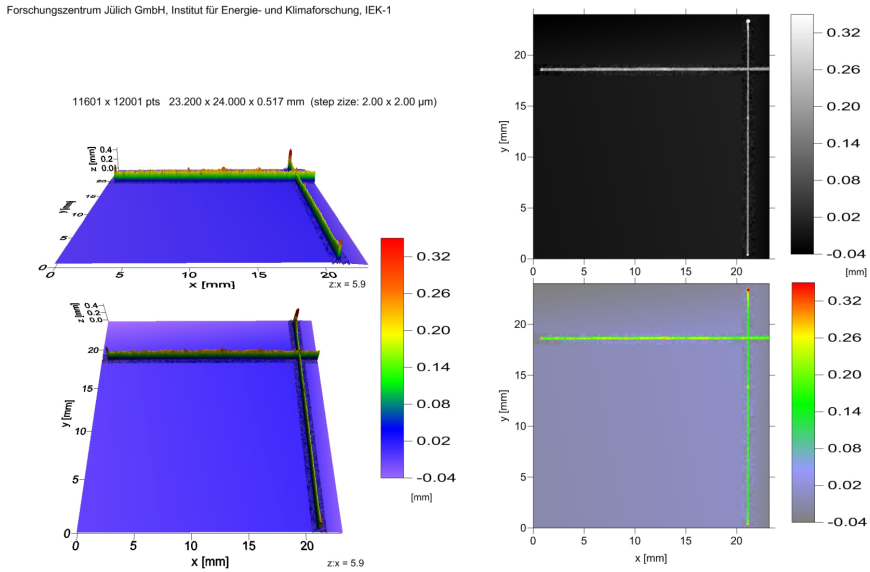


Figure 4.16 Cyberscan micrograph of cladmed K-type thermocouple.

Table 4.5 Dimension of cladded thermolegs with optimized parameters.

track	height (μm)	width (μm)
alumel	96 ± 1	338 ± 20
chromel	211 ± 3	191 ± 5

4.4.4 Thermosensitivity Characterization of the Cladded TC

For the purpose of evaluation of the cladded thermocouple, the thermal and electrical response of the cladded thermocouple was measured over temperatures ranging from ambient up to 500 °C. **Figure 4.17** shows the set-up for determination of the Seebeck coefficient. As shown, each cladded thermoleg was bonded with its corresponding compensation wire. One piece of glass was applied to press both lead wires onto the thermolegs and fixed by a metallic clip. The other sides of compensation wires were connected to the data acquisition system. For comparison, a commercial K-type thermocouple was also mounted on top of the cladded thermocouple junction area to monitor the true sample temperature during the oven test and also connected to the data acquisition system. The sample was inserted into the furnace and heated at 5 K/ min heating rate with flowing Ar protective gas and the voltage and temperatures across the junction were recorded.

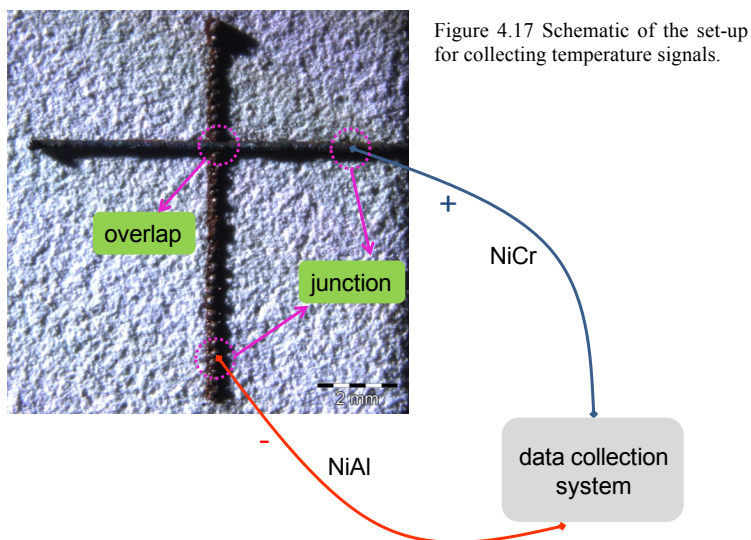


Figure 4.17 Schematic of the set-up for collecting temperature signals.

The thermocouple voltage versus temperature data is shown in **Figure 4.18**. The blue curve and the black curve correspond to the temperature signal of the reference TC and cladded TC, respectively. The lack of data above 480 °C is due to the bad connection between cladded thermolegs and lead wires, at the elevated temperature where the metallic clip failed and the signals could not be recorded any more. Results indicated that the cladded thermocouple had a nearly linear relationship between thermoelectric output voltage and temperature at the experimental temperature range. Its Seebeck coefficient is estimated as 40.9 $\mu\text{V}/\text{K}$ with a regression factor of 0.9996 by a linear fit. A commercial K-type thermocouple typically has a sensitivity of 41.1 $\mu\text{V}/\text{K}$ [98]. So the measured values by the cladded thermocouple were quite reliable and it implied that the cladded thermocouple worked very well as a thermocouple. The difference of the intercept values between the theoretical data of the commercial thermocouple and that of the cladded thermocouple is due to delayed temperature equilibrium during the heating period due to a naturally limited heat transfer/ conduction because the heat element of the furnace was indirect contact to the specimen.

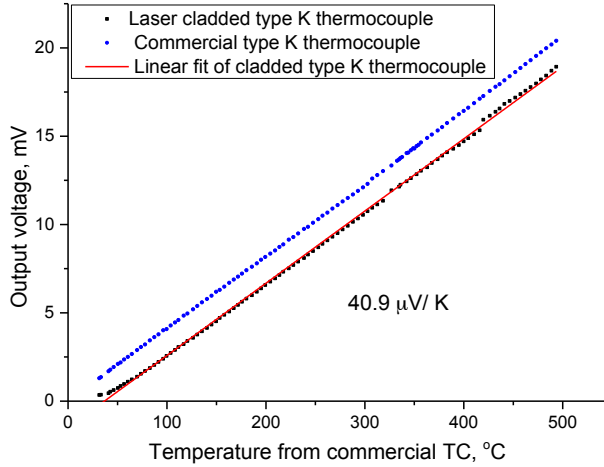


Figure 4.18 K-type thermocouple response from ambient to 500 °C.

4.4.5 Characterization of the Cladded TC Sensor

The electrical resistance of both tracks was examined by a self-assembled DC Four Probe Tester. A value of about $0.03 \pm 0.0004 \Omega$ was measured when the track length was about $2.3 \pm 0.05 \text{ mm}$ for the alumei track and $0.08 \pm 0.004 \Omega$ when the track length was about $3.6 \pm 0.03 \text{ mm}$ for the chromel track. The cross-sectional area was estimated from the profile of a Cyberscan topographer to be about 0.0506 mm^2 for alumei and 0.0377 mm^2 for chromel. Thus, the resistivity for both thermolegs could be calculated and are given in **Table 4.6**. It can be seen that the calculated values are larger than the reported values [90]. In particular for the alumei track, the resistivity is two times bigger than its nominal value. This may be due to the easy oxidation of aluminum which can be found especially at the grain boundaries of alumei. The alumina scale formed during the process is non-conductive and can block the electrical current, so the electrical resistivity is higher than the commercial value. The chromium oxide scale in the chromel tracks is conductive and probably this is why there is no big difference to the reported value.

Table 4.6 Experimental and nominal resistivity of the thermocouple materials.

	resistivity ($\mu\Omega\cdot m$)	
	alumel	chromel
experiment	0.638	0.776
reported [94]	0.29-0.33	0.706

4.4.6 Embedding of Cladded Type-K TC

Before embedding of thermocouples, the embedding of individual tracks has been tried. In order to evaluate the statistical scatter of the results, several tracks under the same parameters were prepared onto the surface of YSZ-based substrate and embedded into YSZ coatings with standard spraying parameters. Contact areas of the tracks were kept accessible by applying a metallic mask (**Figure 4.19a**) in front of the substrate during spraying. **Figure 4.19b-c** shows embedded alumel and chromel tracks, the thickness of top YSZ layer is about 200 μm . **Table 4.7** presents the detailed cladding parameters for both powders. The results represent that 80% of the alumel tracks and 100% of the chromel tracks kept their electrical conductivity after embedding with a second ceramic layer. This means it is possible to embed these cladded thermolegs under the above parameters within functional TBCs.

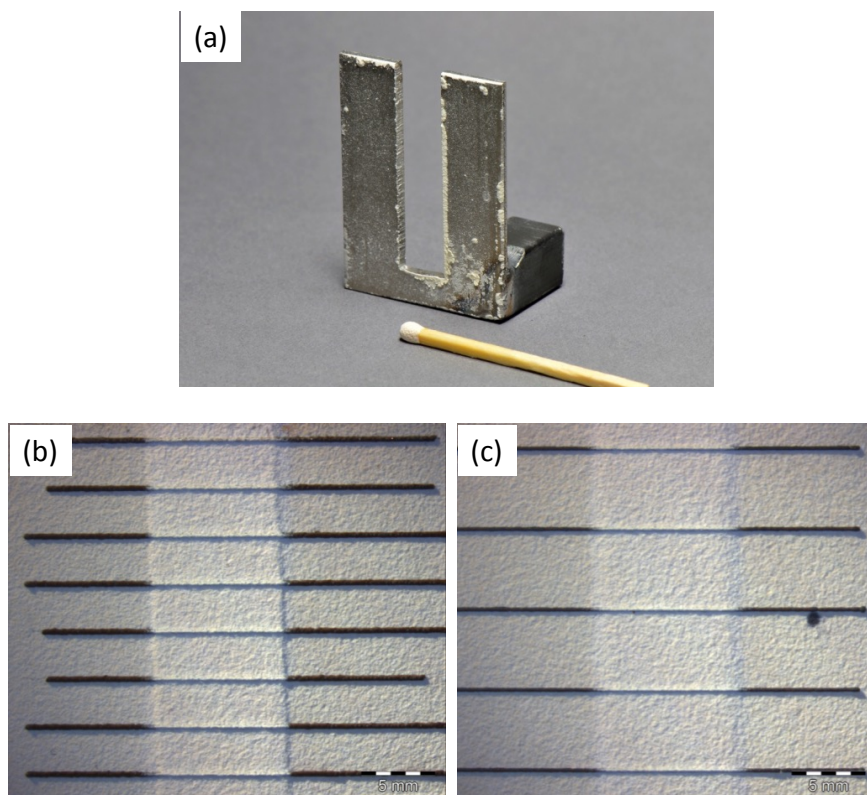


Figure 4.19 The mask used during spraying (a); negative (b) and positive (c) conductor of type K thermocouple with YSZ overcoated.

Table 4.7 Laser cladding parameters for the type K thermocouple deposition.

	P (W)	V (mm/min)	D_b (μ m)	F (%)	V_p (l/ min)	V_c (l/ min)
alumel	15	1000	156	30.0	10	10
chromel	15	1000	156	22.5	10	10

Laser clad K-type thermocouples consisting of Ni₂Al₂Mn₁Si and Ni₁₀Cr were fabricated in the shape of a cross by cladding conductor tracks of alumel and chromel on top of a 30 mm \times 40 mm \times 3.5 mm aluminum substrate that had been previously coated with 200 μ m of APS sprayed

TBC (8YSZ). **Figure 4.20** gives a top view of a bared laser clad thermocouple (left) as well as a thermocouple that has been overcoated with YSZ coatings (right) of 50 μm thickness to demonstrate the ability to embed such sensors underneath functional coatings. The topographies of the coatings were analyzed under the Cyberscan topographer. It is worth mentioning that the scanning area was only the area where tracks were deposited. The scales on the right side reveal the height information of the layers. The dimensions were measured which were $184 \pm 5 \mu\text{m}$ in height and $305 \pm 2 \mu\text{m}$ in width for alumel and $211 \pm 3 \mu\text{m}$ in height and $191 \pm 5 \mu\text{m}$ in width for chromel, respectively. The average roughness was also measured for the cladded alumel which was $10 \pm 2 \mu\text{m}$ and for the chromel was $9 \pm 2 \mu\text{m}$.

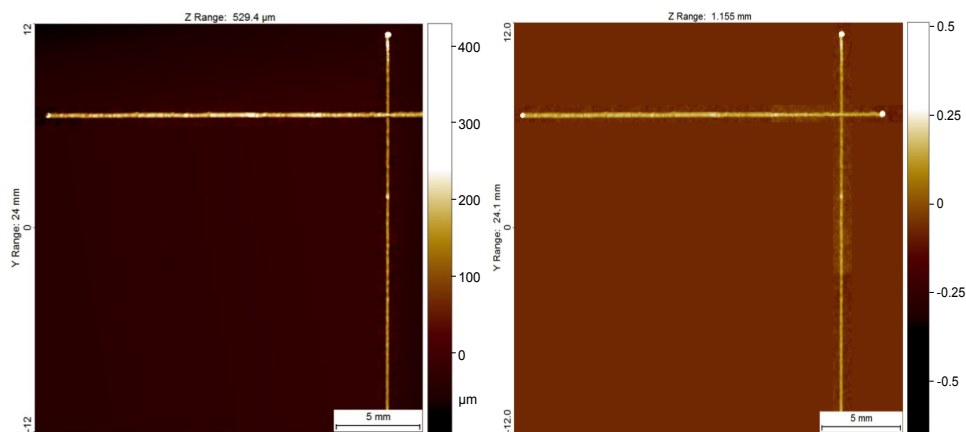


Figure 4.20 Cyberscan micrograph of the cladded K-type thermocouple before (left) and after embedding (right).

Hereafter, the cladded thermocouple was embedded with a YSZ layer of increasing thickness as shown in **Figure 4.21a-c** to investigate whether this thermocouple would lose its electrical conductivity or not. A steel sheet (**Figure 4.21d**) was applied as a mask when spraying the second layer leaving two bared tips for the junction. The cladded thermocouple kept its conductive property after spraying $\sim 200 \mu\text{m}$ thick YSZ coatings.

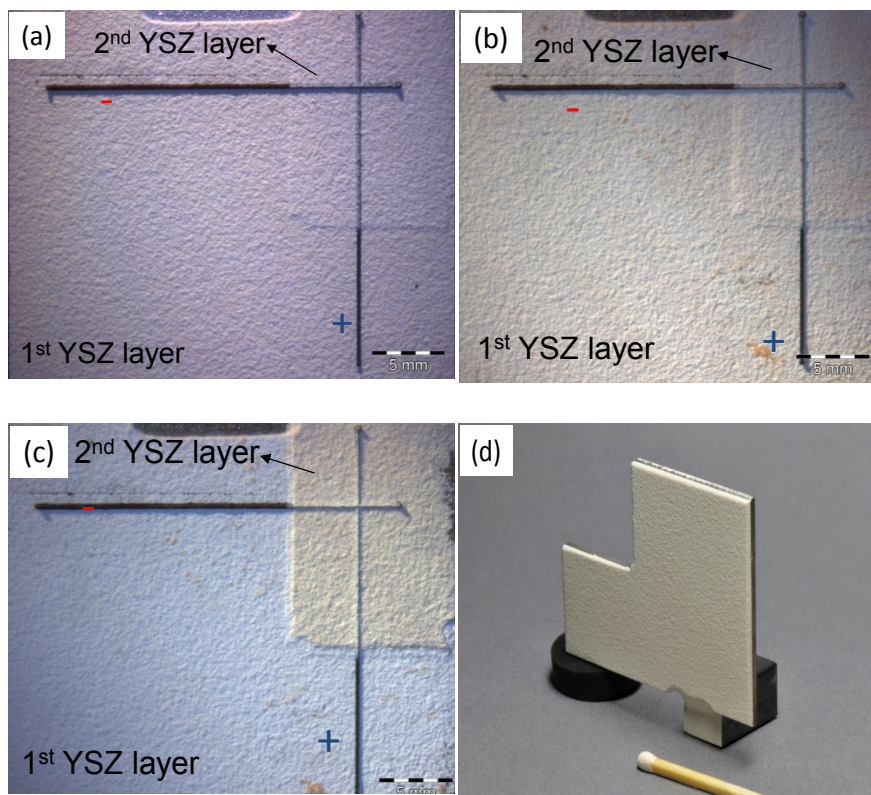
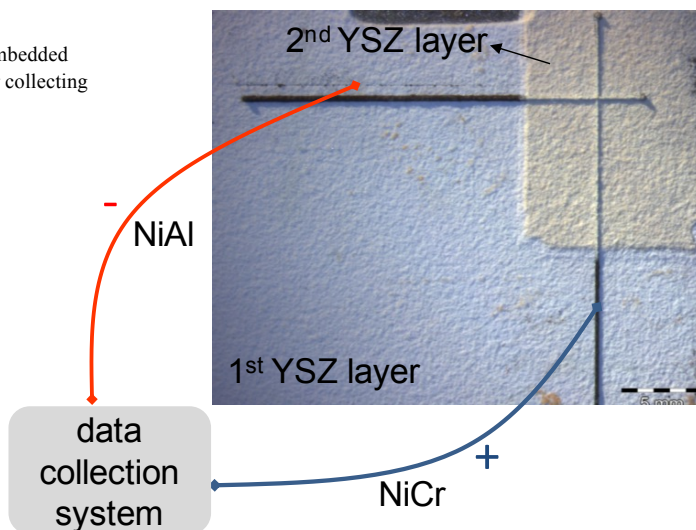


Figure 4.21 The embedded type K thermocouple by YSZ coatings with different thickness: (a) $\sim 50 \mu\text{m}$; (b) $\sim 100 \mu\text{m}$; (c) $\sim 200 \mu\text{m}$. (d) mask.

For the evaluation of the cladded thermocouple before and after embedding with a second ceramic layer, the thermal and electrical response was measured over temperature ranging from ambient up to 450°C , and the results were compared with an industrial standard K-type thermocouple. **Figure 4.22** shows a photo and a set-up for the measurement. The sample was put into the furnace with 5 K/min heating rate under argon protective gas atmosphere that could be able to reduce the oxidation of the produced thermocouple. The voltage and temperatures across the junction were recorded.

Figure 4.22 A photo of one embedded thermocouple and a set-up for collecting temperature signals.



The thermocouple voltage versus temperature data before and after embedding was analyzed as shown in **Figure 4.23**. The Seebeck coefficient of cladded thermocouple before embedding is estimated as $41.2 \mu\text{V}/\text{K}$ with a regression factor of 0.9999 by a linear fit. Similarly, the Seebeck coefficient of this thermocouple after embedding is about $40.9 \mu\text{V}/\text{K}$ within the measurement error with a regression factor of 0.99 by a linear fit. There is a delayed response with the embedded thermocouple at the beginning in **Figure 4.23b** which is caused by the much lower thermal conductivity of the YSZ layer. In both cases, the produced thermocouple yielded a response comparable to the commercial type-K thermocouple and similar with the results reported in [76]. That is to say, the fabricated thermocouple possesses high reproducibility during operation before and after embedding.

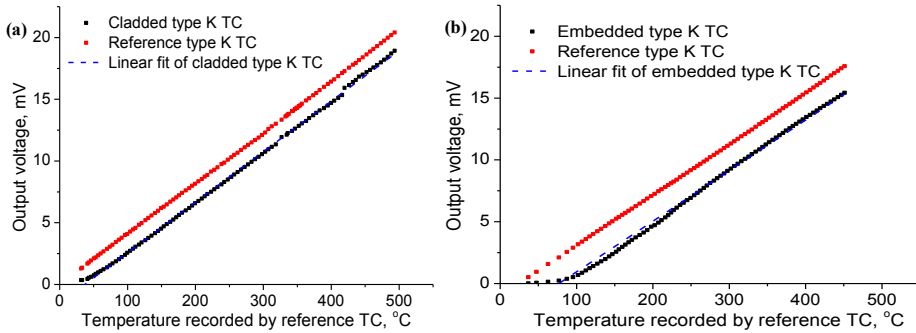


Figure 4.23 K-type thermocouple response from ambient to 450 °C before (a) and after embedding (b).

4.4.7 Deposition of TCs in Small Dimensions

4.4.7.1 Optimization

Since the dimension of tracks is highly related to the spot size on the substrate, thinner tracks were manufactured by reducing the beam diameter on the substrate. The laser power, spot size, carrier and protective gas were kept constant were 15 W, 92 μm , 10 l/ min and 10 l/ min, respectively. The scanning speed and powder feeding rate were optimized to achieve homogeneous clads while preserving a low heat impact to the substrate (**Table 4.8**). For chromel powder, when the travelling speed and powder feeding rate were 2000 mm/ min and 25.0 %, both ceramic substrate and metallic particles melted (**Figure 4.24a**). Convection emerged before molten that formed the big droplet within the ceramic substrate which was not desired. Therefore, powder feeding rate was increased to 30.0 % (**Figure 4.24b**). Under this condition, the substrate was not affected but the dimensions especially the height was not effectively reduced, so the travelling speed and the powder feeding rate was further increased to 3000 mm/ min and 32.0 % (**Figure 4.24d**) finally. The reason why increasing the scanning speed is beneficial to reduce the track height is that the amount of particles delivered per unit length of laser track is reduced. For the almel powder, when the powder feeding rate was higher than 35.0 %, the track detached ($F=50.0$ %) or had poor bonding ($F=35.0$ %) to substrate. So the powder feeding rate was reduced to 32.0 % (**Figure 4.24e**). The dimensions displayed in **Table 4.9** for almel were $61 \pm$

5 μm in height and $175 \pm 5 \mu\text{m}$ in width and for chromel $96 \pm 5 \mu\text{m}$ in height and $150 \pm 5 \mu\text{m}$ in width, respectively.

Table 4.8 Laser cladding parameters for both powders.

powder	track	V (mm/min)	E (J/ mm ²)	F (%)
chromel	(1)	2000	4.9	25.0
	(2)	2000		30.0
	(3)	3000	3.3	30.0
	(4)	3000		32.0
alumel	(5)	4000	2.4	50.0
	(6)	4000		35.0
	(7)	4000		32.0

* Laser power: 15 W; spot size: 92 μm ; protective gas and carrier gas rate: 10 l/ min.

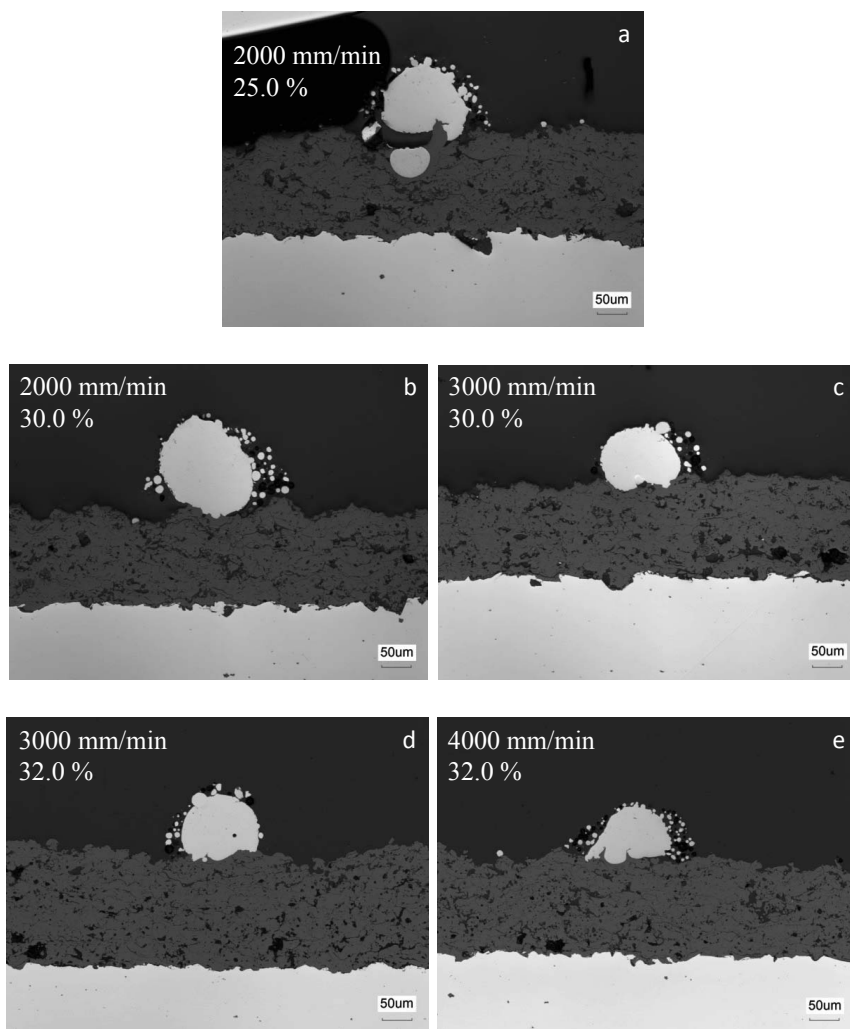


Figure 4.24 Cross-sectional micrographs for both powders under different parameters. $P=15$ W, $D_b=92$ µm, $V_p=V_c=10$ l/ min. (a-d) chromel powder, (e) alumel powder.

Table 4.9 Dimension of cladded thermolegs with optimized parameters.

track	height (μm)	width (μm)
alumel	61 ± 5	175 ± 5
chromel	96 ± 5	150 ± 5

Figure 4.25 shows the influence of the powder feeding rate and the travelling speed to the height of the cladded tracks. The track height was increased from about 115 μm to 170 μm by increasing the powder feeding rate from 25.0 % to 30.0 % and decreased by increasing the travelling speed from 2000 mm/ min to 3000 mm/ min. As mentioned before, the input powder mass per unit length was increased by increasing the powder feeding rate. More particles could be melted if the laser input energy is sufficient. And the input powder mass per unit length was decreased by increasing the travelling speed.

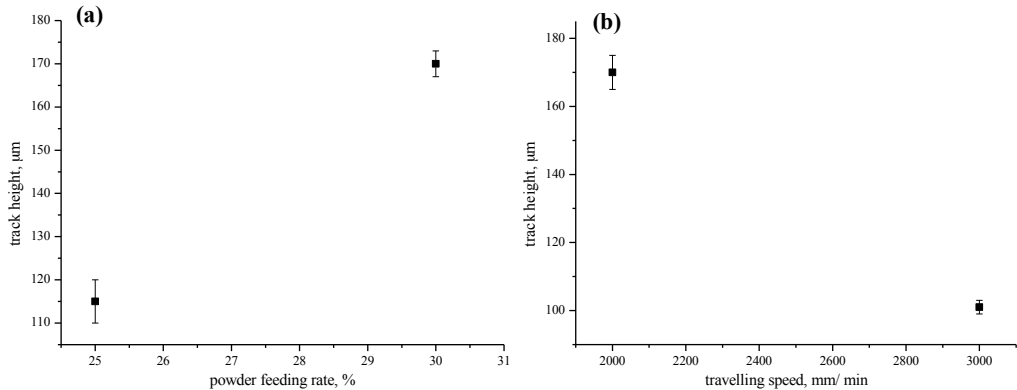


Figure 4.25 Influence of the powder feeding rate (a) and the travelling speed (b) on the height of the chromel tracks by fixing the spot size. $P=15\text{ W}$, $D_b=92\text{ }\mu\text{m}$, $V_p=V_c=10\text{ l/min}$.

4.4.7.2 Depositing and Embedding K-type TC

K-type thermocouple were cladded in a crosswise geometry with the above optimized parameters (alumel: $P=15\text{ W}$, $V=4000\text{ mm/min}$, $D_b=92\text{ }\mu\text{m}$, $F=32.0\text{ }\%$, $V_p=V_c=10\text{ l/min}$; chromel: $P=15\text{ W}$, $V=3000\text{ mm/min}$, $D_b=92\text{ }\mu\text{m}$, $F=32.0\text{ }\%$, $V_p=V_c=10\text{ l/min}$) as shown in **Figure 4.26a**.

Afterwards, it was embedded by a second ceramic layer with a thickness of about 200 μm (**Figure 4.26b**). A steel sheet was used as a mask when spraying the second layer leaving two bared tips for the junction. However, after spraying the second layer, the cladded thermocouple did not work due to a non-sufficient electrical conductivity. In order to find out the reason for this, cross sections of embedded specimen were prepared. **Figure 4.27a** shows deposited alumel along the cladding direction and **Figure 4.27b** shows deposited chromel perpendicular to the cladding direction. Holes indicating removed alumel particles happened during metallographic preparation can be observed at the interface between cladded alumel and ceramic substrate after embedding the second layer. It implied that the mechanical bonding strength between were very poor when compared to the metallurgical adhesion. From this point of view, more stable tracks need to be produced and better balance between good bonding and little HAZ should be figured out.

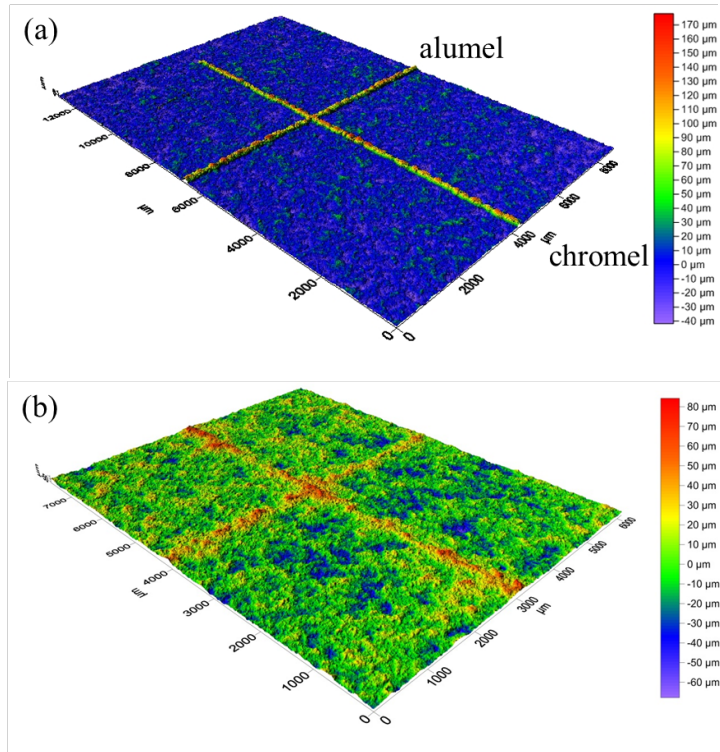


Figure 4.26 Cladded thermocouple (a) before embedding (b) after embedding.

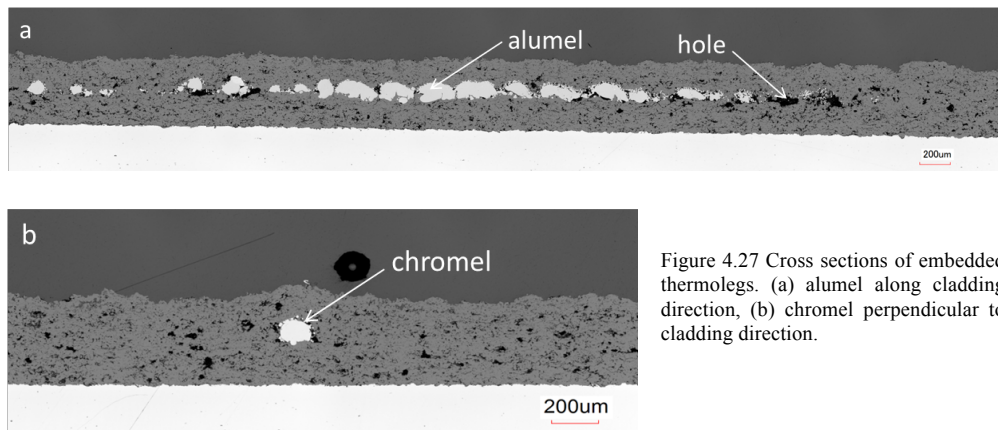


Figure 4.27 Cross sections of embedded thermocouples. (a) alumel along cladding direction, (b) chromel perpendicular to cladding direction.

In conclusion, increasing the powder feeding rate is an effective method to avoid melting of ceramic substrate because of the attenuation of laser beam energy by particle clouds above the substrate. Laser cladding parameters were optimized and a clad thermocouple with desired properties like no impact to the substrate, relatively small dimensions, and good electrical and thermal response was possible to be deposited. A thinner thermocouple with optimized parameters was also produced, however, the first attempt to embed it failed. Poor mechanical bonding and alumel clad quality might be the main reason leading to this problem. Therefore, a balance of mechanical bonding and minimal disturbance to the substrate needs to be adjusted according to the dimensions of the tracks and the substrate roughness.

4.5 Deposition of K-type TC with a Pulsed Laser

4.5.1 Optimization of Alumel Tracks

As a result of the bad wetting behavior of NiAl (alumel) powder on the YSZ ceramic substrate, inhomogeneous tracks with large droplets were formed with the continuous wave laser cladding process. As a result, the following embedding with a second ceramic layer was more difficult and complicated. The dimension of the HAZ was effectively diminished by increasing the powder feeding rate to increase the reflection of the laser beam by the metallic powder and the shadowing effect. Contrary to the continuous wave laser cladding, the pulsed laser cladding offers a number of advantages [99]: lower heat build-up in the workpiece and therefore lower HAZ and dilution. Meanwhile, the laser power-off period between two pulses allows the melt pool to cool down, therefore, the melts duration is shorter in pulsed laser cladding than in continuous wave laser cladding. This might be helpful to avoid the formation of large droplets. Taking into consideration these issues, pulsed laser was applied to deposit tracks.

In order to optimize the process parameters, a number of tracks were deposited at different parameters. The detailed cladding parameters are given in **Table 4.10**. The experiments for alumel powder were performed with fixed spot size on the ceramic surface, powder feeding rate, pulse duration, frequency, protective and carrier gas rate which were 92 μm , 30.0 %, 0.5 ms, 250 Hz, 10 l/ min and 10 l/ min, respectively. As mentioned before, the dimension of the HAZ could

be reduced by increasing the powder feeding rate or by reduction of the energy input per unit area at the substrate surface. The continuous wave laser power could not be further reduced lower than 12 W because of the limitation of the laser facility. However, the laser power could be diminished with a large extent by using a pulsed laser mode. Therefore, the average laser power was decreased to 2.5 W by applying 20 W peak power of the pulsed laser. The cladded tracks were first examined visually. For the purpose of better comparison with the continuous wave laser cladding, a similar energy per unit area of 2.5 J/mm^2 was selected. In this case, the laser power and travelling speed for pulse laser and continuous wave laser were 100 W and 3000 mm/ min (**Table 4.10a**), 15 W and 4000 mm/ min (**Table 4.10g**), respectively. In **Figure 4.28a**, it can be seen from the surface that very few particles were attached to the substrate after pulsed laser cladding and the track area became dark. The same energy input per unit area of two tracks with different parameters (**Table 4.10b and e**) was also picked up to see whether there was any difference of the dimension of the HAZ. The variables were the laser power and scanning velocity and the other parameters were kept constant. More particles stuck to the surface (**Figure 4.28b**) than the track displayed in **Figure 4.28a** because the scanning velocity was reduced, the number of particles delivered per unit length were increased and therefore more particles could be melted by the laser beam source for the supplied energy being sufficient. Even more molten particles were achieved and sticking to the substrate by diminishing the travelling speed from 1000 mm/ min (**Figure 4.28c**) to 200 mm/ min (**Figure 4.28e**). Furthermore, tracks became more and more homogeneous by reducing the scanning speed. The parameters for alumel powder were further improved to 20 W laser power, 100 mm/ min scanning velocity, 30.0 % powder feeding rate, 0.5 ms pulse duration, 250 Hz pulse frequency, 10 l/ min carrier and protective gas rate (**Figure 4.28e**). The decrease of the pulsed duration to 0.4 ms was also attempted and **Figure 4.28f** gives the top view of this alumel track. No big droplets occurred along the deposited tracks (**Figure 4.28e-f**) and the wetting behavior of the NiAl alloy against the YSZ coating was no longer a problem by applying a pulsed laser which could not be solved with a CW laser.

Table 4.10 Laser cladding parameters for the alumeI powder.

	P (W)	V (mm/ min)	t (ms)	f (Hz)	E (J/ mm²)
a	100	3000	0.5	250	2.45
b	100	1000	0.5	250	8.15
c	20	1000	0.5	250	1.63
d	20	500	0.5	250	3.26
e	20	200	0.5	250	8.15
f	20	100	0.4	250	13.04
g	15	4000	-	-	2.72

* Spot size: 92 μm ; feeding rate: 30.0 %; protective gas and carrier gas rate: 10 l/ min.



Figure 4.28 Stereo micrographs of cladded tracks for alumel powder. $D_b=92\ \mu\text{m}$, $F=30.0\ \%$, $f=250\ \text{Hz}$, $V_p=V_c=10\ \text{l/min}$. (a) $P=100\ \text{W}$, $V=3000\ \text{mm/min}$, $t=0.5\ \text{ms}$; (b) $P=100\ \text{W}$, $V=1000\ \text{mm/min}$, $t=0.5\ \text{ms}$; (c) $P=20\ \text{W}$, $V=1000\ \text{mm/min}$, $t=0.5\ \text{ms}$; (d) $P=20\ \text{W}$, $V=500\ \text{mm/min}$, $t=0.5\ \text{ms}$; (e) $P=20\ \text{W}$, $V=200\ \text{mm/min}$, $t=0.5\ \text{ms}$; (f) $P=20\ \text{W}$, $V=100\ \text{mm/min}$, $t=0.4\ \text{ms}$.

Figure 4.29 shows the cross sections of some clad tracks perpendicular to the cladding directions. Even though similar energy per unit area was applied for both pulsed and CW laser cladding, the dimensions of the HAZ were completely different (**Figure 4.29a and e**). The HAZ for pulsed laser cladding was much more severe and affected the entire YSZ coatings underneath the clad (**Figure 4.29a**). However, little effect to the YSZ coating was observed in **Figure 4.29e**. Therefore, it can be concluded that under similar energy per unit area, a higher peak power leads to a larger HAZ. The dimension of the HAZ in **Figure 4.29b** was more serious than that in **Figure 4.29a** and more particles were penetrated into the ceramic coating which maybe induced by the higher energy input per unit length. Likewise, with the same energy per unit area but different peak power (**Figure 4.29b-c**), the HAZ was also quite different. When the laser peak power was decreased to 20 W, there was little influence to the YSZ substrate due to the laser cladding as can be seen in **Figure 4.29c**. With optimized parameters, there was no obvious impact of the clad to the substrate as can be seen from the cross section in **Figure 4.29d**.

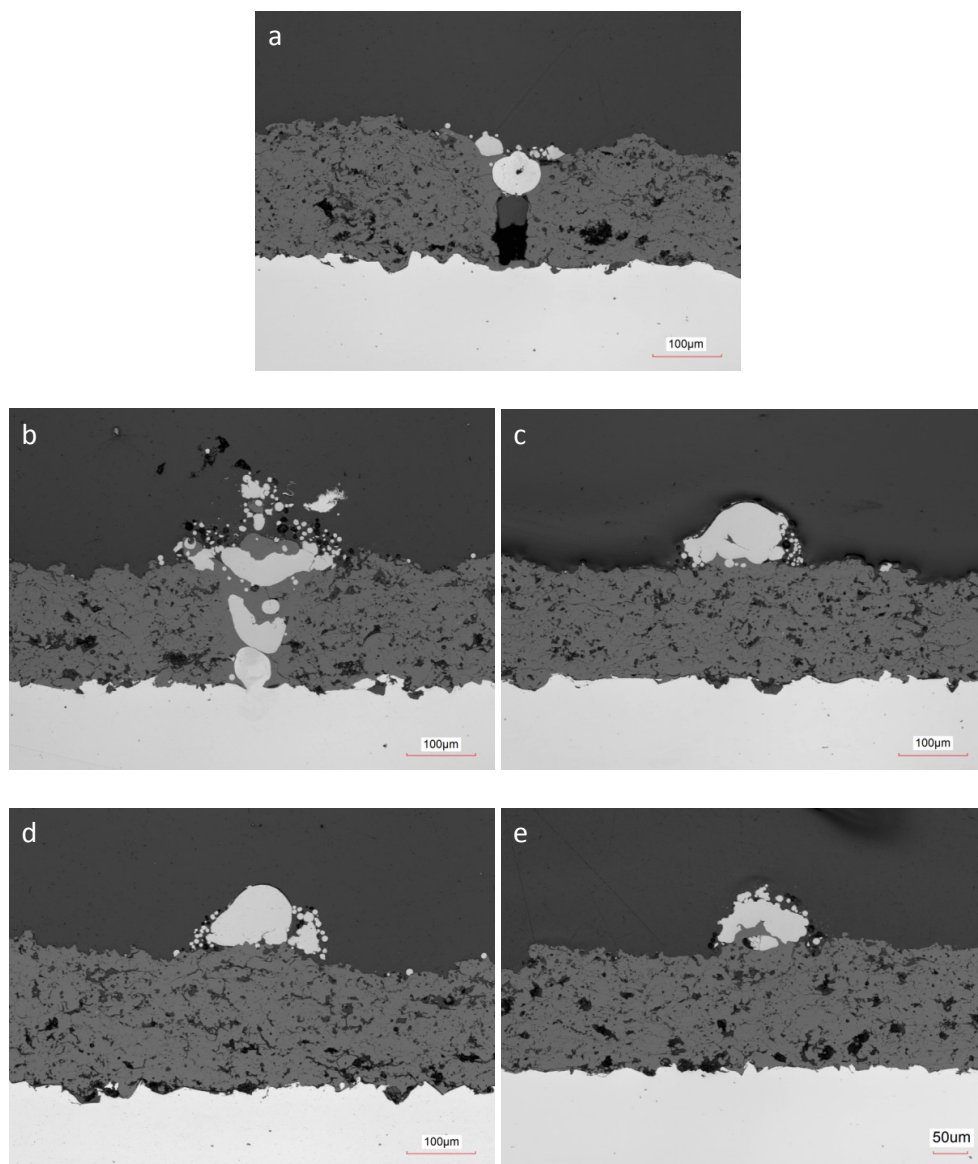


Figure 4.29 Cross-sectional microstructure of the cladmed alumel tracks with different parameters. $D_b=92 \mu\text{m}$, $F=30.0 \%$, $V_p=V_c=10 \text{ l/min}$. Pulse mode: (a) $P=100 \text{ W}$, $V=3000 \text{ mm/min}$, $t=0.5 \text{ ms}$, $f=250 \text{ Hz}$, (b) $P=100 \text{ W}$, $V=1000 \text{ mm/min}$, $t=0.5 \text{ ms}$, $f=250 \text{ Hz}$, (c) $P=20 \text{ W}$, $V=200 \text{ mm/min}$, $t=0.5 \text{ ms}$, $f=250 \text{ Hz}$, (d) $P=20 \text{ W}$, $V=100 \text{ mm/min}$, $t=0.4 \text{ ms}$, $f=250 \text{ Hz}$, cw mode: (e) $P=15 \text{ W}$, $V=4000 \text{ mm/min}$.

According to the above results, the following conclusions are obtained: once there are too less powder particles sticking to the substrate, two cases maybe involved. One is that the remaining energy after attenuation by in-flight particles is insufficient to melt a certain amount of powder and the ceramic surface keeps nearly intact. The other is that the remaining energy after attenuation is so high that the ceramic layer and injected particles are both melted and most powder particles are buried by or penetrated into the ceramic substrate (**Figure 4.28a and Figure 4.29a**). The ceramic surface becomes dark which is probably induced by the loss of oxygen atoms during laser cladding operation and/ or the color from the buried cladding layer because of the transparency of the ceramic coatings.

The above optimized alumel track ($P=20$ W, $V=100$ mm/ min, $D_b=92$ μ m, $F=30.0$ %, $V_p=V_c=10$ l/ min, $t=0.4$ ms, $f=250$ Hz) was further analyzed by the Cyberscan topographer as given in **Figure 4.30**. Obviously, this deposited clad was very smooth as desired. The dimension for this clad layer was about 95 ± 20 μ m in height and 119 ± 13 μ m in width.

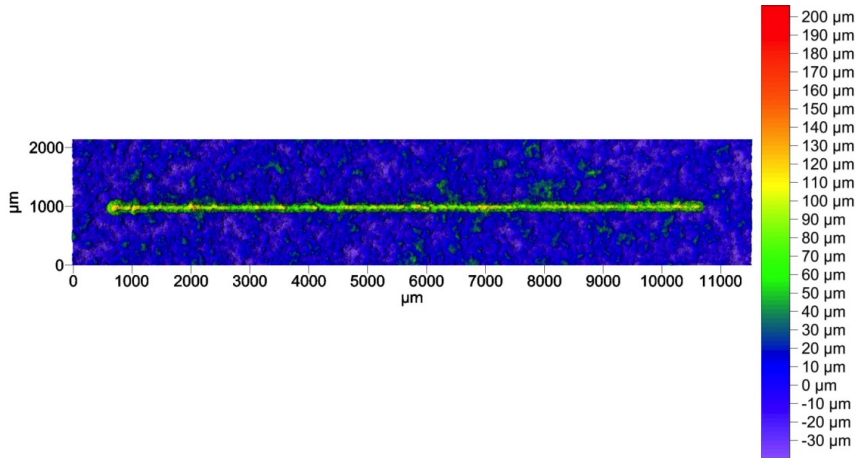


Figure 4.30 Cyberscan micrograph of the clad layer. $P=20$ W, $V=100$ mm/ min, $D_b=92$ μ m, $F=30.0$ %, $V_p=V_c=10$ l/ min, $t=0.4$ ms, $f=250$ Hz.

4.5.2 Optimization of Chromel Tracks

Also for the chromel powder, which composes the type-K thermocouple together with the alumel thermoleg, similar parameters were first attempted (**Table 4.11**) as optimized for the alumel. The laser power, spot size, pulse duration, pulse frequency, carrier and protective gas rate were kept constant, and the powder feeding rate of 15.0 % and 17.5 % were applied with 100 mm/ min and 150 mm/ min travelling speed, respectively. The reason for using 150 mm/ min is to further reduce the width of the tracks [45]. When the feeding rate was more than 20.0 %, detached tracks were obtained (**Figure 4.31a**) or even no tracks formed on the substrate as a result of the insufficient energy of the laser beam after attenuation by the particle cloud. Macroscopic morphologies were displayed in **Figure 4.31b-d**. It turned out that all tracks were bonded to the substrate, but the electrical continuity was unstable with 150 mm/ min scanning velocity. This might be attributed to the decrease of delivered particle numbers, thereby, the melted particles became less and were insufficient to ensure its conductivity.

Table 4.11 Laser cladding parameters for the chromel powder.

	V (mm/ min)	F (%)	t (ms)	E ₀ (J)	P ₀ (W)
(1)	100	26.0	0.4	0.008	2
(2)	100	20.0	0.4	0.008	2
(3)	100	15.0	0.4	0.008	2
(4)	100	17.5	0.4	0.008	2
(5)	150	15.0	0.4	0.008	2
(6)	150	17.5	0.4	0.008	2

* Spot size: 92 μm ; power: 20 W; laser pulse frequency: 250 Hz; protective gas and carrier gas rate: 10 l/ min.

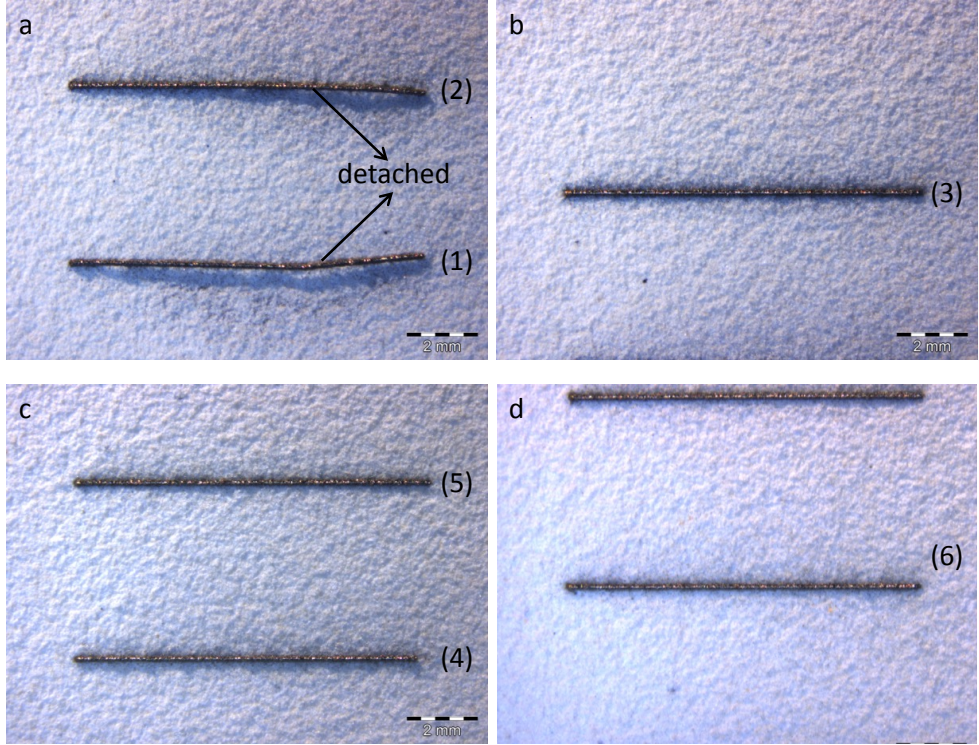


Figure 4.31 Stereo micrographs of cladded tracks for the chromel powder. $P=20$ W, $D_b=92$ μm , $f=250$ Hz, $t=0.4$ ms, $V_p=V_c=10$ l/ min. (1) $V=100$ mm/ min, $F=26.0$ %; (2) $V=100$ mm/ min, $F=20.0$ %; (3) $V=100$ mm/ min, $F=15.0$ %; (4) $V=100$ mm/ min, $F=17.5$ %; (5) $V=150$ mm/ min, $F=15.0$ %; (6) $V=150$ mm/ min, $F=17.5$ %.

The cross sections of deposited tracks perpendicular to the cladding directions for chromel powder were given in **Figure 4.32** from track 3 to track 6 (**Figure 4.31**). It can be seen that the YSZ substrate was not seriously influenced by the laser cladding process. In addition, the morphologies in **Figure 4.32a and c** were with more regular structures with 15.0 % powder feeding rate. Instead, the morphologies of cladded tracks (**Figure 4.32b and d**) were irregular if the remaining energy was insufficient to totally melt the injected particles with 17.5 % powder feeding rate. Thus, the chromel track with the parameters of $P=20$ W, $D_b=92$ μm , $V=100$ mm/ min, $F=15.0$ %, $t=0.4$ ms, $f=250$ Hz, $V_p=V_c=10$ l/ min was taken as the optimized clad. Considering to obtain smaller dimension chromel thermoleg, the laser peak power of 15 W was adopted and the process parameters were eventually optimized to $P=15$ W, $V=80$ mm/ min,

$D_b=92\ \mu\text{m}$, $F=16.0\ \%$, $V_p=V_c=10\ \text{l/min}$, $t=0.5\ \text{ms}$, $f=250\ \text{Hz}$ with a similar optimization procedure.

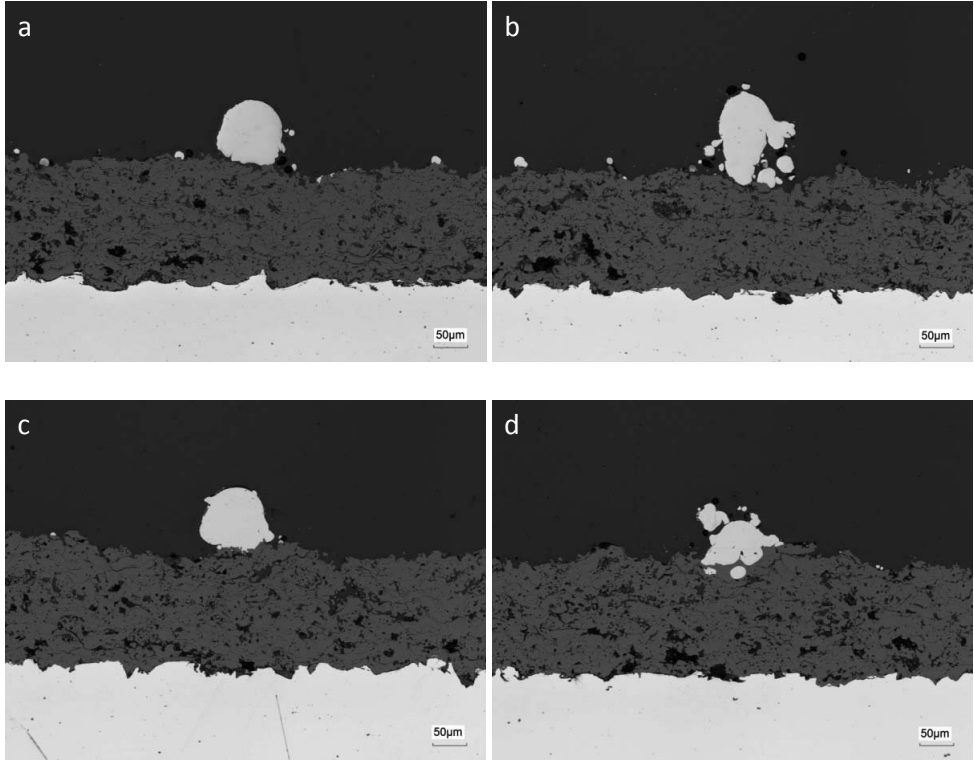


Figure 4.32 Cross-sectional microstructure of the cladded chromel tracks with different parameters. $P=20\ \text{W}$, $D_b=92\ \mu\text{m}$, $t=0.4\ \text{ms}$, $f=250\ \text{Hz}$, $V_p=V_c=10\ \text{l/min}$. (a) $V=100\ \text{mm/min}$, $F=15.0\ \%$; (b) $V=100\ \text{mm/min}$, $F=17.5\ \%$; (c) $V=150\ \text{mm/min}$, $F=15.0\ \%$; (d) $V=150\ \text{mm/min}$, $F=17.5\ \%$.

Figure 4.33 displays the behavior of the clad height as a function of the powder feeding rate and the travelling speed for chromel powder. Similarly, the track height increased with the powder feeding rate and decreased with the travelling speed. The track height was about $90\ \mu\text{m}$ with $15.0\ \%$ powder feeding rate and increased to about $135\ \mu\text{m}$ by applying $17.5\ \%$ powder feeding

rate. When increasing the travelling speed from 100 mm/ min to 150 mm/ min, the track height was decreased from about 92 μm to 88 μm .

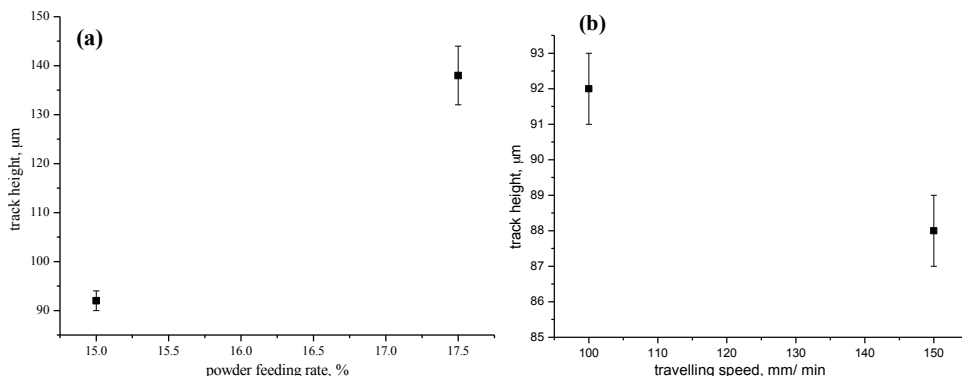


Figure 4.33 Influence of the powder feeding rate (a) and the travelling speed (b) on the height of the clad chromel tracks. $P=20\text{ W}$, $D_b=92\text{ }\mu\text{m}$, $t=0.4\text{ ms}$, $f=250\text{ Hz}$, $V_p=V_c=10\text{ l/ min}$.

4.5.3 Preparation of K-type TCs

The K-type thermocouples were clad in an arrow layout with the above optimized parameters (alumel: $P=20\text{ W}$, $V=100\text{ mm/ min}$, $D_b=92\text{ }\mu\text{m}$, $F=30.0\text{ }\%$, $V_p=V_c=10\text{ l/ min}$, $t=0.4\text{ ms}$, $f=250\text{ Hz}$; chromel: $P=20\text{ W}$, $V=100\text{ mm/ min}$, $D_b=92\text{ }\mu\text{m}$, $F=15.0\text{ }\%$, $V_p=V_c=10\text{ l/ min}$, $t=0.4\text{ ms}$, $f=250\text{ Hz}$) shown in **Figure 4.34a**. For this clad thermocouple, the dimensions for alumel were $82 \pm 3\text{ }\mu\text{m}$ in height and $113 \pm 16\text{ }\mu\text{m}$ in width and $114 \pm 10\text{ }\mu\text{m}$ in height and $81 \pm 18\text{ }\mu\text{m}$ in width for chromel, respectively. The average roughness for the clad alumel was $13 \pm 3\text{ }\mu\text{m}$ and for chromel $13 \pm 3\text{ }\mu\text{m}$. The thermocouple was also deposited with slightly varied parameters (alumel: $P=20\text{ W}$, $V=100\text{ mm/ min}$, $D_b=92\text{ }\mu\text{m}$, $F=30.0\text{ }\%$, $V_p=V_c=10\text{ l/ min}$, $t=0.4\text{ ms}$, $f=250\text{ Hz}$; chromel: $P=15\text{ W}$, $V=80\text{ mm/ min}$, $D_b=92\text{ }\mu\text{m}$, $F=16.0\text{ }\%$, $V_p=V_c=10\text{ l/ min}$, $t=0.5\text{ ms}$, $f=250\text{ Hz}$) and the microstructure is shown in **Figure 4.34b**. Part of the alumel track was missing after cleaning in the ethanol bath and it can be clearly seen that YSZ substrate was not obviously affected by this process. In addition, it implies that the adhesion between alumel track and YSZ substrate was poor. For the chromel thermocouple, the dimension was about $124 \pm 9\text{ }\mu\text{m}$ in height and $90 \pm 3\text{ }\mu\text{m}$

in width. The dimension of alumel thermoleg was about $94 \pm 3 \mu\text{m}$ in height and $125 \pm 4 \mu\text{m}$ in width. The average roughness was about $9 \pm 3 \mu\text{m}$ and $13 \pm 3 \mu\text{m}$ for alumel and chromel. Since the track quality is very sensitive to these above mentioned issues, specimens with flat surface should be carefully processed.

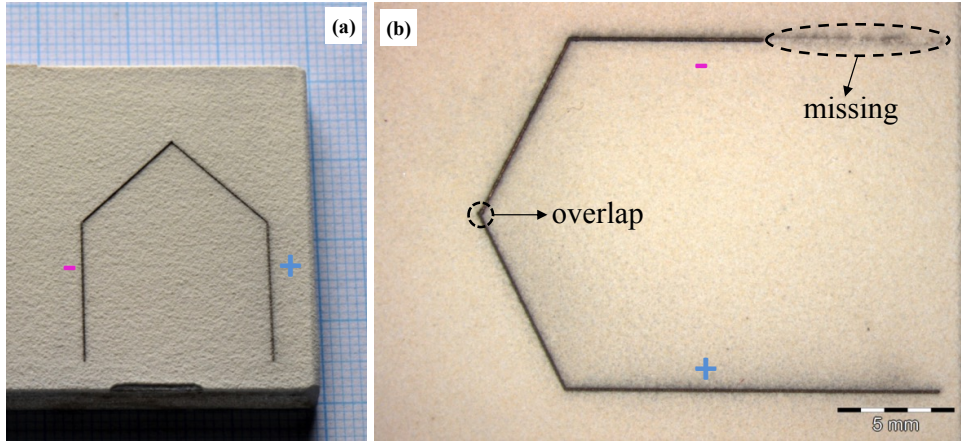


Figure 4.34 Micrographs of cladded TCs with optimized parameters. (a) alumel: $P=20 \text{ W}$, $V=100 \text{ mm/min}$, $D_b=92 \mu\text{m}$, $F=30.0 \%$, $V_p=V_c=10 \text{ l/min}$, $t=0.4 \text{ ms}$, $f=250 \text{ Hz}$; chromel: $P=20 \text{ W}$, $V=100 \text{ mm/min}$, $D_b=92 \mu\text{m}$, $F=15.0 \%$, $V_p=V_c=10 \text{ l/min}$, $t=0.4 \text{ ms}$, $f=250 \text{ Hz}$; (b) alumel: $P=20 \text{ W}$, $V=100 \text{ mm/min}$, $D_b=92 \mu\text{m}$, $F=30.0 \%$, $V_p=V_c=10 \text{ l/min}$, $t=0.4 \text{ ms}$, $f=250 \text{ Hz}$; chromel: $P=15 \text{ W}$, $V=80 \text{ mm/min}$, $D_b=92 \mu\text{m}$, $F=16.0 \%$, $V_p=V_c=10 \text{ l/min}$, $t=0.5 \text{ ms}$, $f=250 \text{ Hz}$.

4.5.4 Embedding of the Cladded TCs

A steel sheet was used as a mask when spraying a second YSZ layer, leaving two bared tips for the junctions. When trying to place the mask, segmental spalling of the TC legs could be observed during preparation (**Figures 4.34b, Figure 4.35**). The second YSZ layer was sprayed only for one pass to easier find out the reasons causing the problem of non-conductivity. Apparently, width and height of clads were reduced at some locations of the tracks which are marked in **Figure 4.35b-c**. The potential reason might be due to ruptures taking place due to the impingement of the ceramic particles on the tracks. Certainly, parameters need to be further optimized with pulsed laser cladding.

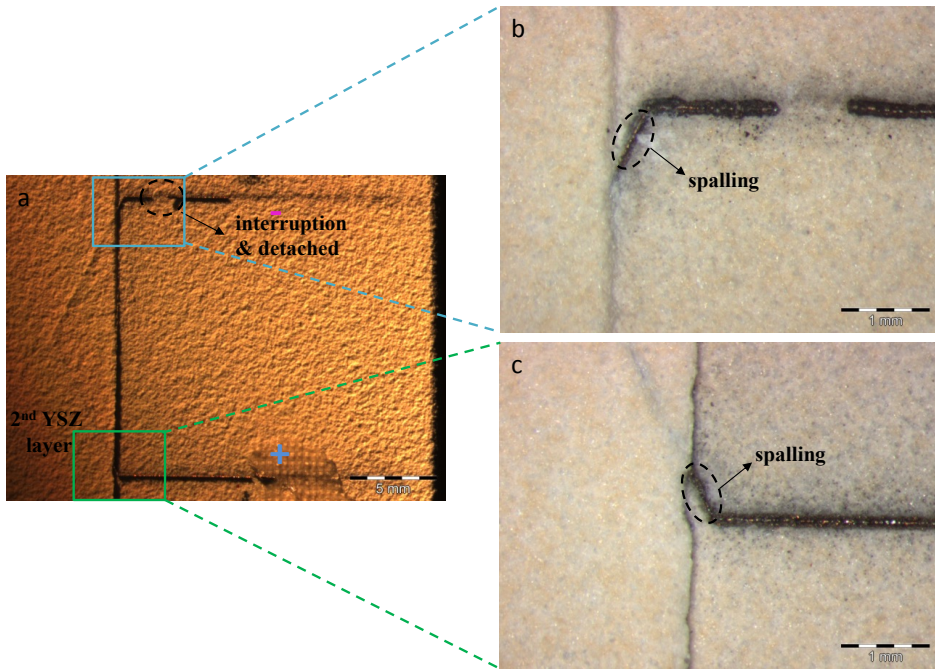


Figure 4.35 Microstructures of embedded thermocouple with the second YSZ layer under the stereo microscope. (a) low magnification, (b) high magnification for the alumel track, (c) high magnification for the chromel track.

To sum up, both the energy input per unit area and pulsed energy played an important role for the dimension of the HAZ, reducing the laser peak power or increasing the powder feeding rate is helpful to diminish the influence of cladding process to the ceramic substrate significantly. K-type thermocouples in the range of 100 μm were possible to be fabricated with the desired properties like no impact to substrate, conductive and low roughness by applying pulsed laser with optimizing the process parameters. Unfortunately, the cladded thermocouple produced with a pulsed laser was failed to work after embedding. There might be two reasons for the degradation. One might be the quality of the cladded thermocouple which was not perfect, so interruptions took place after spraying. A second factor might be the shear force. The measurements of the adhesion strength showed that it plays an important role but not the most significant factor for the successful embedding.

4.6 Shear Force Measurements

From the experience of the previous experiments, it is clear that the bonding strength between cladded tracks and the substrate plays also an important role for the following embedding with the second ceramic layer. Therefore, the shear force measurement was carried out with all the optimized parameters for both kind of clads to evaluate the adhesion strength. The results are shown in **Figure 4.36**. A big scattering is observed for chromel tracks. There is not much difference of the mean shear force per unit area for these three different cladding parameters. For tracks made of alumel powder, there is no big scattering of the shear force except the third deposited clad. From the aforementioned results, it is already known that it is possible to embed the produced thermocouples with parameters of $P=15\text{ W}$, $V=1000\text{ mm/min}$, $D_b=156\text{ }\mu\text{m}$, $F=30.0\%$, $V_p=V_c=10\text{ l/min}$ for alumel powder and $P=15\text{ W}$, $V=1000\text{ mm/min}$, $D_b=156\text{ }\mu\text{m}$, $F=22.5\%$, $V_p=V_c=10\text{ l/min}$ for chromel powder while clads with other parameters were still unable to be which possess similar adhesion strength. In other words, the bonding plays an important role but not the most significant factor for the successful embedding.

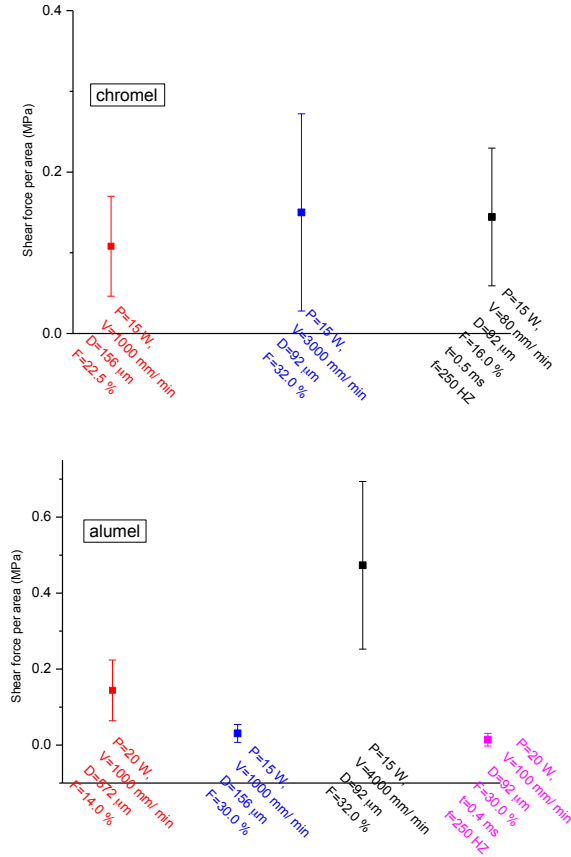


Figure 4.36 Shear force measurement of relatively optimized cladding parameters, the carrier and shielding gas rate are 10 l/ min.

4.7 Summary of Optimized Tracks

Table 4.12 summarizes the optimized parameters for both type-K TC tracks. The cladded tracks can be successfully embedded or not are also described.

Table 4.12 Optimized parameters for both tracks.

	P (W)	V (mm/ min)	D _b (μm)	F (%)	t (ms)	f (Hz)	successful embedding?
chromel	15	1000	156	22.5	-	-	√
	15	3000	92	32	-	-	×
	15	80	92	16	0.5	250	×
alumel	20	1000	572	14	-	-	×
	15	1000	156	30	-	-	√
	15	4000	92	32	-	-	×
	20	100	92	30	0.4	250	×

5. Droplets Formation Mechanism

The laser cladding process depends on a number of variables: laser power, scanning speed, powder feeding rate, duration of particle interaction with the laser beam, relative positions of the laser beam waist, substrate and nozzle outlet, respectively. Droplets were observed from time to time during cladding. This phenomenon is determined by the temperature-dependent rheological properties of the melt (viscosity, surface tension, wettability, etc.) and the amount of melt produced during laser heating [100]. The relation between travelling velocity, power density and powder feeding rate determines whether a deposited layer is smooth and continuous or it is divided into separate segments. So a series of experiments have been made to analyze the influence of the above mentioned parameters on the surface of the stainless steel coated with YSZ layers to better understand the mechanisms controlling this phenomenon. Corresponding parameters are given in **Table 5.1**.

Table 5.1 Laser cladding parameters for different tracks.

	chromel				alumel			
	a	b	c	d	e	f	g	h
P (W)	15	15	22	15	15	15	25	15
V (mm/min)	1000	1500	1500	1000	1000	2500	2500	1000
F (%)	22.5	22.5	22.5	17.5	29	29	29	20

* Spot size: 156 μm ; protective gas and carrier gas rate: 10 l/ min.

It can be clearly seen in **Figure 5.1** that droplets occurred periodically along the clads. Compared to a homogenous clad (**Figure 5.1a**), the droplets that are much larger than its original particle sizes are induced to be formed by reducing the powder feeding rate (**Figure 5.1d**) or increasing the laser power (**Figure 5.1c**) for chromel powder. Similar results were also observed with alumel powder (**Figure 5.1e-h**). Both reduction of powder feeding rate (the remaining energy after attenuation by the particle clouds is higher with reduced powder feeding rate due to less reflection by sparser powder density) and increase of power will lead an increase of the peak temperatures during this process. The higher the temperature is, the smaller the viscosity and

surface tension are [101]. In accordance with this, the melts should be prone for spreading or have better wettability on the substrate, thus, clads with smoother morphology should be acquired. However, the experimental results were contrary to this hypothesis. Therefore, the droplets formation should be related to some other factors.

Table 5.2 shows two combined parameters during laser cladding process: energy input per unit mass of the powder (P/F , J/g) and injected powder per unit length (F/V , g/m). For chromel, it can be clearly seen that droplets have the less tendency to be formed by reducing the energy input per unit mass of the powder (**Figure 5.1a-c**). The injected powder per unit length plays an important role under the same energy input per unit mass of the powder as well. By increasing the injected powder per unit length, droplets have the less tendency to be formed (**Figure 5.1c-d**). In another words, duration of melt is obviously critical for the droplets formation. Similar phenomena were also observed for alume powder. Fewer droplets formed by reducing the energy input per unit mass of the powder or by increasing the injected powder per unit length under the same energy input per unit mass of the powder (**Figure 5.1e-h**). By proper controlling both combined parameters, it is beneficial to obtain continuous and smooth tracks.



Figure 5.1 Topography images of tracks prepared with different parameters: (a-d) chromel clads; (e-h) alumel tracks.

Table 5.2 Two combined parameters under different cladding parameters for chromel and alumei.

powder	parameters	morphology	P/ F (J/ g)	F/ V (g/ m)
chromel	22 W 1500 mm/ min 7.3 g/ min	droplets	181	4.9
	15 W 1000 mm/ min 5.7 g/ min	some droplets	158	5.7
	15 W 1500 mm/ min 7.3 g/ min	almost no droplets	123	4.9
	15 W 1000 mm/ min 7.3 g/ min	no droplets	123	7.3
alumei	15 W 2500 mm/ min 8.6 g/ min	droplets	105	3.4
	25 W 2500 mm/ min 8.6 g/ min	some droplets	174	3.4
	15 W 1000 mm/ min 6.3 g/ min	almost no droplets	143	6.3
	15 W 1000 mm/ min 8.6 g/ min	no droplets	105	8.6

The surface temperature profile of one pixel size during deposition was captured by the FLIR IR camera. Due to the limitation of this camera, less than one pixel was involved within one spot size. Therefore, the temperature evolution displayed cannot be compared quantitatively but more qualitatively. **Figure 5.2** shows only the temperature evolution of chromel clads under process parameters of $P=15$ W, $V=1000$ mm/ min, $F=7.3$ g/ min using 0.09 as emissivity. When the laser beam came close to the chosen pixel area, the temperature increased noticeably, and when the laser beam moved further, the temperature decreased. Platforms displayed on the curve during heating and cooling period were the melting and solidification points of melt. The duration of melt were calculated by taking both values at the platforms. **Table 5.3** gives the duration of melt under different cladding parameters for chromel powder. It is obvious that the duration of melt is the shortest than that under the other three parameters. Therefore, no droplets along the track were obtained under the parameters of $P=15$ W, $V=1000$ mm/ min, $F=7.3$ g/ min. It verifies the point that the duration of melt determines whether the droplets would be formed or not after cladding.

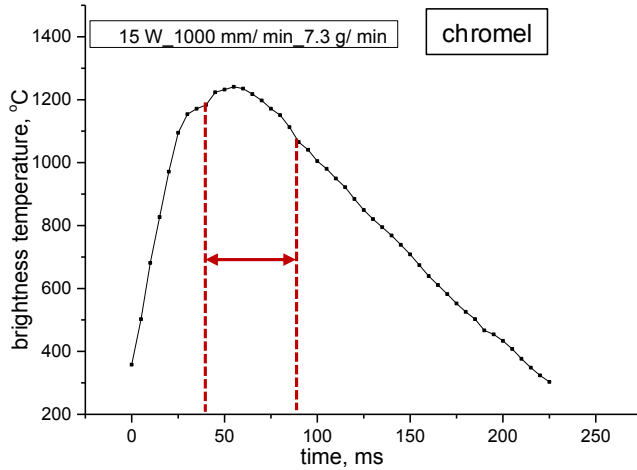


Figure 5.2 Temperature evolution of one pixel for chromel powder under parameters of $P=15$ W, $V=1000$ mm/ min, $F=7.3$ g/ min (emissivity=0.09).

Table 5.3 The duration of melt under different parameters for chromel powder.

parameters	morphology	duration of melt (ms)
22 W 1500 mm/ min 7.3 g/ min	droplets	75
15 W 1000 mm/ min 5.7 g/ min	some droplets	81
15 W 1500 mm/ min 7.3 g/ min	almost no droplets	85
15 W 1000 mm/ min 7.3 g/ min	no droplets	56

With respect to the droplets/ undulation formation mechanism in terms of continuous deposition, limited publications were reported. Tracks with periodic undulation were observed when the process parameters were not properly optimized by laser cladding process [24, 44, 102-103]. It was reported that when the energy per unit length of Inco 904L on stainless steel 304L was insufficient, surface tension would dominant the whole process and broke the molten clads into individual droplets. Melts hydrodynamics (driven by Marangoni effect) became more important when excessive energy per unit length were afforded accompanied by an increase of the melt volume and a decrease of the melt viscosity. The HAZ became larger with the decrease of the scanning speed. More powder from the track boundaries were melted and the molten clads become irregular [103].

In order to obtain continuous clads, Steen et al [104] reported that the average energy per unit area must exceed the threshold value to guarantee good wetting of the Nimonic 75 by the Stellite 12. Mazumder et al [89] reported that minimum average energy per unit area of WC-12 wt.% Co against low carbon steel was required to form a continuous track during the process.

The humping phenomenon was more observed and reported by arc welding process [105-109]. The backward flow of molten weld metal was proved to be responsible for the initial formation and the growth of a hump correlated to the high surface tension confirmed by a LaserStrober video imaging system [109]. The strong momentum of the backward flow of molten metal inside the weld pool prevents backfilling of the front portion of the weld pool. When increasing the power or the welding speed, the velocity and momentum of the flow of molten metal towards the tail of the weld pool must also be higher. Therefore, the droplets on the surface would have higher tendency to be formed. Different models have also been proposed [110-111] and can provide plausible explanations of the periodic behavior of the humping phenomenon. Rayleigh's theory of the instability of a free liquid cylinder due to surface tension to the humping phenomenon was applied during the welding process. This is also reasonable to apply this theory to the laser cladding process because both processes are quite similar.

Consider an infinite cylinder of radius R_c of an ideal fluid which is maintained by surface tension only [112] and is assumed to be freely suspended in space. A small amplitude perturbation analysis shows that all disturbances end up in stable vibrations. If the wavelength of the disturbance exceeds the circumference of the cylinder:

$$\lambda > 2\pi R_c$$

instability starts and the perturbation begins to grow. Eventually the cylinder will break up into droplets. Furthermore, the analysis provides a break up time τ of that disturbance which grows fastest where

$$\tau = 3 \sqrt{\frac{\rho_c}{\sigma} R_c^3}$$

where ρ_c denotes the density, σ the surface tension. So if the solidification time of the droplet exceeds the break up time, the clad may break into droplets.

Table 5.4 gives the radius of the cylinder and break up time under different parameters for chromel powder. The diameters of the cylinder were defined as the widths of cladded tracks. The radiuses for the parameters of $P=15$ W, $V=1000$ mm/ min, $F=7.3$ g/ min and $P=15$ W, $V=1500$ mm/ min, $F=7.3$ g/ min were about 0.103 mm and 0.085 mm, respectively. The break up time was calculated according to the above formula which was below 170 μ s. With higher power or lower powder feeding rate, the radius became larger which were 0.139 mm and 0.114 mm, respectively. The break up time took longer and was about 263 μ s and 192 μ s under higher laser power and lower powder feeding rate. Since the break up time is in the order of μ s rather than ms, this result is not able to interpret the droplets phenomenon quantitatively either.

Table 5.4 The radiuses and break up time of clads under different parameters for chromel powder.

parameters	morphology	R_c (mm)	τ (μ s)
$P=22$ W, $V=1500$ mm/ min, $F=7.3$ g/ min	droplets	0.139	263
$P=15$ W, $V=1000$ mm/ min, $F=5.7$ g/ min	some droplets	0.114	192
$P=15$ W, $V=1500$ mm/ min, $F=7.3$ g/ min	almost no droplets	0.085	127
$P=15$ W, $V=1000$ mm/ min, $F=7.3$ g/ min	no droplets	0.103	167

* $\rho=8.91$ g/ cm^3 , $\sigma=1.76$ N/ m @ 1450 $^{\circ}$ C [113]

In general, the wetting behavior for aludel is more difficult than chromel. It is reported that the addition of Cr (or Cr-O clusters) can significantly improve the wettability of liquid Cu on ZrO_2 substrate [114]. According to this, the presence of Cr element in chromel makes the big difference in the wetting behavior between aludel (Ni-2Al2Mn1Si) and chromel (Ni-10Cr).

6. Summary and Outlook

In this work, a new method for fabricating high temperature type K thermocouple (TC) sensors using laser cladding technology has been developed.

The first experiment showed that the heat affected zone (HAZ) was significantly influenced by the energy per unit area and the powder feeding rate as well as the peak power. Reducing the energy per unit area, the peak power or increasing the powder feeding rate was beneficial to reduce the dimension of the HAZ.

The dimensions of produced type K TC sensors by continuous wave (CW) laser cladding were in the range of two hundred microns in thickness and width. The average roughness was for the cladmed alumel was $10 \pm 2 \mu\text{m}$ and for the chromel was $9 \pm 2 \mu\text{m}$. The resistivity of cladmed alumel ($0.638 \mu\Omega\cdot\text{m}$) is two times larger than its nominal value ($0.29\text{-}0.33 \mu\Omega\cdot\text{m}$) after optimization. This may be due to the easy oxidation of aluminum formed especially at the alumel grain boundaries. The non-conductive alumina can block the electrical current. The resistivity of cladmed chromel ($0.776 \mu\Omega\cdot\text{m}$) is close to its nominal value ($0.706 \mu\Omega\cdot\text{m}$) after optimization. This may be due to the conductive chromium oxide scale formed in the chromel tracks. It is possible to embed sensors manufactured by CW laser cladding and reliable performance was confirmed with the thermosensitivity measurement. The Seebeck coefficients of cladmed thermocouple are estimated as $41.2 \mu\text{V}/\text{K}$ before embedding and $40.9 \mu\text{V}/\text{K}$ after embedding which are close to the reported value $41.1 \mu\text{V}/\text{K}$.

The dimensions of cladmed TC sensors by pulsed laser cladding were less than 100 microns by pulsed laser cladding. It has been not achieved to embed such sensors due to the poor bonding strength between the clads and the substrate up to now.

The shear force measurements were carried out with all the optimized parameters for both kind of alumel and chromel clads to evaluate the adhesion strength. Results show that a big scattering was obtained due to the roughness substrate surface and the tip of the shearing tool was difficult to be placed. The adhesion strength between the cladmed tracks and the substrate plays an important role but not the most significant factor for the subsequent successful embedding.

Reducing the powder feeding rate, increasing the travelling speed or the laser power leads to the formation of periodically droplets along the clads. Regarding to its formation mechanism, the duration of melt which determined by two important combined parameters (P/F and F/V) is critical for the droplets formation. Smooth tracks can be obtained by reducing the duration of melt. Rayleigh's theory could be applied to explain the periodically formed droplets along the clads. If the wavelength of the disturbance exceeds the circumference of the cylinder, instability starts and the cylinder will break up into droplets eventually. The presence of Cr in chromel makes the big difference in the wetting behavior between alumei ($Ni-2Al2Mn1Si$) and chromel ($Ni-10Cr$).

In summary, the manufactured TC sensors by the laser cladding technique provide minimal intrusion to the substrate, small feature sizes (100~200 μm), low roughness (~10 μm) and electrical conductivity. Several advantages are possessed by this technique when fabricating TC sensors, such as neither vacuum processing nor application of masks during cladding as well as less time-consuming.

This technology is still in its infancy, and there are many opportunities and challenges both in terms of the process itself and potential applications. However, the microstructure improvement of laser cladded thermocouple sensors is a topic to be continually focused on. Future work how the embedded sensors affect the lifetime of TBCs in terms of degradation needs to be studied. Application and system level issues associated with sensor placement have to be further addressed. In addition, the different sensors, like strain gauge sensors, flow sensors, piezoelectric sensors, accelerometers et al need be adopted for different purposes.

7. Literature

- [1] S. M. Meier, D. K. Gupta; The evolution of thermal barrier coatings in gas turbine engine applications. *Journal of Engineering for Gas Turbines and Power*, Vol. 116 (1), 1994, p. 250-257.
 - [2] N. P. Padture, M. Gell, E. H. Jordan; Thermal barrier coatings for gas-turbine engine applications. *Science*, Vol. 296 (5566), 2002, p. 280-284.
 - [3] A. Feuerstein, J. Knapp, T. Taylor, A. Ashary, A. Bolcavage, N. Hitchman; Technical and economical aspects of current thermal barrier coating systems for gas turbine engines by thermal spray and EB-PVD: a review. *Journal of Thermal Spray Technology*, Vol. 17 (2), 2008, p. 199-213.
 - [4] D. Stöver, G. Pracht, H. Lehmann, M. Dietrich, J. E. Döring, R. Vaßen; New material concepts for the next generation of plasma-sprayed thermal barrier coatings. *Journal of Thermal Spray Technology*, Vol. 13 (1), 2004, p. 76-83.
 - [5] L. B. Chen; Ytria stabilized zirconia thermal barrier coatings-a review. *Surface Review and Letters*, Vol. 13 (05), 2006, p. 535-544.
 - [6] D. R. Clarke, S. R. Phillpot; Thermal barrier coating materials. *Materials Today*, Vol. 8 (6), 2005, p. 22-29.
 - [7] R. Vaßen, M. O. Jarligo, T. Steinke, D. E. Mack, D. Stöver; Overview on advanced thermal barrier coatings. *Surface & Coatings Technology*, Vol. 205 (4), 2010, p. 938-942.
 - [8] D. Zhu, R. A. Miller; Thermal barrier coatings for advanced gas turbine engines. *MRS Bulletin*, Vol. 25 (07), 2000, p. 43-47.
 - [9] R. Vassen, A. Stuke, D. Stöver; Recent developments in the field of thermal barrier coatings. *Journal of thermal spray technology*, Vol. 18 (2), 2009, p. 181-186.
 - [10] R. A. Miller; Thermal barrier coatings for aircraft engines history and directions. *Journal of thermal spray technology*, Vol. 6 (1), 1997, p. 35-42.
-

-
- [11] V. S. Stubican; Phase equilibria and metastabilities in the systems $\text{ZrO}_2\text{-MgO}$, $\text{ZrO}_2\text{-CaO}$, and $\text{ZrO}_2\text{-Y}_2\text{O}_3$. *Advanced Ceramic Materials*, Vol. 24A, 1984, p. 71-85.
- [12] S. Stecura; Optimization of the Ni-Cr-Al-Y/ $\text{ZrO}_2\text{-Y}_2\text{O}_3$ thermal barrier system. *Advanced Ceramic Materials*, Vol. 1 (1), 1986, p. 68-76.
- [13] R. Darolia; Thermal barrier coatings technology: critical review, progress update, remaining challenges and prospects. *International materials reviews*, Vol. 58 (6), 2013, p. 315-348.
- [14] S. Bose, J. DeMasi-Marcin; Thermal barrier coating experience in gas turbine engines at Pratt & Whitney. *Journal of thermal spray technology*, Vol. 6 (1), 1997, p. 99-104.
- [15] W. A. Nelson, R. M. Orenstein; TBC experience in land-based gas turbines. *Journal of thermal spray technology*, Vol. 6 (2), 1997, p. 176-180.
- [16] C. Mercer, J. R. Williams, D. R. Clarke, and A. G. Evans; On a ferroelastic mechanism governing the toughness of metastable tetragonal-prime (t') yttria-stabilized zirconia. *Proceedings of the royal society A*, Vol. 463 (2081), 2007, p. 1393-1408.
- [17] U. Schulz, M. Schmücker; Microstructure of ZrO_2 thermal barrier coatings applied by EB-PVD. *Materials Science and Engineering: A*, Vol. 276 (1-2), 2000, p. 1-8.
- [18] R. Vaßen; Thermal Barrier Coatings. *Ceramics Science and Technology*, Wiley-VCH Verlag GmbH & Co. KGaA, Vol. 4, 2013, p. 95-115.
- [19] B. Preauchat, S. Drawin; Isothermal and cycling properties of zirconia-based thermal barrier coatings deposited by PECVD. *Surface and Coatings Technology*, Vol. 146-147, 2001, p. 94-101.
- [20] T. E. Strangman; Thermal barrier coatings for turbine airfoils. *Thin Solid Films*, Vol. 127, 1985, p. 93-105.
- [21] M. Peters, K. Fritscher, G. Staniek, W. A. Kaysser, U. Schulz; Design and Properties of Thermal Barrier Coatings for advanced turbine engines. *Materials Science and Engineering Technology*, Vol. 28 (8), 1997, p. 357-362.
-

-
- [22] J. R. Nicholls, K. J. Lawsons, A. Johnstone, D. S. Rickerby; Methods to reduce the thermal conductivity of EB-PVD TBCs. *Surface and Coatings Technology*, Vol. 151-152, 2002, p. 383-391.
- [23] H. Huang, K. Eguchi, T. Yoshida; Novel structured yttria-stabilized zirconia coatings fabricated by hybrid thermal plasma spraying. *Science and Technology of Advanced Materials*, Vol. 4(6), 2003, p. 617-622.
- [24] M. Fasching, F. B. Prinz, L. E. Weiss; ‘Smart’ coatings: a technical note. *Journal of Thermal Spray Technology*, Vol. 4 (2), 1995, p. 133-136.
- [25] A. P. Newbery, P. S. Grant; Oxidation during electric arc spray forming of steel. *Journal of Materials Processing Technology*, Vol. 178 (1-3), 2006, p. 259-269.
- [26] P. J. Kelly, R. D. Arnell; Magnetron sputtering: a review of recent developments and applications. *Vacuum*, Vol. 56 (3), 2000, p. 159-172.
- [27] J. F. Lei, L. C. Martin, H. A. Will; Advances in thin film sensor technologies for engine applications. *ASME 1997 International Gas Turbine and Aeroengine Congress and Exhibition*. American Society of Mechanical Engineers, 1997.
- [28] F. B. Prinz, L. E. Weiss, D. P. Siewiorek; Electronic packages and smart structures formed by thermal spray deposition. *U.S. Patent 5278442*, 1994.
- [29] S. Sampath, A. Patel, A. H. Dent, R. Gambino, H. Herman, R. Greenlaw, E. Tormey; Thermal spray techniques for fabrication of meso-electronics and sensors. *Materials Research Society Proceedings*, Vol. 624, 2000, p. 181-188.
- [30] S. Sampath, J. Longtin, R. Gambino, H. Herman, R. Greenlaw, E. Tormey; Direct-write thermal spraying of multilayer electronics and sensor structures. *Direct-Write Technologies for Rapid Prototyping Applications*, A. C. Pique and D. B. Chrisey, Ed., Academic Press, New York, 2002, p. 261-302.
- [31] S. Sampath, H. Herman, R. J. Greenlaw; Method and apparatus for fine feature spray deposition. *U.S. Patent 6576861*, 2003.
-

-
- [32] J. P. Longtin, S. Sampath, R. Gambino, R. Greenlaw, J. Brogan; Direct-write thermal spray for sensors and electronics: an overview. *NIP & Digital Fabrication Conference, Society for Imaging Science and Technology*, Vol. 2006 (3), 2006, p. 116-119.
- [33] C. Gouldstone, J. Brogan, R. Greenlaw, R.J. Gambino, J. Gutleber, S. Sampath, J. Longtin; Embedded resistive strain sensors for harsh environments. *IEEE Aerospace Conference*, 2006.
- [34] J. Gutleber, J. Brogan, R. Gambino, C. Gouldstone, R. Greenlaw, S. Sampath, J. Longtin; Embedded temperature and heat flux sensors for advanced health monitoring of turbine engine components. *IEEE Aerospace Conference*, 2006.
- [35] T. S. Theophilou, J. P. Longtin, S. Sampath, S. Tankiewicz, R. J. Gambino; Integrated heat-flux sensors for harsh environments using thermal-spray technology. *IEEE Sensors Journal*, Vol. 6 (5), 2006, p. 1126-1133.
- [36] J. Longtin, S. Sampath, S. Tankiewicz, R. J. Gambino, R. J. Greenlaw; Sensors for harsh environments by direct-write thermal spray. *IEEE Sensors Journal*, Vol. 4 (1), 2004, p. 118-121.
- [37] J. P. Longtin, E. Mari, Y. Tan, S. Sampath; Using thermal spray and laser micromachining to fabricate sensors. *Journal of Thermal Spray Technology*, Vol. 20 (4), 2011, p. 958-966.
- [38] O. Svelto; Principles of Lasers. *Plenum Press*, New York, 1998.
- [39] V. S. Aizenshtadt, V. I. Krylov, A. S. Metel'skii; Tables of Laguerre Polynomials and Functions. *Pergamon Press*, Oxford, 1966.
- [40] L. Sexton, S. Lavin, G. Byrne, A. Kennedy; Laser cladding of aerospace materials. *Journal of Materials Processing Technology*, Vol. 122 (1), 2002, p. 63-68.
- [41] R. Vilar; Laser cladding. *Journal of Laser Applications*, Vol. 11 (2), 1999, p. 64-79.
- [42] R. Vilar; Laser alloying and laser cladding. *Materials Science Forum*, Vol. 301, 1999, p. 229-252.
- [43] E. Toyserkani, A. Khajepour, S. F. Corbin; Laser cladding. *CRC press*, 2004.
-

-
- [44] J. Laeng, J. G. Stewart, F. W. Liou; Laser metal forming processes for rapid prototyping-a review. *International Journal of Production Research*, Vol. 38 (16), 2000, p. 3973-3996.
- [45] U. De Oliveira, V. Ocelik, J. T. M. De Hosson; Analysis of coaxial laser cladding processing conditions. *Surface and Coatings Technology*, Vol. 197 (2), 2005, p. 127-136.
- [46] W. M. Steen, V. M. Weerasinghe, P. Monson; Some aspects of the formation of laser clad tracks. *International Symposium/ Innsbruck. International Society for Optics and Photonics*, 1986, p. 226-234.
- [47] J. Powell, P. S. Henry, W. M. Steen; Laser cladding with preplaced powder: analysis of thermal cycling and dilution effects. *Surface engineering*, Vol. 4 (2), 1988, p. 141-149.
- [48] J. D. Kim, Y. Peng; Melt pool shape and dilution of laser cladding with wire feeding. *Journal of Materials Processing Technology*, Vol. 104 (3), 2000, p. 284-293.
- [49] E. Lugscheider, H. Bolender, H. Krappitz; Laser cladding of paste bound hardfacing alloys. *Surface Engineering*, Vol. 7 (4), 1991, p. 341-344.
- [50] J. Y. Jeng, B. Quayle, P. J. Modern, W. M. Steen; Computer control of laser multi-powder feeder cladding system for optimal alloy scan of corrosion and wear resistance. *LAMP*, Vol. 11 (2), 1992, p. 819-824.
- [51] B. Gruenwald, S. Nowotny, W. Henning, F. Dausinger, H. Hugel; New technological developments in laser cladding. *Laser Materials Processing*, Vol. 2306, 1994, p. 934-944.
- [52] W. M. Steen, V. M. Weerasinghe, P. Monson; High power lasers and their industrial applications. *SPIE*, Vol. 650, 1986, p. 226-234.
- [53] Y. P. Hu, C. W. Chen, K. Mukherjee; Development of a new laser cladding process for manufacturing cutting and stamping dies. *Journal of materials science*, Vol. 33 (5), 1998, p. 1287-1292.
- [54] P. A. Vetter, T. Engel, J. Fontaine; Laser cladding: the relevant parameters for process control. *Laser Materials Processing: Industrial and Microelectronics Applications*, Vol. 2207, 1994, p. 452-462.
-

-
- [55] M. Murphy, C. Lee, W. M. Steen; Studies in rapid prototyping by laser surface cladding. *Laser Materials Processing*, Vol. 2306, 1994, p. 882-887.
- [56] J. Lin, W. M. Steen; Design characteristics and development of a nozzle for coaxial laser cladding. *Journal of Laser Applications*, Vol. 10 (2), 1998, p. 55-63.
- [57] X. Wu, B. Zhu, X. Zeng, X. Hu, K. Cui; Critical state of laser cladding with powder auto-feeding. *Surface and Coatings Technology*, Vol. 79, 1996, p. 200-204.
- [58] S. F. Corbin, E. Toyserkani, A. Khajepour; Cladding of an Fe-aluminide coating on mild steel using pulsed laser assisted powder deposition. *Materials Science and Engineering: A*, Vol. 354 (1-2), 2003, p. 48-57.
- [59] E. Toyserkani, S. F. Corbin, A. Khajepour; Iron aluminide coating of mild steel using laser assisted powder deposition. *Proceeding of the 11th International Symposium on Processing and Fabrication of Advanced Materials Processing*, 2002, p. 244-257.
- [60] M. Doubenskaia, P. Bertrand, I. Smurov; Optical monitoring of Nd: YAG laser cladding. *Thin Solid Films*, Vol. 453-454, 2004, p. 477-485.
- [61] M. L. Griffith, M. E. Schlienger, L. D. Harwell, M. S. Oliver; Understanding thermal behavior in the LENS process. *Materials & Design*, Vol. 20 (2-3), 1999, p. 107-113.
- [62] D. P. Hand, M. D. T. Fox, F. M. Haran, C. Peters, S. A. Morgan, M. A. McLean, W. M. Steen, J. D. C. Jones; Optical focus control system for laser welding and direct casting. *Optics and Lasers in Engineering*, Vol. 34 (4-6), 2000, p. 415-427.
- [63] G. Bi, A. Gasser, K. Wissenbach, A. Drenker, R. Poprawe; Identification and qualification of temperature signal for monitoring and control in laser cladding. *Optics and Lasers in Engineering*, Vol. 44 (12), 2006, p. 1348-1359.
- [64] H. Tan, J. Chen, X. Lin, F. Zhang, W. Huang; Research on molten pool temperature in the process of laser rapid forming. *Journal of Materials Processing Technology*, Vol. 198 (1-3), 2008, p. 454-462.
-

-
- [65] W. C. Lin, C. Chen; Characteristics of thin surface layers of cobalt-based alloys deposited by laser cladding. *Surface and Coatings Technology*, Vol. 200 (14-15), 2006, p. 4557-4563.
- [66] M. Doubenskaia, I. Smurov, S. Grigoriev, M. Pavlov; Complex analysis of elaboration of steel-TiC composites by direct metal deposition. *Journal of Laser Applications*, Vol. 25 (4), 2013, p. 1-8.
- [67] W. Gao, S. Zhao, F. Liu, Y. Wang, C. Zhou, X. Lin; Effect of defocus manner on laser cladding of Fe-based alloy powder. *Surface and Coatings Technology*, Vol. 248, 2014, p. 54-62.
- [68] Y. Sun, M. Hao; Statistical analysis and optimization of process parameters in Ti6Al4V laser cladding using Nd: YAG laser. *Optics and Lasers in Engineering*, Vol. 50 (7), 2012, p. 985-995.
- [69] J. Feng, M. G. S. Ferreira, R. Vilar; Laser cladding of Ni-Cr/Al₂O₃ composite coatings on AISI 304 stainless steel. *Surface and Coatings Technology*, Vol. 88 (1), 1997, p. 212-218.
- [70] J. De Damborenea, A. J. Vázquez; Laser cladding of high-temperature coatings. *Journal of materials Science*, Vol. 28 (17), 1993, p. 4775-4780.
- [71] L. C. Lim, Q. Ming, Z. D. Chen; Microstructures of laser-clad nickel-based hardfacing alloys. *Surface and Coatings Technology*, Vol. 106 (2), 1998, p. 183-192.
- [72] Y. Li, W. M. Steen; Laser cladding of stellite and silica on aluminum substrate. *Proc. SPIE 1979, International Conference on Lasers and Optoelectronics*, 602, 1993.
- [73] S. Sircar, C. Ribaudo, J. Mazumder; Laser clad nickel based superalloys: microstructure evolution and high temperature oxidation studies. *Proc. SPIE 0957, Laser Beam Surface Treating and Coating*, 29, 1988.
- [74] A. Hidoucia, J. M. Pelletiera, F. Ducoinb, D. Dezertc, R. E. Guerjouma; Microstructural and mechanical characteristics of laser coatings. *Surface and Coatings Technology*, Vol. 123 (1), 2000, p. 17-23.
- [75] X. Wu; In situ formation by laser cladding of a TiC composite coating with a gradient distribution. *Surface and Coatings Technology*, Vol. 115 (2), 1999, p. 111-115.
-

-
- [76] Y. Sen, W. Liu, M. Zhong; Microstructure characteristics and properties of in-situ formed TiC/Ni based alloy composite coating by laser cladding. *Proc. SPIE 4831, First International Symposium on High-Power Laser Macroprocessing*, 481, 2003.
- [77] L. R. Katipelli, A. Agarwal, N. B. Dahotre; Laser surface engineered TiC coating on 6061 Al alloy: microstructure and wear. *Applied Surface Science*, Vol. 153 (2), 2000, p. 65-78.
- [78] C. Hu, H. Xin, L. M. Watson, T. N. Baker; Analysis of the phases developed by laser nitriding Ti-6Al-4V alloys. *Acta materialia*, Vol. 45 (10), 1997, p. 4311-4322.
- [79] P. Ding, J. Liu, G. Shi, S. Zhou, P. Cao; Laser surface alloying of a low alloy steel with cobalt. *Journal of materials processing technology*, Vol. 58 (1), 1996, p. 131-135.
- [80] A. Frenk, W. Kurz; High speed laser cladding: solidification conditions and microstructure of a cobalt-based alloy. *Materials Science and Engineering: A*, Vol. 173 (1), 1993, p. 339-342.
- [81] J. Przybylowicz, J. Kusinski; Laser cladding and erosive wear of Co-Mo-Cr-Si coatings. *Surface and Coatings Technology*, Vol. 125 (1), 2000, p. 13-18.
- [82] A. Frenk, W. Kurz; Microstructure formation in laser materials processing. *Lasers in Engineering*, Vol. 1, 1992, p. 193-212.
- [83] A. Frenk, M. Vandyoussefi, J. D. Wagnière, W. Kurz, A. Zryd; Analysis of the laser-cladding process for stellite on steel. *Metallurgical and Materials Transactions B*, Vol. 28 (3), 1997, p. 501-508.
- [84] F. Audebert, R. Colaco, R. Vilar, H. Sirkin; Production of glassy metallic layers by laser surface treatment. *Scripta materialia*, Vol. 48 (3), 2003, p. 281-286.
- [85] F. Lusquinos, J. Pou, J. L. Arias, M. Larosi, A. de Carlos, B. Leon, M. P. Amor, S. Best, W. Bonfield, F. C. M. Driessens; Laser surface cladding: a new promising technique to produce calcium phosphate coatings. *Key Engineering Materials*, Vol. 218, 2001.
- [86] S. Nowotny, S. Scharek, E. Beyer, K. H. Richter; Laser beam build-up welding: precision in repair, surface cladding, and direct 3D metal deposition. *Journal of Thermal Spray Technology*, Vol. 16 (3), 2007, p. 344-348.
-

-
- [87] A. Rosochowski, A. Matuszak; Rapid tooling: the state of the art. *Journal of materials processing technology*, Vol. 106 (1), 2000, p. 191-198.
- [88] P. F. Jacobs; Stereolithography and other RP and M technologies: from rapid prototyping to rapid tooling. *SME Press*, New York, 1996.
- [89] J. Mazumder, D. Dutta, N. Kikuchi, A. Ghosh; Closed loop direct metal deposition: art to part. *Optics and Lasers in Engineering*, Vol. 34 (4), 2000, p. 397-414.
- [90] C. P. Paul, H. Alemohammad, E. Toyserkani, A. Khajepour, S. Corbin; Cladding of WC-12 Co on low carbon steel using a pulsed Nd: YAG laser. *Materials Science and Engineering: A*, Vol. 464 (1-2), 2007, p. 170-176.
- [91] H. Choi, A. Datta, X. Cheng, X. Li; Microfabrication and characterization of metal-embedded thin-film thermomechanical microsensors for applications in hostile manufacturing environments. *Journal of Microelectromechanical Systems*, Vol. 15 (2), 2006, p. 322-329.
- [92] M. Riabkina-Fishman, J. Zahavi; Laser alloying and cladding for improving surface properties. *Applied Surface Science*, Vol. 106, 1996, p. 263-267.
- [93] F. Hansen, W. W. Duley; Attenuation of laser radiation by particles during laser materials processing. *Journal of laser applications*, Vol. 6 (3), 1994, p. 137-143.
- [94] M. Gremaud, I. D. Wagnière, A. Zryd, W. Kurz; Laser metal forming: process fundamentals. *Surface Engineering*, Vol. 12 (3), 1996, p. 251-259.
- [95] J. Lin; Temperature analysis of the powder streams in coaxial laser cladding. *Optics & Laser Technology*, Vol. 31 (8), 1999, p. 565-570.
- [96] J. Ch. Liu, L. Li, Y. Zhang, X. Xie; Attenuation of laser power of a focused Gaussian beam during interaction between a laser and powder in coaxial laser cladding. *Journal of Physics D: Applied Physics*, Vol. 38 (10), 2005, p. 1546-1550.
- [97] K. Nakashima, H. Matsumoto, K. Mori; Effect of additional elements Ni and Cr on wetting characteristics of liquid Cu on zirconia ceramics. *Acta materialia*, Vol. 48 (18-19), 2000, p. 4677-4681.
-

-
- [98] R. Marshall, L. Atlas and T. Putner; The preparation and performance of thin film thermocouples. *Journal of Scientific Instruments*, Vol. 43 (3), 1996, p. 145-150.
- [99] S. Sun, Y. Durandet, M. Brandt; Parametric investigation of pulsed Nd: YAG laser cladding of stellite 6 on stainless steel. *Surface and Coatings Technology*, Vol. 194 (2-3), 2005, p. 225-231.
- [100] A. Yakovlev, E. Trunova, D. Grevey, M. Pilloz, I. Smurov; Laser-assisted direct manufacturing of functionally graded 3D objects. *Surface and Coatings Technology*, Vol. 190 (1), 2005, p. 15-24.
- [101] I. S. Grigoriev, E. Z. Meilikhov, A. A. Radzig; Handbook of Physical Quantities. CRC, 1997.
- [102] E. Toyserkani, A. Khajepour, S. Corbin; 3-D finite element modeling of laser cladding by powder injection: effects of laser pulse shaping on the process. *Optics and Lasers in Engineering*, Vol. 41, 2004, p. 849-867.
- [103] I. Yadroitsev, P. Bertrand, I. Smurov; Parametric analysis of the selective laser melting process. *Applied surface science*, Vol. 253(19), 2007, p. 8064-8069.
- [104] W. M. Steen, C. G. H. Courtney; Hardfacing of Nimonic 75 using 2 kW continuous wave CO₂ laser. *Metals technology*, Vol. 7(1), 1980, p. 232-237.
- [105] F. Savage, E. F. Nipples, K. Agusa; Effect of arc force on defect formation in GTA welding. *Welding Journal*, Vol. 58 (7), 1979, p. 212-224.
- [106] C. E. Albright, S. Chiang; High speed laser welding discontinuities. *Journal of Laser Applications*, Vol. 1 (1), 1988, p. 18-24.
- [107] S. Tsukamoto, H. Irie, M. Inagaki, T. Hashimoto; Effect of focal position on humping bead formation in electron beam welding. *Transactions of National Research Institute for Metals*, Vol. 25 (2), 1983, p. 62-67.

- [108] S. Tsukamoto, H. Irie, M. Inagaki, T. Hashimoto; Effect of beam current on humping bead formation in electron beam welding. *Transactions of National Research Institute for Metals*, Vol. 26 (2), 1984, p. 135-140.
- [109] T. C. Nguyen, D. C. Weckman, D. A. Johnson, H. W. Kerr; The humping phenomenon during high speed gas metal arc welding. *Science and Technology of Welding and Joining*, Vol. 10 (4), 2005, p. 447-459.
- [110] B. J. Bradstreet; Effect of surface tension and metal flow on weld bead formation. *Welding Journal*, Vol. 47 (7), 1968, p. 314-322.
- [111] U. Gratzke, P. D. Kapadia, J. Dowden, J. Kross, G. Simon; Theoretical approach to the humping phenomenon in welding processes. *Journal of Physics D: Applied Physics*, Vol. 25 (11), 1992, p. 1640-1647.
- [112] Rayleigh Lord; Theory of sound. *New York*, 1896, p. 351-362.
- [113] J. Brillo, I. Egry; Surface tension of Nickel, copper, iron and their binary alloys. *Journal of Materials Science*, Vol. 40, 2005, p. 2213-2216.
- [114] K. Nakashima, H. Matsumoto, K. Mori; Effect of additional elements Ni and Cr on wetting characteristics of liquid Cu on zirconia ceramics. *Acta materialia*, Vol. 48(18), 2000, p. 4677-4681.

Acknowledgements

I would like to express my deep appreciation to Prof. Dr. Robert Vaßen for giving me this opportunity to come to IEK-1 (Forschungszentrum Jülich) for studying and being my ‘Doktorvater’. I have learned a lot, not only the knowledge but also the dedication to research. Thanks to Prof. Dr. Detlev Stöver for his work in evaluating my dissertation and being my co-referee, as well as to Prof. Dr. Marcus Petermann for the chairmanship during the examination.

I am most grateful to Dr. Daniel Emil Mack for his guidance, expertise with knowledge and interactive discussions in the process for accomplishing of my PhD work. I also appreciate my co-supervisor, Dr. Georg Mauer for his persistent motivation and endless support on me.

I would like to thank my best German friend Dr. Malte Willberg for his lots of support on my work, my daily English practicing and German teaching. Thanks for having lunch as well as spending time with me during my private life. I appreciate it a lot. Best wishes for him and his family!

Many thanks to Dr. Qianli Ma to support me whenever I need help. I appreciate it a lot. Thanks for explaining my endless doubts and spending time together to have lunch as well as play card, mahjong and have parties...I feel very lucky to know him. Best wishes for him and his family as well!

Thanks to my flatmate Mengchu Tao to live with me for over two years. I am not as active as now without you. It is full of fun to stay and spend time together. Hope you can find your truth love soon. All the best to her and her future!

Thanks to Panpan Wang for her support during writing my dissertation. I could work as late as I want because I knew she was there waiting for me to go back home in the darkness no matter how late it was. I could not finish my work on time without her. Best kisses and wishes for her and her PhD work!

Thanks to Wenting He for helping me to prepare the documents for the Chinese embassy after I leave Germany. Thanks for spending time together and we had lots of fun. All the best to her and her PhD as well.

Many thanks to Dr. Manuel Krott for his support on my work and also to Dr. Philipp Terberger. Thanks to Jan Bergholz and Dr. Diana Marciano to visit me from time to time and have fun together (swim, pubs, parties) which makes me much more cosy here. Thank you so much!

Thanks to Dr. Tomas Keuter, Dr. Chih-Long Tsai, Dr. Stefan Rezanka, Markus Mutter, Dr. Emine Bakan, Yang Liu and Dapeng Zhou for being my lovely colleagues. All the best!

I would also like to give my thanks to my sweet colleagues Kai Wilkner, Mark Kappertz, Ralf Laufs, Ralf Steinert, Werner Herzhof, Bader Volker, Rainer Kriescher, Frank Vondahlen especially Karl-Heinz, Rauwald for supporting me on my work in IEK-1. I am not able to finish my work without them. All the best to all of you!

Many thanks to Iris Schönnneis-Vogel, Vicky Rostin, Hiltrud Moitroux, Stefan Weitz, and especially Marianne Meyer to support me on my work. I appreciate it a lot!

I would like to express my deepest love to my eternal mom and wish to be your daughter the next life again!!! My love to my father, my elder brother, my sister-in law and my little nephew, you have no idea how much I love you all!

Many thanks to Dr. Jian He for your tolerance and your love. Best wishes to you and your future!

Thanks to all of you in IEK-1!

Yanli Zhang

● General Information

Gender: Female

Date of Birth: September 9th, 1986

Place of Birth: Shandong Province, China

Tel: 13021168383

Citizenship: People's Republic of China

E-Mail: yanli zhang@aliyun.com

● Education

Oct. 2012-Jan. 2016 **PhD** **Material Engineering** **Forschungszentrum Jülich (FZJ)**

Supervisor: Prof. Dr. Robert Vaßen

✧ Research field: Laser Cladding, 'Smart' Coatings.

Sep. 2009-Feb. 2012 Master Material Science Beihang University

Supervisor: Prof. Hongbo Guo

✧ Research field: Thermal Spray Technique, Thermal Barrier Coatings, Electronic Beam Physical Vapor Deposition.

Sep. 2005-Jun. 2009 **Bachelor** **Chemical Material** **University of Jinan**

- ✧ Majors: Chemical Material, Physical Chemistry, Nanomaterials, Principles of Metals, Advanced Materials Processing Engineering, Material Corrosion and Protection, Mechanical Design...

● Researching Experiences

➤ *Development of In-situ Sensors for High Temperature Coatings*

- ✧ The deposition of in-situ sensors (such as thermocouples, strain gauges) within Thermal Barrier coatings on the gas turbine engines to monitor its operating history, which is very significant to increase the life time of the coatings.

✧ One patent has been applied but still under argument.

➤ *National Natural Science Foundation of China*

- ✧ The deposition of ceramic coatings with certain composition by electron beam physical vapour deposition (EB-PVD) method to test the thermal conductivity coefficient.

➤ *Operation of the High Temperature Performance Laboratory*

- ✧ To operate the instrument, including Differential Scanning Calorimetry (DSC), Thermogravimetry (TG), Static Oxidation Instrument to make sure the smoothly running of the different experiments.

➤ *Influence of the Composition of Bond Coat to the Life Time of the Thermal Barrier Coatings*

✧ The design of the composition, the oxidation and corrosion resistance experiments.

● Publications

1. **Y. Zhang**, R. Vassen, D. Mack, et al., Embedded sensors for high temperature coatings by laser cladding technique, **German Patent**, PT 1.2663 PCT, 2014.
2. **Y. Zhang**, L. Guo, Y. Yang, et al. Influence of Gd₂O₃ and Yb₂O₃ co-doping on the phase stability,

thermo-physical properties and sintering of 8YSZ, Chinese Journal of Aeronautics, 25 (2012) 948-953.

3. J. He, H. Guo, **Y. Zhang**, et al., Improved hot-corrosion resistance of Si/Cr co-doped NiAlDy alloy in simulative sea-based engine environment, Corrosion Science 85 (2014) 232-240.

● Key Skills

- Languages: Chinese, English and German (Elementary)
- Instruments: Laser (Cladding) Facility, Scanning Electron Microscope (SEM), X-ray Diffraction (XRD), Laser Thermal Conductivity Meter, Differential Scanning Calorimeter, Thermogravimetry...

● Hobbies

- Badminton, swimming.

Band / Volume 299

**Optical near-field investigations of photonic structures
for application in silicon-based thin-film solar cells**

A. M. Ermes (2015), vi, 157 pp

ISBN: 978-3-95806-108-8

Band / Volume 300

**Strom- und Gasmärktedesign zur Versorgung
des deutschen Straßenverkehrs mit Wasserstoff**

M. Robinus (2015), VI, 255 pp

ISBN: 978-3-95806-110-1

Band / Volume 301

**Alterung von Vakuum-plasmagespritzten MCrAlY-Schutzschichten
und ihre Wechselwirkung mit Nickel- und Cobalt-basierten
 γ/γ' -Superlegierungen**

P. J. Terberger (2015), IX, 149 pp

ISBN: 978-3-95806-113-2

Band / Volume 302

Verbundvorhaben ELFA Effiziente Luftfahrzeuge

Brennstoffzellensysteme zur Energieerzeugung BREZEN –
Teilprojekt: Kerosinaufbereitung

R. Peters, J. Meißner, J. Pasel, R. C. Samsun, D. Stolten
(2016), viii, 84 pp

ISBN: 978-3-95806-114-9

Band / Volume 303

**Cavity-Ringdown-Spektroskopie zur Untersuchung der Rolle
höherer Stickoxide für den nächtlichen Schadstoffabbau in der
unteren Atmosphäre**

S. Schrade (2016), II, 118 pp

ISBN: 978-3-95806-116-3

Band / Volume 304

**Thermo-mechanical Properties of Mixed Ionic-Electronic
Conducting Membranes for Gas Separation**

V. K. Stournari (2016), 167 pp

ISBN: 978-3-95806-117-0

Band / Volume 305

**Untersuchungen zu suspensionsplasmagespritzten
Wärmedämmschichtsystemen**

N. Schlegel (2016), X, 136 pp

ISBN: 978-3-95806-118-7

Band / Volume 306

**Laser processing for the integrated series connection
of thin-film silicon solar cells**

B. Turan (2016), xii, 188 pp

ISBN: 978-3-95806-119-4

Band / Volume 307

**Development and Application of a Multiscale Model
for the magnetic Fusion Edge Plasma Region**

F. Hasenbeck (2016), 190 pp

ISBN: 978-3-95806-120-0

Band / Volume 308

**Emissions of Biogenic Volatile Organic Compounds and
Ozone Balance under Future Climate Conditions**

C. Wu (2016), VI, 105 pp

ISBN: 978-3-95806-121-7

Band / Volume 309

**Computerunterstützte Auslegung eines Brennstoffzellen-Batterie-
Hybridsystems für die Bordstromversorgung**

C. Krupp (2016), iii, 207 pp

ISBN: 978-3-95806-124-8

Band / Volume 310

**Influence of H₂O, HCl and H₂S on the Release and
Condensation of Trace Metals in Gasification**

M. Benito Abascal (2016), XIX, 172 pp

ISBN: 978-3-95806-125-5

Band / Volume 311

**Mechanical and Thermochemical Properties of Nano-structured
Membranes for Gas Separation in Fossil-fired Power Plants**

J. Zhang (2016), II, 134 pp

ISBN: 978-3-95806-126-2

Band / Volume 312

**Development of Embedded Thermocouple Sensors for Thermal
Barrier Coatings (TBCs) by a Laser Cladding Process**

Y. Zhang (2016), II, 108 pp

ISBN: 978-3-95806-129-3

Weitere **Schriften des Verlags im Forschungszentrum Jülich** unter
<http://wwwzb1.fz-juelich.de/verlagextern1/index.asp>

Energie & Umwelt /
Energy & Environment
Band / Volume 312
ISBN 978-3-95806-129-3

